

# Long-term behaviour of prestressed timber decks in road bridge design

T.G. Exterkate



[1]



Faculty of Civil Engineering and Geosciences  
Delft University of Technology

October 30, 2021

# Long-term behaviour of prestressed timber decks in road bridge design

To obtain the degree of Master of Science  
at the Delft University of Technology.

*Author:*  
Thijs Exterkate

*Thesis Committee:*  
Elgar Slooten (Witteveen+Bos)  
Jan-Willem van de Kuilen (TU Delft)  
Michele Mirra (TU Delft)  
Kees Blom (TU Delft)

## Summary

Conventional building methods are still based on the reinforced concrete industry. In the last decades, timber has become more popular because it could be a more sustainable alternative. However, pure timber is not always an option, especially when slender design is required by the client. Because of its low elastic modulus, deflections often require an increased deck height. Therefore, this research focuses on the strengthening of timber bridge decks with reinforcement and prestress in order to increase their slenderness (= the ratio of the span to the height of the cross-section). This might make timber decks more competitive to reinforced concrete designs regarding slenderness. The problem is that prestressing timber decks will lead to creep deformations that induce losses of prestress force. This research is focused on modelling the creep deformations and the resulting resistance losses of prestressed timber decks.

First, a cross-sectional model is developed to be able to find the initial resistance of a reinforced and prestressed timber deck. This model is based on an incrementally increasing curvature so that the deck behaviour can be quantified from zero load to the failure load. Second, a time dependent model is developed to find the displacements and resistance through time. The timber bridge deck is modelled with ODE systems. The ODE's are used to find the (1) displacements and (2) strains of the deck. To obtain the time dependent behaviour of the deck, a viscoelastic E-modulus is substituted into the displacement- and strain equations. This viscoelastic E-modulus decreases with time, which causes an increase in displacements (= creep displacement). In the same way, the strains are modelled over time. The time dependent creep strains are implemented in the cross-sectional model to find the reduced resistance of the timber deck.

The outcomes of the model suggest that large prestress forces lead to negative creep deflections (= creep in upwards direction). Meaning that for the right value of the prestress force, also zero creep deflections can be obtained. Besides creep, the instantaneous deflections are a large part of the total deflections. According to the results of the model, the instantaneous deflections can be decreased by up to 70%. Regarding the resistance, the final increase of bending moment resistance can reach up to 30% by incorporating prestress (at  $t = 50$  years, including losses due to creep). Due to creep, prestress force is lost over time, resulting in a decreased deck resistance. This research shows that the creep losses result in a bending moment resistance decrease of up to 12%. Taking this into account, a bridge deck with a slenderness of 31 to 33 will be able fulfil its requirements after 50 years of service life. Depending on the client requirements, a slenderness of over 34 can be reached.

Using Eurocode, creep deformations are calculated with a simplistic and conservative method. The model that is built in this research gives a more advanced way of determining the creep deformations of a timber deck. This leads to more realistic quantification of creep behaviour. However, Several factors still cause uncertainty in the model. Therefore, experiments with timber decks should be done to obtain more accurate data for the creep behaviour. The model from this research can be calibrated according to data from experiments, which will increase the reliability of the results.

# Contents

- 1 Introduction** **1**
- 1.1 Problem context . . . . . 1
- 1.2 Problem statement . . . . . 2
- 1.3 Objective . . . . . 3
- 1.4 Scope . . . . . 3
  - 1.4.1 Deck configuration . . . . . 3
  - 1.4.2 Deck height . . . . . 5
  - 1.4.3 Materials . . . . . 5
  - 1.4.4 Durability . . . . . 5
- 1.5 Research questions . . . . . 6
- 1.6 Methodology . . . . . 7
  
- 2 Literature review** **10**
- 2.1 Contemporary timber bridges . . . . . 10
  - 2.1.1 Timber bridge decks . . . . . 11
- 2.2 Structural timber . . . . . 13
  - 2.2.1 Benefits of structural timber . . . . . 13
  - 2.2.2 Wood anatomy . . . . . 13
  - 2.2.3 Glued laminated timber . . . . . 14
  - 2.2.4 Laminated Veneer Lumber . . . . . 15
- 2.3 Failure mechanisms . . . . . 15
  - 2.3.1 Effect of reinforcement . . . . . 16
  - 2.3.2 Effect of prestress . . . . . 16
- 2.4 Reinforced timber . . . . . 17
- 2.5 Prestressed timber . . . . . 20
  - 2.5.1 Main problem with prestressed timber . . . . . 22
- 2.6 Creep and prestress losses . . . . . 22
  
- 3 Material Properties** **26**
- 3.1 Glulam . . . . . 27
- 3.2 Laminated Veneer Lumber . . . . . 28
  
- 4 Loads** **29**
- 4.1 Global loads . . . . . 29
  - 4.1.1 Permanent actions ( $G_k$ ) . . . . . 29
  - 4.1.2 Leading variable actions ( $Q_{k,1}$ ) . . . . . 29

4.2	Ultimate limit state . . . . .	30
4.2.1	ULS load configuration . . . . .	31
4.2.2	ULS bending moments . . . . .	32
4.3	Serviceability limit state . . . . .	34
4.4	Loads for creep . . . . .	35
4.5	Guidelines for deflection . . . . .	36
<b>5</b>	<b>Cross-sectional Model</b>	<b>37</b>
5.1	Model description . . . . .	37
5.2	Model for reinforced cross-section . . . . .	37
5.2.1	Cross-sectional properties . . . . .	38
5.2.2	Elastic equations . . . . .	39
5.2.3	Plastic equations . . . . .	40
5.3	Model for prestressed cross-section . . . . .	42
5.3.1	Zero tension at bottom fibre . . . . .	44
5.3.2	Up to elastic limit . . . . .	45
<b>6</b>	<b>Initial behaviour results</b>	<b>47</b>
6.1	Reinforced cross-section . . . . .	47
6.1.1	Effect of tension reinforcement . . . . .	47
6.1.2	Effect of reinforcement allocation . . . . .	48
6.2	Prestressed cross-section . . . . .	51
<b>7</b>	<b>Long-term behaviour</b>	<b>54</b>
7.1	Governing ODE's . . . . .	54
7.1.1	Axial deformation . . . . .	55
7.1.2	Bending . . . . .	56
7.2	Deformation functions . . . . .	58
7.2.1	Axial shortening . . . . .	58
7.2.2	Bending deflection . . . . .	59
7.2.3	Instantaneous displacements . . . . .	62
7.3	Strains . . . . .	62
7.3.1	Axial strains . . . . .	62
7.3.2	Bending strains . . . . .	62
7.3.3	$z_1$ and $z_2$ for tendon layouts . . . . .	63
7.4	Time-dependent E-modulus . . . . .	65
7.4.1	Findley's power law . . . . .	65
7.4.2	Material parameters $m$ and $n$ . . . . .	65
7.4.3	Equation for $E_v(t)$ . . . . .	69
7.4.4	Viscoelastic stiffnesses $E_v I$ and $E_v A$ . . . . .	71
7.5	time-dependent $P$ . . . . .	72
7.5.1	Starting principle . . . . .	72
7.5.2	First time step . . . . .	72
7.5.3	Convergence criterion . . . . .	73
7.5.4	General principle . . . . .	74

<b>8</b>	<b>Long-term results</b>	<b>76</b>
8.1	Deflection . . . . .	76
8.1.1	SLS deflection . . . . .	76
8.1.2	Creep deflection . . . . .	78
8.1.3	Total deflection . . . . .	83
8.2	Moment decrease . . . . .	83
8.2.1	Creep strains . . . . .	84
8.2.2	Moment decrease . . . . .	85
8.3	Span variation . . . . .	88
8.3.1	L = 25 meters . . . . .	88
8.3.2	L = 35 meters . . . . .	89
<b>9</b>	<b>Discussion</b>	<b>91</b>
<b>10</b>	<b>Conclusion</b>	<b>93</b>
	<b>References</b>	<b>99</b>
<b>Appendix A</b>	<b>Design options</b>	<b>104</b>
A.1	Multi Criteria Analysis . . . . .	104
A.2	Cross-section analysis . . . . .	105
A.2.1	Calculations . . . . .	106
A.3	Design choice . . . . .	107
<b>Appendix B</b>	<b>Governing equations</b>	<b>108</b>
B.1	Timber slab (1) . . . . .	108
B.2	Timber box section (2) . . . . .	109
B.3	Hybrid timber box section (3) . . . . .	109
B.4	Reinforced timber box section (4) . . . . .	110
<b>Appendix C</b>	<b>Standard viaducts</b>	<b>113</b>
<b>Appendix D</b>	<b>Timoshenko ODE system</b>	<b>114</b>
D.1	Timoshenko equations . . . . .	114
D.2	Results . . . . .	115

# 1. Introduction

Before the invention of concrete and iron, bridges have primarily been constructed of wood. The main reason for this is its widespread availability in most areas of the world. Besides, little skill is required for basic woodworking. Also without tools, simple bridges of logs or trunks were built. Since then, timber remained the most important building material until the end of the 18th century, when the first manufacturing of structural iron developed. This led to advances in the metal industry. Together with concrete, the first reinforced concrete bridges were designed around the beginning of the 20th century. As a consequence of the development of concrete and steel, timber had lost its presence in bridge design. As a result, the current construction sector is dominated by concrete and steel.

## 1.1 Problem context

The construction sector is a large consumer of energy and natural resources and therefore accounts for significant emissions of greenhouse gases [2], [3]. The main materials causing this are concrete and steel, being the greatest producers of the total greenhouse gas emissions in the building sector [4]. Now that the effects of climate change have made sustainability a necessity, there exists a great challenge towards a more sustainable construction sector. This is why timber is increasingly becoming more popular. In contradiction to concrete and steel, timber is a sustainable alternative that could help mitigating climate change [5]. Also, wood is a renewable material. Sustainable forestry can provide an unlimited amount of structural timber while concrete and steel are prone to depletion of resources [6].

However, the total market share of structural timber is still small in comparison to that of steel and concrete [7]. Mechanical properties, durability and costs are often important reasons to prefer traditional materials over timber. When the spans of traffic bridges become larger, the confidence of building with timber decreases. It is easier to choose alternatives of reinforced concrete because knowledge on these materials is much more comprehensive than on timber. Lots of experience with concrete makes it a reliable option. Generally, use of timber is limited to pedestrian- and bicycle bridges. Many contractors in the Netherlands are not familiar with designing timber structures yet. Therefore, project costs of timber alternatives are often estimated higher than necessary. Also Eurocode provides more in depth information about reinforced concrete constructions than on timber constructions. For these reasons, companies' tendency to use timber in traffic bridges is still small.

In traffic bridge design, client requirements impose strict limitations on construction height. Meaning that there is no space for arches and trusses in these cases. Consequently, these bridges are composed with slender girder like deck types. Most of them are made with reinforced concrete because of its relatively high strength that comes with inexpensiveness of these designs.

Over the past decades, several studies suggest that timber is a more sustainable building material. It would be an alternative to build these bridges with timber. The basic concept of designing with timber is creating high beam systems. This structural height is inherently connected to timber because normalized beam systems have a limited lamellae width. This requires an increased thickness of the cross-section, making it difficult to compete to the slender reinforced concrete variants. Secondly, timber has low stiffness and strength properties compared to reinforced concrete. This results in large deformations, especially for horizontal members. Last, there is a lack of knowledge on the long-term behaviour of timber. Eurocode 5 offers a creep factor approach to incorporate the long-term deformations. In many cases, these creep factors are conservative. Resulting in increased cross-section dimensions. Which is a problem in highway bridge projects, where slender design is an important requirement. Not only because of aesthetic considerations, but a thicker deck will also induce extra project costs because the on-ramps require more groundwork and space, see Figure 1.1. A reinforced concrete alternative is often preferred over a timber alternative.

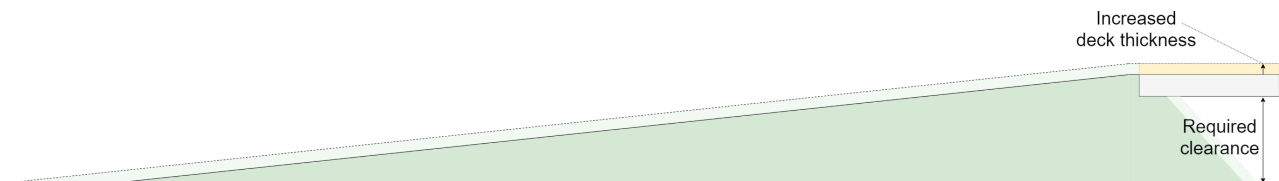


Figure 1.1: More ground work for increased deck thickness

Previous discussed problems ask for new solutions in order to make timber a suitable material for highway bridges. An analysis of different solutions is done in Appendix A, from which is concluded that longitudinally prestressed timber bridge decks are the most promising option. FRP is used as tendon material. Calculations for a prestressed timber deck can be found in Appendix B. Prestressing timber will again introduce its own problems. The instantaneous deflection and initial resistance of a prestressed timber beam can be calculated accurately. However, as mentioned before, uncertainty exists regarding the long-term behaviour of a prestressed system, particularly concerning the losses of prestress due to creep. The problem context is also summarized in a flow chart in Figure 1.2

## 1.2 Problem statement

Timber as a structural material could help in decreasing environmental impacts. Bridge design with timber results in decks with increased cross-sectional height. This makes it difficult to comply with client requirements regarding slenderness. Timber induces additional project costs, making it even more difficult to compete with traditional alternatives. Inno-



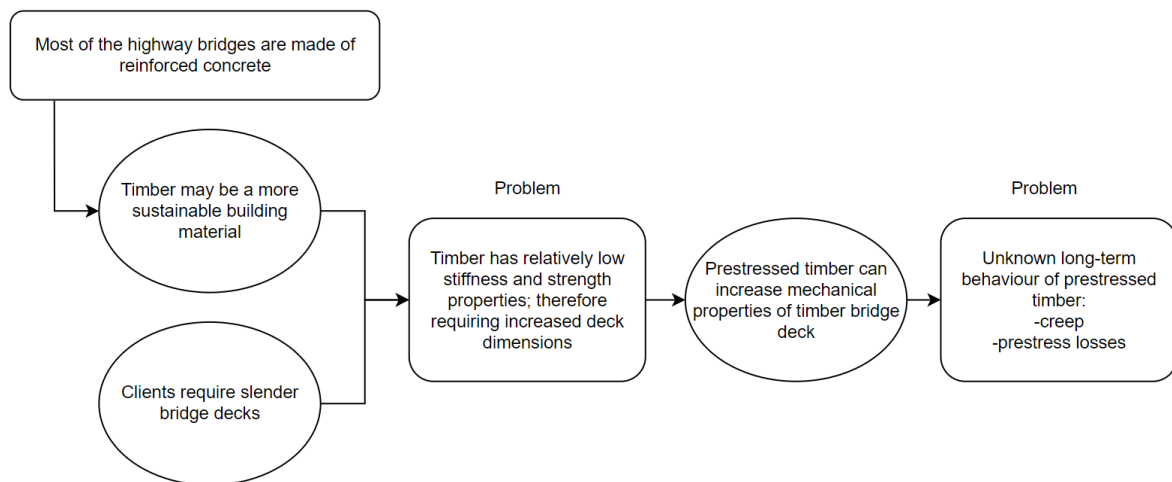


Figure 1.2: Flow chart of problem context

vative solutions like prestressed timber systems sound promising, but will also introduce problems, especially due to its unknown behaviour in the long-term. Problem statement:

**Timber bridge decks require an increased cross-section height and therefore they are not able to compete to standard deck solutions. Prestressed timber decks are subject to long-term processes like creep that increase deformations over time and induce prestress losses.**

### 1.3 Objective

Timber bridge decks require cross-sections with increased height, which lead to costly projects. Prestressing these decks introduces other problems regarding the long-term behaviour. The goal of this research is **to find the maximum slenderness for a prestressed timber bridge deck by quantifying the initial behaviour<sup>[1]</sup> and secondly, modelling the influence of creep on the deflection and prestress losses.** This will result in a conclusion and a set of recommendations about whether prestressed timber bridge decks may be an alternative for reinforced concrete.

<sup>[1]</sup>Initial behaviour is defined as the behaviour of the deck without taking into account the time-dependent behaviour of timber. It includes the instantaneous deflection and the initial bending moment resistance (both based on the material parameters at  $t = 0$ ).

### 1.4 Scope

#### 1.4.1 Deck configuration

Many standard viaducts are made of reinforced concrete having a continuous deck on multiple supports. Some examples representative for the Netherlands can be found in Appendix

C. In this research, a continuous deck over one mid-support with two spans of length  $L$  is considered, see Figure 1.3. In this research, the span  $L$  is varied within a range of 25 to 35 meters. Using this layout, the end result will be applicable to most of the current viaduct cases.

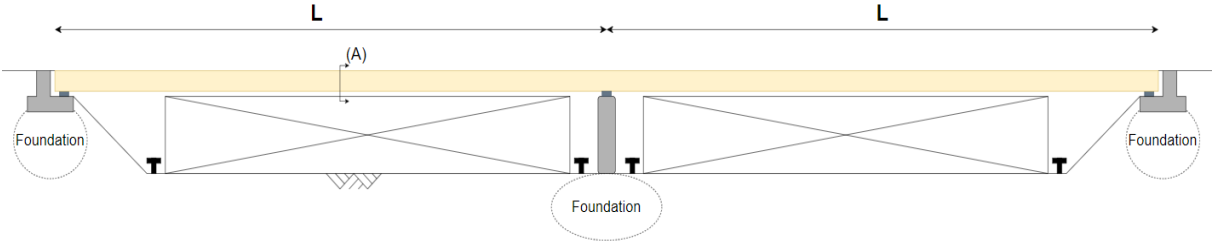


Figure 1.3: Longitudinal view of the bridge deck

The cross-section of the deck is presented in Figure 1.4. It exists of a timber slab. The structural height is  $h_{timber}$ , which also includes the reinforcement. The total deck height is  $h_{timber} + h_{asphalt}$ . If there is spoken of the deck height in this research, the structural deck height is meant (unless stated differently). The total slab is composed of smaller parts, indicated with the vertical dotted lines. The ducts for the prestress cables are milled from the parts. Then the parts are glued together and the prestress ducts are injected with glue. At  $x = 0$  and  $x = 2L$  (see Figures 1.5 and 1.6) the prestress tendons are also attached to the deck ends by plates. It is assumed that the strain of the prestress tendons is the same as the strain of the timber at that location, so strain compatibility is assumed in this research. The reinforcement layers, if present, are glued to the top- and bottom surfaces and anchored at the beam ends. It is important to note that in this research, prestress and reinforcement are different:

- With prestress is meant: the FRP prestress tendons that have a straight- or parabolic profile (so the cross-sectional location can be variable over the longitudinal direction)
- With reinforcement is meant: FRP reinforcement layers that are non-prestressed. Constant cross-sectional location over the longitudinal direction

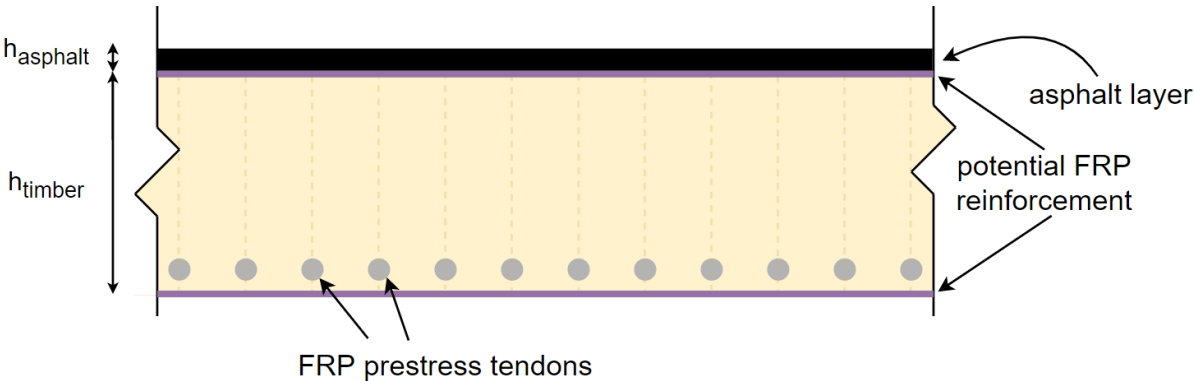


Figure 1.4: Cross-section A (see Figure 1.3) of the timber deck

The model is based on variable tendon layouts. In case of straight tendons, the vertical location  $z$  of the tendons has a constant value, see Figure 1.5. For parabolic tendons, the vertical location  $z$  of the tendons depends on the longitudinal coordinate  $x$ , see Figure 1.6

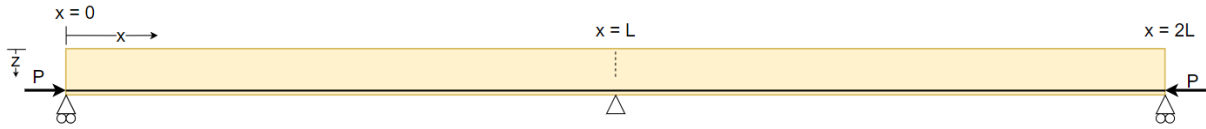


Figure 1.5: Deck with straight tendons

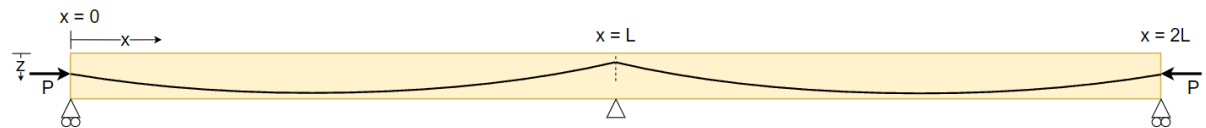


Figure 1.6: Deck with parabolic tendons

### 1.4.2 Deck height

For concrete bridges, spans of around 30 meters give a beam cross-section height of around 1000-1200 mm according to suppliers Haitsma [8] and Romein [9]. This corresponds to a slenderness of up to 30.0, the slenderness is defined as the span over the deck height. The continuous bridge project of the A4 Delft-Schiedam with two spans of 24 and 25.5 meter has a total deck height of 900 mm [10], which corresponds to a slenderness of 28. It should be noted that this design exists of a massive concrete slab. As described in the problem statement, the timber bridge deck should be able to compete with these concrete variants. Therefore, it should have the same total deck height of around 1000 mm and a slenderness of around 30.0.

### 1.4.3 Materials

Timber has a very low embodied energy content when local certified wood is used [11]. Meaning that it is best to use abundantly available woods in Europe. Using solid timber is not an option for spans with an order of magnitude of 20-30 meters. Solid timber is directly cut from a tree stem. Glued Laminated Timber (glulam) or Laminated Veneer Lumber (LVL) offer much more possibilities regarding span length (explained in Sections 2.2.3 and 2.2.4). Glulam and LVL are both products that are fabricated from tree species available in Europe, also making them good options in terms of sustainability. Therefore, this thesis is limited to bridge design using glulam and LVL.

### 1.4.4 Durability

According to Table 1.1, a bridge is designed for up to 100 years. This corresponds to category 4 or 5.

Design working life category	Indicative design working life (years)	Examples
1	10	Temporary structures <sup>(1)</sup>
2	10 to 25	Replaceable structural parts, e.g. gantry girders, bearings
3	15 to 30	Agricultural and similar structures
4	50	Building structures and other common structures
5	100	Monumental building structures, bridges, and other civil engineering structures
(1) Structures or parts of structures that can be dismantled with a view to being re-used should not be considered as temporary.		

Table 1.1: Design working life category according to EN 1990 clause 2.3

According to EN 1995-2 section 4, design measures should be taken to guarantee durability. In the design of this bridge, the timber is protected against weathering by constructional preservation measures:

- Protection of the timber deck by the watertight seal layer.
- No precipitation or solar radiation can reach the timber deck.
- The load bearing components are sufficiently ventilated since they are in direct contact with fresh air.
- No risk of increased moisture contents near the ground since the bridge deck is at elevated height.

Taking into account these measures, the timber is sufficiently protected and falls within Eurocode Service Class 2.

## 1.5 Research questions

Traffic bridges made out of timber may be more sustainable than reinforced concrete bridges. Following from the problem context however, timber requires too thick bridge decks that are not able to compete with the slenderness of reinforced concrete decks. A Prestressed timber deck is mentioned as the most promising solution for increasing the slenderness. To investigate these subjects, following research questions are composed.

### Main research question:

***What is the maximum slenderness that can be obtained by prestressing a timber bridge deck?***

The objective (Section 1.3) will be reached by answering the main research question. Following sub-questions are composed to work towards an answer to the main research question:

### Sub-questions:

1. What are the loads and resulting forces on a timber traffic bridge?

2. What reinforcing/prestressing layouts are most efficient for the initial resistance<sup>[1]</sup>?
3. What are the time-dependent deformations?
4. What are the long-term prestress losses and how do they influence the deck resistance?
5. What slenderness can be reached with prestressed timber bridge decks?

<sup>[1]</sup> *The initial resistance is defined as the resistance at the moment where creep has not yet occurred (at time instant  $t = 0$ )*

## 1.6 Methodology

This section gives a stepwise overview of the tasks that are to be done to answer the main research question. A flowchart of all successive tasks is presented in Figure 1.7

The first task is determining the initial resistance of the deck cross-section. This will be done using a cross-sectional model of the timber deck. Python is used for this task. The cross-sectional model will be based on an incremental increase of curvature. The curvature is increased up to failure of the cross-section. Using this approach, the strains and stresses are quantified at every loading instant of the cross-section. This will give insights about the initial behaviour of the cross-section.

After this, the time-dependent behaviour of the timber will be modelled. This will be done using Maple since this is the most powerful software to work with Ordinary Differential Equations (ODE's). ODE's will be used to quantify the displacements of the timber bridge deck. The bridge deck will be modelled with ODE's for two cases:

- **Bending** - The external loads (like traffic and selfweight) will cause the slender bridge deck to be loaded in bending. Also the forces from prestressing the deck will result in bending deformations.
- **Axial deformation** - The prestress cables are attached to both ends of the timber deck. Therefore, the deck will also be loaded in axial compression.

The ODE's for bending and axial deformation will be used to obtain the deformation functions of the bridge deck. These deformation functions depend on the longitudinal coordinate  $x$  along the deck and the vertical coordinate  $z$  over the height of the deck cross-section. Furthermore, the system parameters will govern the behaviour of the deformation of the timber deck. The system parameters are the span  $L$ , the loads  $q_i$  (due to external forces and prestress), the prestress force  $P$ , the eccentricities of the prestress force  $e_i$ , the bending stiffness  $EI$  and the axial stiffness  $EA$ . When these ODE's are solved for the boundary conditions corresponding to the bridge scope, the initial deformation functions are obtained.

The next step is finding an approach to model the time-dependent behaviour of the bridge deck. This will be done using the initial deformation functions, which are dependent on the stiffnesses  $EI$  and  $EA$ . In order to include time in the deformation functions, the initial E-modulus will be replaced by a viscoelastic E-modulus that is dependent on time:  $E_v(t)$ , this approach is based on Findley's power law for creep behaviour of viscoelastic materials

[12]. The actual formula for  $E_\nu(t)$  depends on parameters regarding the creep behaviour of the material. These parameters will be determined based on creep curves obtained from experiments in literature. By substituting  $E_\nu(t)$  in the deformation functions, the deformation functions become time-dependent. This means that the creep behaviour of the timber can be modelled. By assuming a constant prestress force  $P$ , the time-dependent deformations can be formulated in analytical expressions. However, the prestress material will deform due to the creep of timber, meaning that the prestress force will change within every time step. Therefore, a numerical approach will be used to model the time-dependent deformations. Using the ODE relations, the strains in the timber deck can be modelled for every  $x$  and  $z$  location, at every time instant  $t$ . The prestress tendons are assumed to be glued within the timber cross-section. It is assumed that at the location of the tendon, the strains of the tendon and the timber are compatible. By filling in the tendon profile for  $z$ , the creep strains are found within the prestress tendons.

These creep strains will lead to a change in strain in the prestress material, meaning that the stresses will change, resulting in a change in prestress force and ultimately a change in deck resistance. At the governing locations, the prestress force will decrease. This results in prestress losses and a decrease in resistance. The creep strains from the Maple model will be implemented in the Python model to be able to quantify the decrease in deck resistance. These final resistances can be compared to the actions on the timber deck. By iterating through the flow chart in Figure 1.7, the optimal bridge deck slenderness can be found.

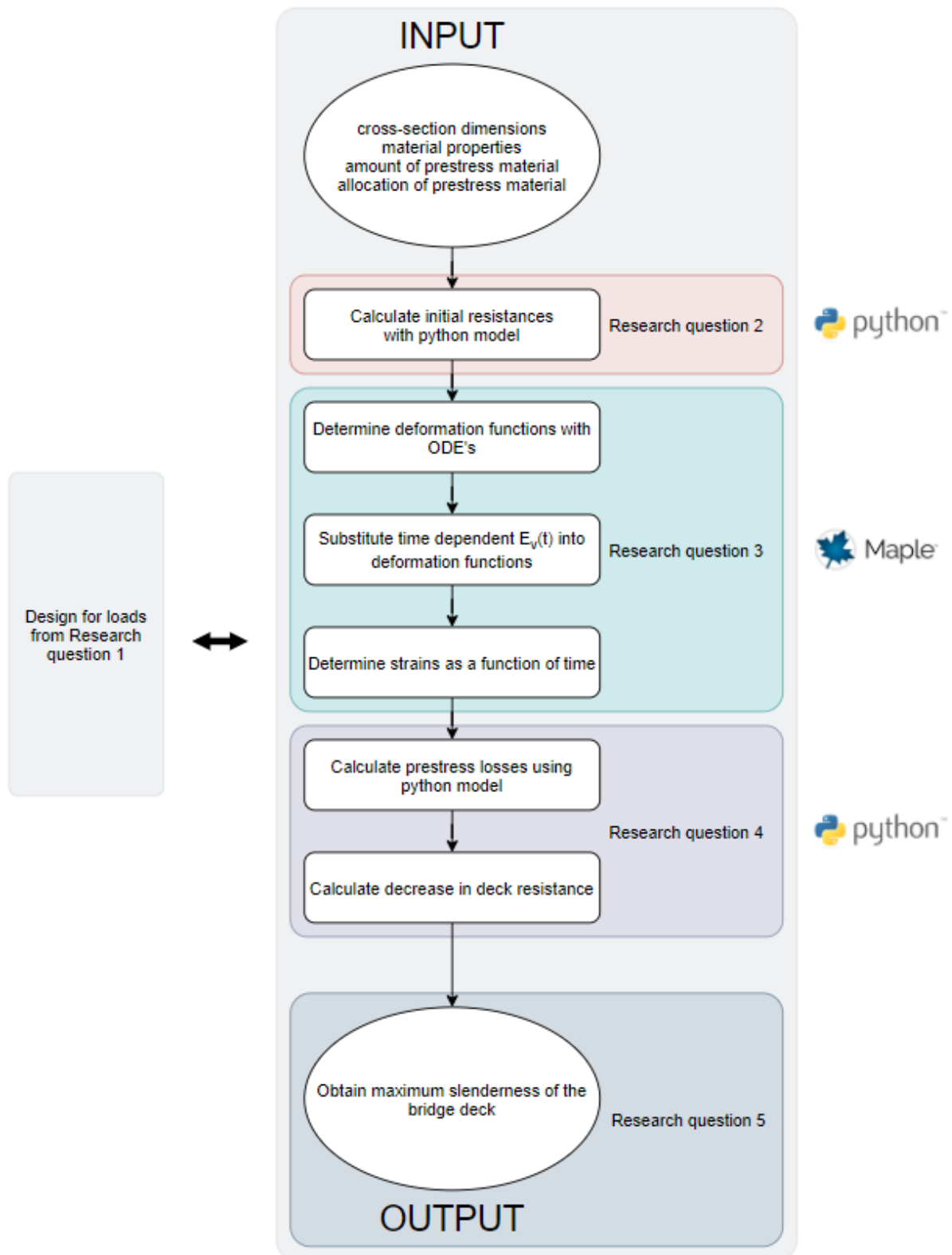


Figure 1.7: Flow chart thesis

## 2. Literature review

### 2.1 Contemporary timber bridges

Several examples of timber bridges for heavy traffic exist, showing that it is possible to reach considerable spans with structural timber. These examples do not have the slenderness that should be reached for this research (see the objective in section 1.3), however they serve as an example of the durability and economic benefit that can be reached with timber as a structural material. These timber bridges are characterized by high aesthetic value and low environmental impact.

#### **Mistissini Bridge**

This bridge in Québec, Canada opened in 2014. It is 160 metres long and consists of four spans of 37, 43, 43 and 37 meters (Figure 2.1a). Glulam is used for the main beams and arches. The total equivalent manufacturing emissions of this bridge are negative, meaning that the bridge consumes CO<sub>2</sub>, rather than releasing it. The bridge costs less than an equivalent steel-concrete bridge and has an expected lifespan of at least 100 years [1].

#### **Mjøsa Bridge**

Two bridge designs over lake Mjøsa in Norway are proposed, a timber and a concrete alternative (Figure 2.1b). If the timber alternative is chosen, it will be the longest timber bridge in the world (1650 metres). Maximum spans are up to 69 metres. These big spans are possible because of the huge two timber trusses that are stabilized using timber diagonals. Results of sustainability studies show that the timber alternative has lower emissions across all environmental impact categories. It only has a slightly higher estimated price than the concrete design [13].

#### **Kjøllsæter Bridge**

The bridge opened in 2005 and is designed for heavy military vehicles, therefore the bridge is considered to be the strongest timber bridge in the world. Glulam GL36c is used for the trusses. The length is 158 meters with a largest span of 45 metres (Figure 2.1c). The bridge is designed for a service life of 100 years. It should be noted that this service life is achieved by





(a) Mistissini Bridge



(b) Mjøsa Bridge



(c) Kjøllsæter Bridge



(d) Sneek Bridge

Figure 2.1: Contemporary timber bridges

treating the wood with creosote, which can be harmful if it leaks into the environment. The price of the timber bridge is slightly higher than the costs of an equivalent steel bridge [14].

## Sneek Bridge

The first timber traffic bridge of Accoya has been built in Sneek in 2009, it spans 32 metres (Figure 2.1d). The life span of the bridge was required to be 80 years. In bridge design, this is often achieved by a toxic chemical preservation. However, this was not considered an acceptable option in the Sneek project. Instead, a new alternative of acetylated radiata pine was launched, also called Accoya [15]. Accoya is shown to have lower environmental impact than other sustainably processed woods [16].

### 2.1.1 Timber bridge decks

#### Stress-Laminated Timber bridge decks

This particular deck type has become popular over the past several years, especially in Scandinavian countries. The concept of a Stress-Laminated Timber (SLT) deck is shown in Figure 2.2. An SLT deck is composed of timber laminations which are stressed together by pre-

stressing rods. The ends of the laminations are simple butt joints which are longitudinally displaced from each other. This allows for a deck plate with a length according to every design requirement. Friction between the laminations will result in redistribution of forces over the total width of the beam. This results in a deck that behaves like an orthotropic plate, see Figure 2.3. An example of a complete SLT deck is shown in Figure 2.4. It can be seen that this design also incorporates a water-tight layer that protects the timber deck. A protective layer like this is used together with an asphalt pavement.

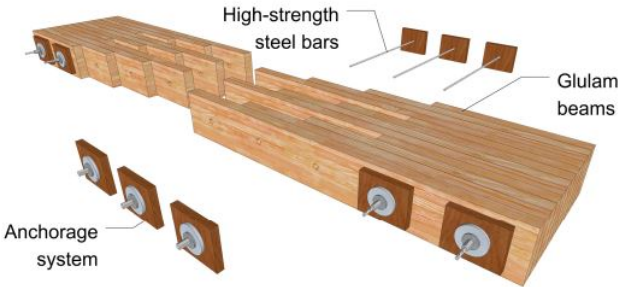


Figure 2.2: Concept of an SLT deck [17] composed of several laminations

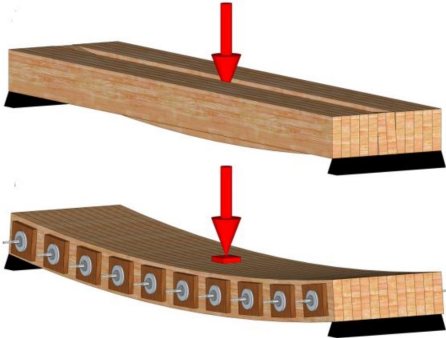


Figure 2.3: Redistribution of forces in an SLT deck [17]

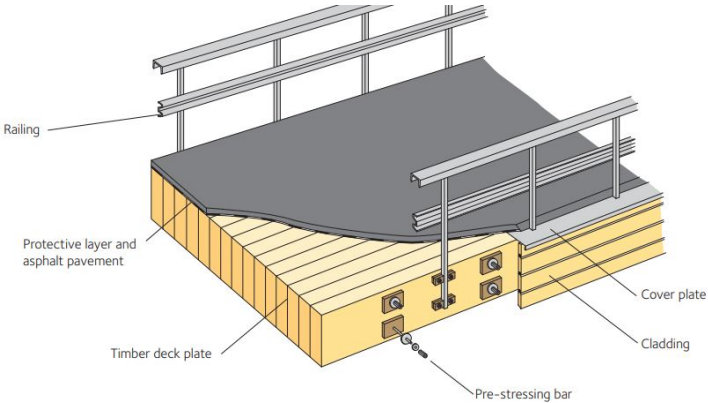


Figure 2.4: Example of an SLT deck with finishing [18]

Dahl et al [19] did research on a 222 mm-thick SLT deck. They did experiments with the same SLT deck as used in the Tynset Bridge. This is a bridge in Norway built for highway traffic loads. Also research is done to bigger thicknesses. Ekholm et al [20] did experiments to full scale SLT decks with a thickness of 270 mm. They found a maximum failure load of 900 kN. Which is much larger than the local wheel loads of 200 kN that should be taken into account according to Eurocode.

## **2.2 Structural timber**

### **2.2.1 Benefits of structural timber**

The main advantage of timber is that it results in less emission of greenhouse gases. It should be noted that this is not something that can be taken for granted when designing with timber. Sustainable timber construction comprises all processes of the manufacturing chain. This means that growing, harvesting, processing and building should all be done eco-friendly. Secondly, timber is a renewable resource, well-managed forestry can provide an unlimited amount of structural timber without depletion of forests. These forests are carbon sinks, which means that they absorb carbon dioxide. Consequently, carbon dioxide from the air is converted into the wood that we use to build, resulting in a negative carbon dioxide footprint [11]. By assessing the sustainability of a timber structure, it is important that also the end of life is taken into account. Because sometimes the timber is burned, resulting in emissions that still end up in the air.

Timber has an excellent strength-over-weight ratio. This results in lightweight timber structures, which is beneficial for the foundations and the construction speed. It also enables prefabrication of large elements, these can be transported to the building site relatively easy. The downside of lightweight structures is that vibration issues may occur as a result of alternating wind or traffic loads. However, these issues are not part of the scope of this research.

Timber components can be prefabricated and transported to the building site. Glulam or LVL are important materials for prefabrication. These materials enable prefabrication of large and slender spans. These bridge components are relatively easy to handle and can be assembled on site in short time spans. Reducing the hinderance on the surrounding of the timber bridge projects.

Wood is a biodegradable material, which mainly means that it is of good use in indoor climates. However, technological knowledge is increasing, making timber a more and more weather resistant material. In general, bridges with Consequences Class 3 should be designed for a lifespan of 100 years. Accoya wood already has a guaranteed service life of 80 years in outdoor climates, making it a good alternative [15]. This is made possible by acetylating wood, which is a sustainable way of modifying the wood structure. However, currently this is only done for the wood species pinus radiata from New Zealand. A good and more sustainable alternative would be to modify local woods. Important to note is that, in some countries, structural timber sometimes is conserved with creosote. This is a chemical that is harmful when it leaches into the environment [21].

### **2.2.2 Wood anatomy**

Wood is an organic material made of cells. It grows naturally and therefore it tends to be an anisotropic material. This means that it has different properties when stress is applied in different directions. Properties also depend on location since a stem cross-section comprises different wood types, see Figure 2.5. Therefore, natural wood is a highly variable and unpredictable material. In Engineered Wood Products (EWP), predictability of behaviour is

increased by disassembling and reassembling parts of wood.

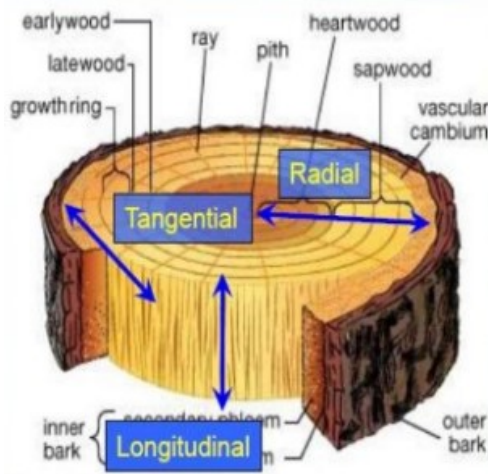


Figure 2.5: Principal directions and different types of wood in cross-section of a stem



Figure 2.6: Sawn timber beam with pith, knots and drying cracks

Solid or sawn timber is produced from logs in sawmills. Solid timber beams still contain knots, fibre direction variation and other natural defects like in Figure 2.6. This causes very scattered mechanical properties of beams with identical dimensions, which makes it impossible to exploit the high strength of the majority of the wood. Therefore, these solid timber beams are graded and assigned to a strength class. This enables more efficient and economical use of timber. Dimensions of solid timber beams are limited by the size of the logs. Heights of these beams go up to around 300 mm. This limits the maximum spans to approximately five to seven meters.

### 2.2.3 Glued laminated timber

Glued laminated timber (glulam) is composed of stacked timber 'lamellae' bonded together by adhesives. The lamellae in glulam are arranged parallel to the grain as can be seen in Figure 2.7. In contradiction, lamellae of cross laminated timber are arranged orthogonally. The idea behind glulam is reducing the variance in mechanical properties and a more homogeneous material. By smart placement of the lamellae, knots and other weak links are less significant. In addition, large knots and defects are removed and the laminate is finger jointed together, Figure 2.8

The great advantage of glulam over solid timber is that its maximum span is not limited by the dimensions of the tree stem. The lamellae can be finger jointed together to form the desired length. These laminated timbers can be manufactured in almost any straight or curved configuration. This makes glulam very suitable for long span components required for bridge design.

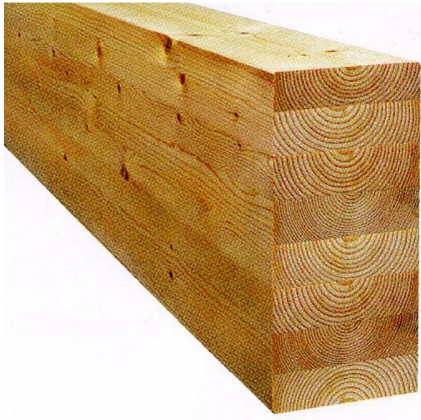


Figure 2.7: Glued laminated timber beam

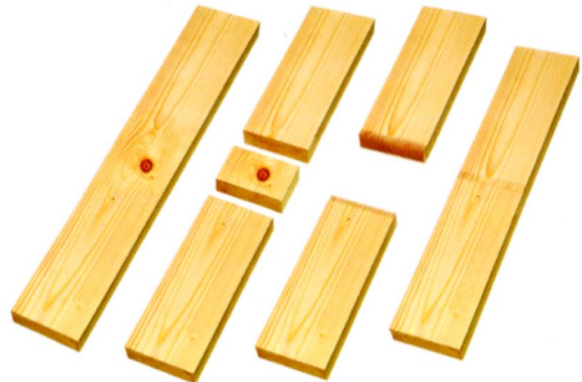


Figure 2.8: Removal of defects within an individual lamellae

### 2.2.4 Laminated Veneer Lumber

The production process of Laminated Veneer Lumber (LVL) is comparable to that of glulam. Instead of sawn wood lamellas (glulam), LVL is produced from wooden veneer sheets that are peeled of a log, see Figure 2.9 and 2.10. The LVL planks can be fabricated with all its sheets in the same grain direction or a cross layered set-up. Same grain direction gives a high axial strength. This can be suitable for beams or columns. The cross-wise lay-up gives a high in plane strength and stiffness, which is suitable for shear walls of floors.

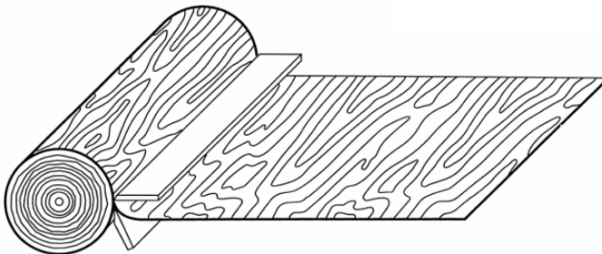


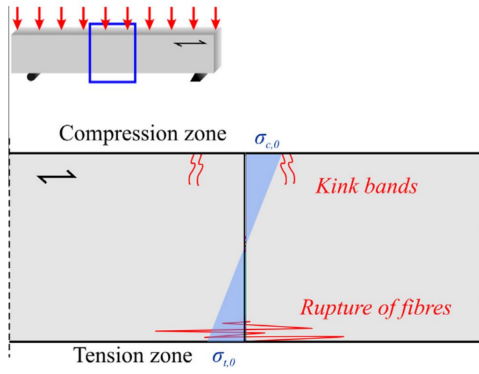
Figure 2.9: Veneer sheet peeling



Figure 2.10: LVL plank

## 2.3 Failure mechanisms

Timber beams (unreinforced and non-prestressed) tend to have a brittle failure in bending. Displacements are proportional until tensile failure on the lower side of the beam, see Figure 2.11. Usually this failure is initiated by the presence of a knot. Compression failure is less susceptible to natural defects and is mostly not governing. Failure under compression can be characterized as a ductile failure [22]. In general, a ductile failure is more desirable than the typical brittle failure of a pure timber beam.



(a) Sketch of typical bending failure of timber



(b) Tension failure for beam in bending

Figure 2.11: Bending failure of timber

### 2.3.1 Effect of reinforcement

Reinforcement enhances the mechanical properties of glulam beams. Increased strength and stiffness properties are obtained by incorporating reinforcement. Also the ductility of a beam in bending can be increased due to the shift of tension failure to compression failure at the upper side of a beam in bending. Tensile reinforcement causes the neutral axis to move towards the bottom of the beam. As a result the compressive strain in the timber increases relative to the tensile strain. Then compressive yielding may occur before the timber fails in tension [22].

### 2.3.2 Effect of prestress

Prestress may increase the strength and stiffness of a timber beam even further. SLS is often governing for high span timber beams. Prestress may lead to an SLS assessment that is less restrictive than the ULS. This is due to the negative bending moment that is exerted on the beam, resulting in negative deflections due to prestressing [23]. Besides, prestressing introduces stresses in the beam that are opposite to the stresses due to actions. This means that prestress results in a negative bending moment that compensates the positive bending moment from the action on the beam. For elastic calculations, following equations can be used to calculate stresses in top and bottom of the beam [24]:

$$\sigma_{top} = \frac{P}{A_t} - \frac{P \cdot e}{w} + \frac{M \cdot y}{I} \quad (2.1a)$$

$$\sigma_{bottom} = \frac{P}{A_t} + \frac{P \cdot e}{w} - \frac{M \cdot y}{I} \quad (2.1b)$$

where  $P$  [kN]: prestress force;  $A_t$  [mm<sup>2</sup>]: area of timber;  $e$  [mm]: eccentricity of tendon placement;  $w$  [mm<sup>3</sup>]: section modulus;  $M$  [kNm]: applied moment;  $y$  [mm]: distance to neutral axis;  $I$  [mm<sup>4</sup>]: second moment of area.

## 2.4 Reinforced timber

**Kliger, Johansson and Crocetti** [25] studied the behaviour of glulam beams reinforced with steel plates and carbon fibre (CFRP) laminates. Modern technologies minimize the problem of delamination of the adhesives. This report does not state that the experiments show adhesive failure. Which means that strains of the glulam and reinforcement are compatible.

Glulam beams without reinforcement were tested to find a reference value of strength and stiffness. Also different configurations of glulam reinforced sections were tested, see Figure 2.12. With respect to the non-reinforced beam, results show that for 5% reinforcement the stiffness increases up to 100% and the ultimate moment capacity increases up to 90%. Another advantage of reinforcement is that the variability of the stiffness is much smaller than the non-reinforced beams, which means more predictable beams.

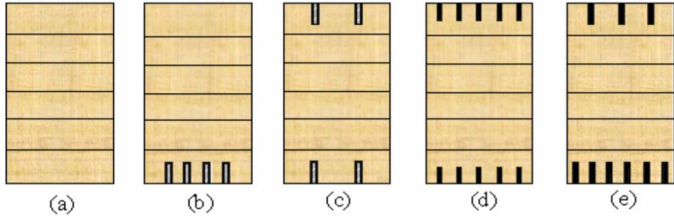


Figure 2.12: Experimental beam configurations from Kliger et al [25]

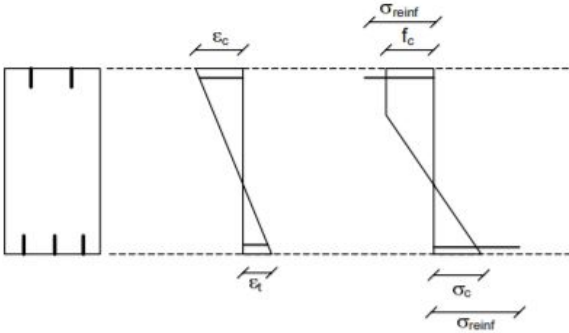


Figure 2.13: Stress distribution adopted by Kliger et al [25]

The cross-sectional model used by this research comprises a linear strain distribution (assumed that planar cross-section remain planar according to Bernoulli), see Figure 2.13. The stress-strain diagram is linear up to compressive failure, then the yield stress remains constant up to strain failure. Therefore, the cross-sectional stress distribution is linear in elastic phase and perfectly plastic when the glulam fails in compression, see Figure 2.13. The model uses five failure modes. First and second are tension failure in elastic phase or elastic-plastic phase in compression. Third mode is compression failure due to too large compression strains. Fourth when the reinforcement starts to yield. Fifth mode is rupture of the reinforcement. They found that the experimental results agreed well with the ultimate moment and deflection results of the calculation model.

**Gentile, Svecova and Rizkalla** [26] carried out a study to sawn timber beams strengthened with glass fibre reinforced polymers (GFRP). No glulam was used in the experiments. 22 half-scale (Figure 2.14a) and 4 full-scale (Figure 2.14b) beams were tested to failure.

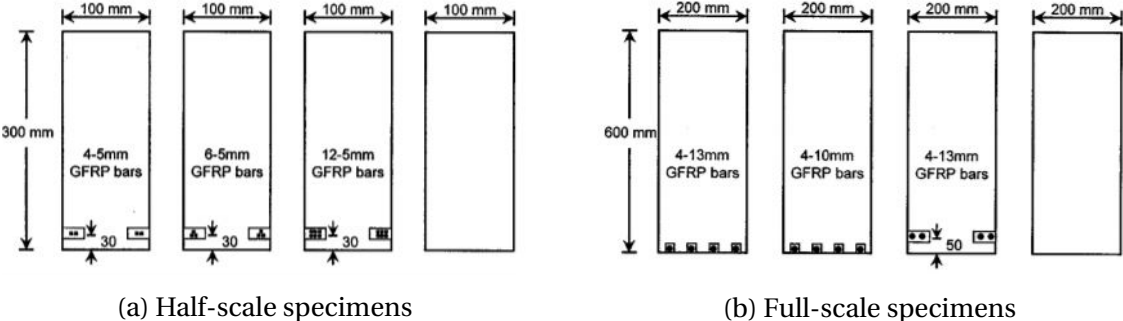


Figure 2.14: Experimental beam configurations from Gentile et al [26]

In contradiction to the reinforced glulam beams from [25] and [27], the results of the half-scale and full-scale beams all show very scattered results. A result of the fact that wood is a highly variable material. The E-modulus and ultimate loads of the reinforced beams are all higher than the unreinforced beams. However, some of the beams with smaller reinforcement ratios show higher E-modulus and ultimate load. This implies that no predictable correlation exists for sawn timber.

Also an analytical model was proposed. The stress distribution was based on a slightly different stress-strain relation than presented by Kliger et al [25] (see Figure 2.15a). When the timber starts to yield, the stresses are not constant. A factor  $m$  is used to decrease the stresses after the yielding point (see Figure 2.15b).

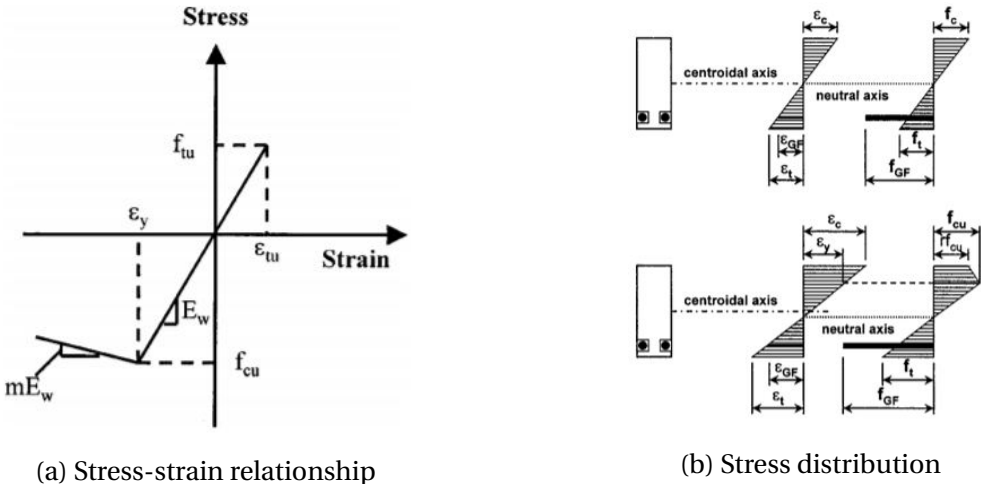


Figure 2.15: Analytical model of Gentile et al

**Blaß and Romani** [27] carried out a research project to glulam reinforced with glass fibres, aramid fibres and carbon fibres. They state that the disadvantage of steel is its lower yield strength. This may lead to plastic deformation of the steel before the timber fails.



The model uses six possible failure modes, see Figure 2.16. Assumed is a constant MOE, constant tensile and compression strength and a linear-elastic-ideal-plastic stress strain relationship. The corresponding failure modes can occur at different locations of the cross-section, as explained in the figure.

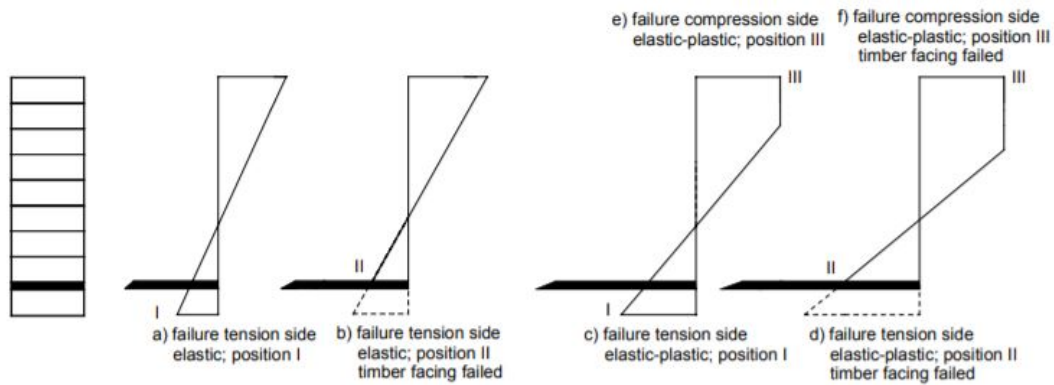


Figure 2.16: Failure modes of a reinforced glulam beam by Blaß and Romani

30 beams with tensile reinforcement were tested. A reinforcing plate was applied between the two bottom timber laminations. Using only tensile reinforcement, the neutral axis shifts downwards and therefore a plastic compression deformation is more likely to occur. The test results were compared to simulations of unreinforced beams. In all cases, the reinforced beams had a significantly higher failure load (reaching from 30% to 100%).

**Hoseinpour, Valluzzi, Garbin and Panizza** [28] tested glulam beams with a height and width of 135 mm and 115 mm respectively. Various configurations and materials were used in the experiments. Flax (a natural product) and carbon fibers were used as reinforcement materials.

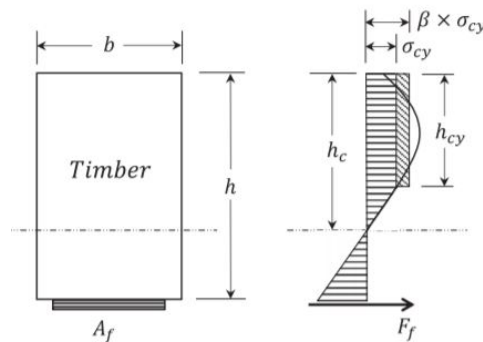


Figure 2.17: Stress distribution adopted by Hoseinpour et al

They analysed several models similar to the ones presented before. Their final model has an elastic behaviour in tension and elastic-perfectly-plastic in compression. In addition, an extra  $\beta$  factor is used for the perfectly plastic stress distribution to calibrate the model, see Figure 2.17. The value for  $\beta$  depends linearly on the height of the plastic zone  $h_{cy}$ .

The desirable compressive failure of timber was only reached with carbon fibers as reinforcement materials. The flax fiber reinforced beams failed in tension. This implies that only relatively strong reinforcements enable the shift from a brittle to a ductile failure.

## 2.5 Prestressed timber

In contradiction to reinforced glulam, prestressed glulam is a rather new concept. Not much research is yet done to prestressed timber. An overview is given by **Kliger, Haghani, Brunner, Harte and Schober** [29]. They state that the best way to improve behaviour of reinforced beams in SLS is by prestressing. Eccentric prestress cables on the tension side induces a negative bending moment, which counteract the bending moment from external loads. The negative bending moment causes a deflection in the upward direction. This counteracts the deflection from external loads. Besides, more efficient use of the material is realized. In passively reinforced timber, the full strength of the reinforcement is often not used because the timber generally fails first. Main advantages of prestressing timber with FRP over passively reinforced systems:

- Less strengthening material is required
- Load bearing capacity increases
- Improvements of design in SLS

In research done before, prestress laminations were often glued to the timber beams. The problem is that delamination of the prestressing material might occur. In case of gluing an FRP laminate to the bottom of a timber beam, high shear stresses occur at the ends of the FRP laminate. However, modern technologies on adhesives make them increasingly stronger. Examples exist on beam experiments where debonding of the prestress materials did not occur [30]. Research has also been done to gradiented anchoring techniques [31]. This technique causes a more evenly distributed shear stress between the timber and the prestress material, resulting in a smaller delamination risk.

Another main challenge is the long-term behaviour of prestressed timber beams. Timber is a material where relatively large creep deflections may occur. Therefore, prestress force is lost over time due to axial shortening of the beam [32], [33]. This is described in Section 2.6

**De Luca and Marano** [34] carried out a research to glulam beams prestressed with steel bars. Their model can be used to calculate the internal forces and the resulting resisting moment, see Figure 2.18. This model is comparable to the previous stated models used for reinforced timber. Only the forces that are imposed by the prestress tendons are now also incorporated. In this case, the model is subjected to a glulam beam with two steel tendons in longitudinal slots at the top and bottom faces, where the bottom tendon is prestressed by a force  $N_p$ . Internal forces ( $R_i$ ) and lever arms ( $d_i$ ) are defined as in Equations 2.2a - 2.2e. These equations are only applicable for ULS, since plastic strains occur at the compression side of the beam.

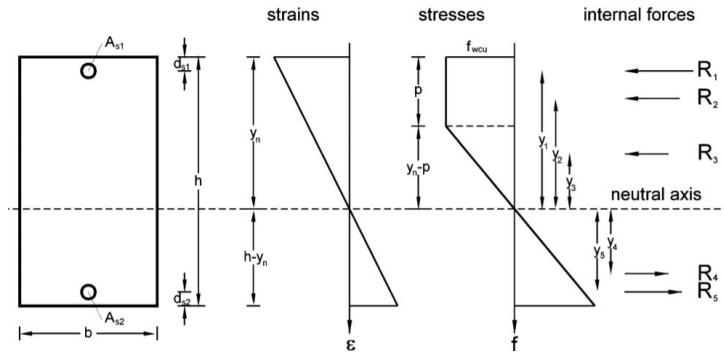


Figure 2.18: Internal forces of a timber beam with steel bars within the top and bottom

$$R_1 = A_{s1} \cdot f_{rein}; \quad d_1 = d_{s1} \quad (2.2a)$$

$$R_2 = p \cdot b \cdot f_{timber}; \quad d_2 = 1/2 \cdot p \quad (2.2b)$$

$$R_3 = ((y_n - p) \cdot b \cdot 1/2) \cdot f_{timber}; \quad d_3 = (y_n - p) \cdot 2/3 \quad (2.2c)$$

$$R_4 = ((h - y_n) \cdot b \cdot 1/2) \cdot f_{timber}; \quad d_4 = y_n + (h - y_n) \cdot 2/3 \quad (2.2d)$$

$$R_5 = A_{s2} \cdot f_{prestess}; \quad d_5 = h - d_{s2} \quad (2.2e)$$

The curvature ( $\chi$ ) is defined as:

$$\chi = \frac{|\epsilon|}{y} \quad (2.3)$$

As can be seen in Figure 2.18, assumption is made that sections remain planar. The strains ( $\epsilon_i$ ) can be calculated as:

$$\epsilon_i = \chi \cdot y_i \quad (2.4)$$

Where  $y_i$  is the distance of the centroid of the areas away from the neutral axis:

$$y_1 = -(y_n - d_{s1}) \quad (2.5a)$$

$$y_2 = -y_n \quad (2.5b)$$

$$y_3 = -(y_n - p) \quad (2.5c)$$

$$y_4 = (h - y_n) \quad (2.5d)$$

$$y_5 = d_{s2} - y_n \quad (2.5e)$$

Equilibrium of internal forces:

$$\sum_i^5 R_i + N_p = 0 \quad (2.6)$$

Where  $N_p$  is the prestressing force acting on the steel bar on the bottom of the beam. The resulting bending moment resistance can be computed as:

$$\sum_i^5 R_i \cdot d_i + N_p \cdot d_5 = 0 \quad (2.7)$$

**Brady and Harte** [33] did research to glulam beams prestressed with FRP laminates bonded to the lower side of the beam. By applying a prestress force, the FRP material may be used more efficiently because a bigger part of its tensile strength is engaged. The material model in this research is based on a bi-linear stress-strain relationship (like presented before in Figure 2.15a).

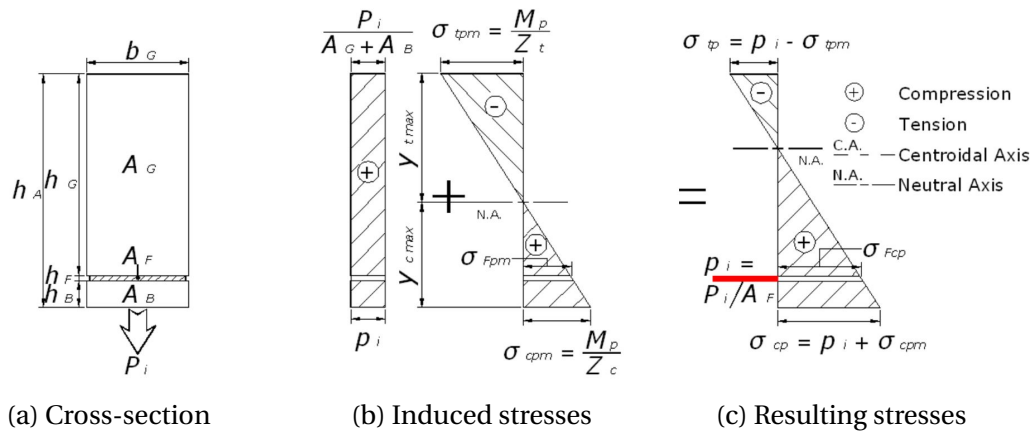


Figure 2.19: Stress distribution resulting from prestressed FRP

By prestressing the FRP laminate, the stress distribution as in Figure 2.19 is created. The eccentric force in the FRP is equivalent to applying an axial compressive force and a negative moment, see Figure 2.19b. The sum of these forces is presented in Figure 2.19c. The experimental prestressed beams gave 98% and 143% higher moment capacities with respect to the unreinforced beam.

### 2.5.1 Main problem with prestressed timber

All articles about prestressed timber describe the short-term behaviour of prestressed systems. Generally this gives good results of increased capacities and stiffnesses. However, in a large part of the articles, it is mentioned that creep might cause prestress losses, decreasing the bending moment resistance over time.

## 2.6 Creep and prestress losses

The forces exerted by prestress cause an axial shortening of a timber member. Because of creep, the shortening becomes bigger over time. This decreases the strains and stresses in the prestress tendons, causes a loss of prestress force over time.

**Palermo et al** did a study to the potential of longitudinal post-tensioning for timber bridges [35]. They conclude that the application of post-tensioning and engineered timber like LVL and glulam increases the competitiveness of timber for bridges. The long-term behaviour is quantified with proposed analytical expressions: They are expressed using geometrical and mechanical features of the section in one parameter named  $\Theta_p$ . Using  $\Theta_p$ , the elastic losses in a simply supported beam with one tensioning tendon can be calculated as follows:

$$\Delta P_{p0} = P_{p0}(1 - \Theta_p)$$

The next equation shows the time-dependent formula approximated using an age-adjusted effective modulus method, where  $\phi(t, t_0)$  is the creep coefficient and  $\chi(t, t_0)$  is the ageing coefficient:

$$\Delta P(t) = P_{p0} \left( 1 - \frac{\Theta_p [1 - (1 - \Theta_p) \cdot \phi(t, t_0) (1 - \chi(t, t_0))]}{1 + \chi(t, t_0) \cdot \phi(t, t_0) \cdot (1 - \Theta_p)} \right)$$

Using these equations, they present two graphs for the prestress losses dependent on the parameter  $\Theta_p$ , see Figure 2.20. The instantaneous losses due to elastic shortening of the timber deck can reach up to 20% of the total prestress force. Depending on the service class, the time-dependent losses can also be calculated. In this research, service class 2 can be used and this will lead to a maximum time-dependent prestress loss of 11%. Which is not a huge decrease of prestress due to the long-term losses.

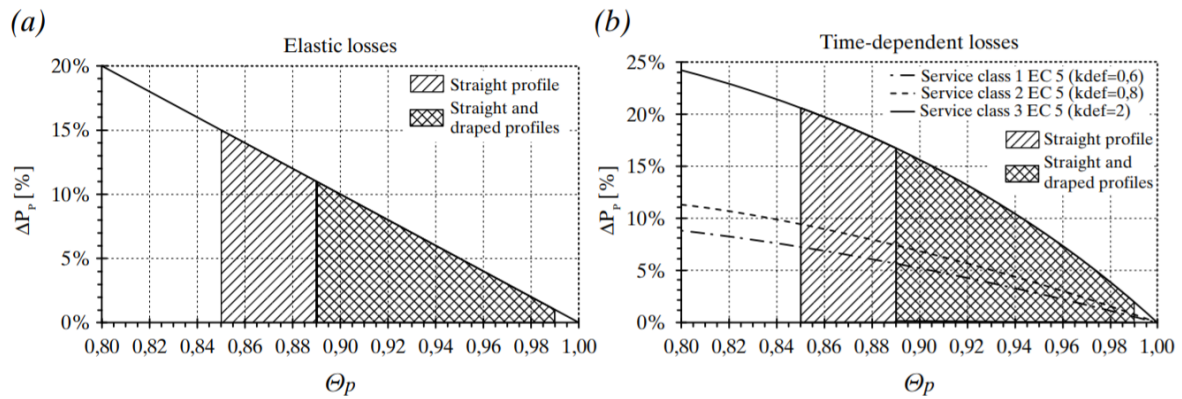


Figure 2.20: Prestress losses in a simply supported beam: (a) elastic losses, (b) time-dependent losses at infinite time [35]

**Willebrands** [36] proposed a creep curve based on experiments from Gowda [37]. Gowda experimented with beams of sawn timber and glulam subject to four point bending tests. Willebrands fitted its own creep curve to the results of the experiment of Gowda:

$$\phi(t) = 0.125 \cdot \ln(0.2t + 1) \quad (2.8)$$

**O’Ceallaigh et al** [38] [39] studied the effect of flexural reinforcement on the long-term behaviour of glulam beams. Creep tests were performed under variable Relative Humidity between 60% and 90%, which corresponds to Service Class 3 conditions. It is concluded that

the reinforced beams had a lower average deflection after 75 weeks than the non-reinforced beams. The tests confirmed that reinforcing timber with FRP material have a beneficial effect on the creep behaviour of timber.

**Fragiacomo and Davies** did research to prestressed radiata pine LVL members [40], [41]. The main issue of a prestressed timber system is its behaviour in the long-term. The beam specimens were tested in bending with straight prestressing tendons through the centroid of the beams, which means that no prestressing moment is applied to the beam cross-section. In their experiments they determined a creep curve for the bending beams with and without prestressing tendons, see Figure 2.21. For the prestressed beams they fitted the following power equation to the experimental results:

$$\phi(t) = 0.033 \cdot t^{0.305} \quad (2.9)$$

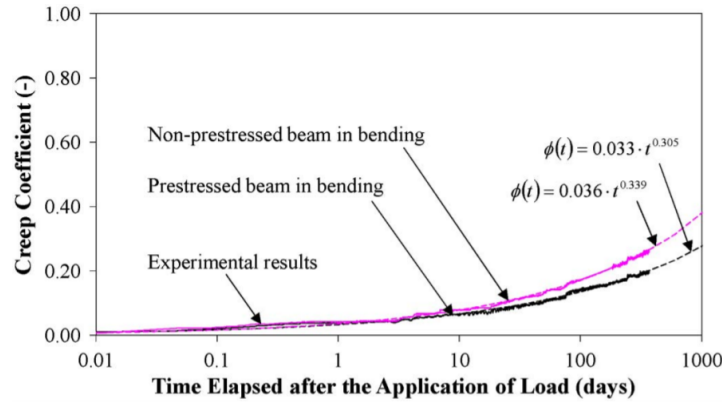


Figure 2.21: Experimental creep curves [40]

They used the model in Figure 2.22 for the time-dependent stress-strain relation of timber. Where the quantities  $\epsilon$  and  $\sigma$  = total strain and stress at the instant  $t$ ;  $\alpha_u$ ,  $\alpha_T$ , and  $T(\tau)$  = moisture expansion coefficient, thermal expansion coefficient, and temperature of timber at the instant  $\tau$ , respectively; and  $J(t, \tau, u)$  = “pure” creep function of timber, given by the function in Figure 2.23. With some manipulations, these complex formulas are rewritten and simplified to the time-dependent equation in Equation 2.10.

$$\begin{aligned} \epsilon(t) = & \int_{t_0}^t J_0(u(\tau)) d\sigma(\tau) + \int_{t_0}^t J_c(t - \tau) d\sigma(\tau) \\ & + \int_{t_0}^t \sigma(\tau) dJ_0(u(\tau)) + J^\infty \int_{t_0}^t \left\{ 1 - e^{-c \int_{\tau}^t |du(\tau_1)|} \right\} d\sigma(\tau) \\ & - \int_{t_0}^t b\epsilon(\tau) du(\tau) + \int_{t_0}^t \alpha_u du(\tau) + \int_{t_0}^t \alpha_T dT(\tau) \end{aligned}$$

Figure 2.22: Model from Toratti [42] used by Fragiaco [41]

$$\begin{aligned}
J(t, \tau, u) &= J_0(u) + J_0(u_{\text{ref}})\phi(t - \tau) \\
&= \frac{1}{E_0(1 - ku)} + \frac{1}{E_0(1 - ku_{\text{ref}})} \cdot a(t - \tau)^d
\end{aligned}$$

Figure 2.23: Pure creep function as used by Toratti [42]

$$\epsilon(t) - \epsilon_{in}(t) = \frac{\sigma_0}{E} [1 + \phi_c(t) + \phi_{ms}(t, U)] \quad (2.10)$$

In Equation 2.10,  $\phi_c(t)$  is the pure creep coefficient. The pure creep coefficient can be given by Equation 2.11

$$\phi_c(t) = a \cdot t^d \quad (2.11)$$

**Bank and Mosallam** did a study to the creep behaviour of a Fibre Reinforced Polymer (FRP) frame. They used Findley's power law to model the creep behaviour. The creep expressions in this model have the same form as the expressions for modelling the creep of timber. The general form of Findley's creep expression is given as:

$$\epsilon(t) = \epsilon_0 + m(t/t_0)^n \quad (2.12)$$

This equation has the same form as the pure creep function as in Equation 2.11, which is used for creep of timber. According to Findley's model, Equation 2.12 can be rewritten to determine a viscoelastic modulus which is dependent on time. So instead of an increasing creep factor (as in Equation 2.11), following E-modulus depending on time is used to determine the creep behaviour:

$$E_v = \frac{E_0 E_t}{E_t + E_0 \cdot t^n} \quad (2.13)$$

In this research, Findley's viscoelastic modulus will be used for the creep behaviour of a timber bridge deck.

### 3. Material Properties

Material properties are calculated from Eurocode. Timber sorts considered are glulam and Laminated Veneer Lumber (LVL). The design value  $X_d$  of a strength property should be calculated according to (EN 1995-1-1):

$$X_d = k_{mod} \frac{X_k}{\gamma_m} \tag{3.1}$$

The design member stiffness property  $E_d$  should be calculated according to (EN 1995-1-1):

$$E_d = \frac{E_{mean}}{\gamma_m} \tag{3.2}$$

Values for  $\gamma_M$  are given in Table 3.1. It can be seen that the  $\gamma_M$  value for LVL is slightly more beneficial.

Glued laminated timber	1,25
LVL, plywood, OSB,	1,2

Table 3.1:  $\gamma_M$  values (EN 1995-1-1)

In the bridge design, the timber parts are protected against direct influences from precipitation (also see section 1.4.4). Therefore, service class 2 is assigned. This gives values for  $k_{mod}$  and  $k_{def}$  as in Table 3.2 and 3.3. Both the values are the same for glulam and LVL.

Material	Standard	Service class	Load-duration class				
			Permanent action	Long term action	Medium term action	Short term action	Instantaneous action
Glued laminated timber	EN 14080	1	0,60	0,70	0,80	0,90	1,10
		2	0,60	0,70	0,80	0,90	1,10
		3	0,50	0,55	0,65	0,70	0,90
LVL	EN 14374, EN 14279	1	0,60	0,70	0,80	0,90	1,10
		2	0,60	0,70	0,80	0,90	1,10
		3	0,50	0,55	0,65	0,70	0,90

Table 3.2:  $k_{mod}$  values (EN 1995-1-1)



Material	Standard	Service class		
		1	2	3
Glued Laminated timber	EN 14080	0,60	0,80	2,00
LVL	EN 14374, EN 14279	0,60	0,80	2,00

Table 3.3:  $k_{def}$  values (EN 1995-1-1)

### 3.1 Glulam

Properties of glulam are given in Table 3.4. For glulam depths in bending up to 600 mm the characteristic value for  $f_{m,k}$  may be increased with the factor  $k_h$  (EN 1995-1-1 clause 3.3). However, depths of the beams for this project will be around 1000 mm, so  $k_h$  is not applicable.

For lamination thickness of less than 40 mm, the bending strength may be multiplied by a factor  $k$  (EN 14080 clause 5.1.3):

$$k = \min\left(\left(\frac{40}{t}\right)^{0.1}; 1.05\right) \quad (3.3)$$

For glulam members made of at least ten laminations the product ( $E_{0,g,k}G_{g,k}$ ) may be increased by a factor  $k = 1,40$  (EN 14080 clause 5.1.3).

Property	Symbol	Glulam strength class						
		GL 20h	GL 22h	GL 24h	GL 26h	GL 28h	GL 30h	GL 32h
Bending strength	$f_{m,g,k}$	20	22	24	26	28	30	32
Tensile strength	$f_{t,0,g,k}$	16	17,6	19,2	20,8	22,3	24	25,6
	$f_{t,90,g,k}$	0,5						
Compression strength	$f_{c,0,g,k}$	20	22	24	26	28	30	32
	$f_{c,90,g,k}$	2,5						
Shear strength (shear and torsion)	$f_{v,g,k}$	3,5						
Rolling shear strength	$f_{r,g,k}$	1,2						
Modulus of elasticity	$E_{0,g,mean}$	8 400	10 500	11 500	12 100	12 600	13 600	14 200
	$E_{0,g,05}$	7 000	8 800	9 600	10 100	10 500	11 300	11 800
	$E_{90,g,mean}$	300						
	$E_{90,g,05}$	250						
Shear modulus	$G_{g,mean}$	650						
	$G_{g,05}$	540						
Rolling shear modulus	$G_{r,g,mean}$	65						
	$G_{r,g,05}$	54						
Density	$\rho_{g,k}$	340	370	385	405	425	430	440
	$\rho_{g,mean}$	370	410	420	445	460	480	490

Table 3.4: Characteristic properties of glulam (EN 14080 clause 5.1.4)

## 3.2 Laminated Veneer Lumber

Properties of Laminated Veneer Lumber (LVL) are given in Table 3.5. To keep the overview simple, only the properties of loads flatwise and parallel to the grain are given (described in draft version of EN 14374).

For depths in bending not equal to 300 mm the characteristic bending strength should be multiplied by the factor  $k_h$  (EN 1995-1-1 clause 3.4):

$$k_h = \min \left( \left( \frac{300}{h} \right)^s ; 1.2 \right) \quad (3.4)$$

Where the size exponent  $s = 0.15$  (Table 3.5).

			Strength class				
Property		Symbol	Unit	LVL 32 S	LVL 50 S	LVL 52 S	LVL 80 S
Bending strength	Flatwise, parallel to grain	$f_{m,0,flat,k}$	N/mm <sup>2</sup>	32	50	52	80
	Size effect parameter	$s$	-	0,15	0,15	0,15	0,15
Tension strength	Parallel to grain (length 3 000 mm)	$f_{t,0,k}$	N/mm <sup>2</sup>	24	35	42	60
Compression strength	Parallel to grain	$f_{c,0,k}$	N/mm <sup>2</sup>	26	35	56	57,5
Shear strength	Flatwise, parallel to grain	$f_{v,0,flat,k}$	N/mm <sup>2</sup>	1,3	2,3	3,2	8
TModulus of elasticity	Parallel to grain	$E_{0,mean}^a$	N/mm <sup>2</sup>	10 000	13 800	15 600	16 800
	Parallel to grain	$E_{0,k}^b$	N/mm <sup>2</sup>	8 800	11 600	14 000	14 900
Shear modulus	Flatwise, parallel to grain	$G_{0,flat,mean}$	N/mm <sup>2</sup>	400 <sup>e</sup>	500	500	850
	Flatwise, parallel to grain	$G_{0,flat,k}$	N/mm <sup>2</sup>	300 <sup>e</sup>	400	400	760
Density		$\rho_{mean}$	kg/m <sup>3</sup>	440	510	580	800
		$\rho_k$	kg/m <sup>3</sup>	410	480	550	730
<sup>a</sup> Covering $E_{m,0,edge,mean}$ , $E_{t,0,mean}$ , $E_{m,0,flat,mean}$ , and $E_{c,0,mean}$ <sup>b</sup> Covering $E_{m,0,edge,k}$ , $E_{t,0,k}$ , $E_{m,0,flat,k}$ , and $E_{c,0,k}$ <sup>c</sup> Covering $E_{t,90,edge,mean}$ , $E_{c,90,edge,mean}$ <sup>d</sup> Covering $E_{t,90,edge,k}$ , $E_{c,90,edge,k}$ <sup>e</sup> Values need not to be verified within type testing.							

Table 3.5: Characteristic properties of LVL (EN 14374 clause B.2)

# 4. Loads

## 4.1 Global loads

This section presents which loads are exerted on the deck for different limit states and combinations. All loads are calculated for a reference width of 1 meter.

### 4.1.1 Permanent actions ( $G_k$ )

Permanent actions are composed of selfweight. The bridge super structure exists of the timber deck, the asphalt layer and further finishing like curbs and railings. Estimation of the total dead load per  $\text{m}^2$  is presented in Table 4.1. The volume of the timber is assumed to be equal to a surface of  $1 \text{ m}^2$  with a thickness of  $t$ .

	Density ( $\rho$ ) [ $\text{kN}/\text{m}^3$ ]	Thickness ( $t$ ) [mm]	Weight ( $\rho \cdot t$ ) [ $\text{kN}/\text{m}^2$ ]
Timber	5	$h$	$5h$
Asphalt	22	140	3.1
Finishing			1.0 (assumption)
$G_k$			$5h + 4.1$

Table 4.1: Selfweight of the deck

### 4.1.2 Leading variable actions ( $Q_{k,1}$ )

The leading variable action is the traffic load on the bridge. Traffic loads are defined in NEN-EN 1991-2, they are composed of Several Load Models (LM). LM1 comprises most of the general traffic loads. For simplicity, only LM1 is used for verification. LM1 exists of **Tandem Systems** (TS) and **Uniformly Distributed Loads** (UDL). Values are given in Table 4.2. This results in a bridge cross-section that is loaded like in Figure 4.1.

Location	Tandem system <i>TS</i>	<i>UDL</i> system
	Axle loads $Q_{ik}$ (kN)	$\alpha_{q_i} q_{ik}$ (or $q_{ik}$ ) (kN/m <sup>2</sup> ) $\alpha_{q_i}$
Lane Number 1	300	9
Lane Number 2	200	2,5
Lane Number 3	100	2,5
Other lanes	0	2,5
Remaining area ( $q_k$ )	0	2,5

Table 4.2: Characteristic values for Load Model 1 (NEN-EN 1991-2 table 4.2)

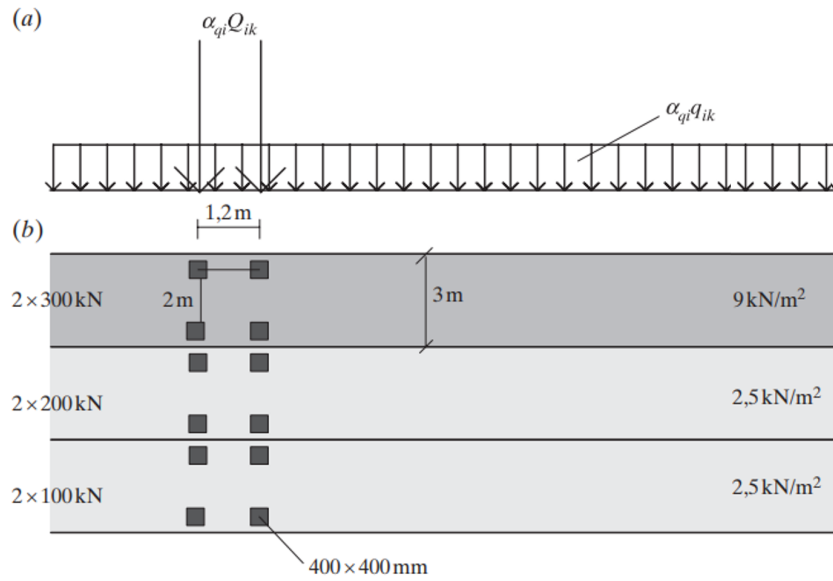


Figure 4.1: Load model 1. (a) side view. (b) top view. [43]

## 4.2 Ultimate limit state

In ULS, the characteristic actions must be multiplied with partial factors  $\gamma$  to take into account uncertainties. NEN-EN 1990 equation 6.10 is used for ULS load combination, see Equation 4.1. Corresponding  $\gamma$  values are taken from NEN-EN 1990 table A1.2(B).

$$E_d = \sum_{j \geq 1} \gamma_{G,j} G_{k,j} + \gamma_P P + \gamma_{Q,1} Q_{k,1} + \sum_{i > 1} \gamma_{Q,i} \psi_{0,i} Q_{k,i} \quad (4.1)$$

$\gamma_{G,j} = 1.35$  where unfavourable (1.00 where favourable)

$\gamma_{Q,i} = 1.5$  where unfavourable (0.0 where favourable)

Equation 4.2 gives the resulting design actions:

$$E_{d,ULS} = \overbrace{\gamma_G \cdot G_k}^{\text{selfweight}} + \overbrace{\gamma_{Q,1} \cdot q_{k,1}}^{\text{traffic-UDL}} + \overbrace{\gamma_{Q,1} \cdot Q_{k,1}}^{\text{traffic-TS}} \quad (4.2)$$

Where:

$G_k$  is the selfweight of the bridge deck

$q_{k,1}$  is the UDL from LM1

$Q_{k,1}$  is the TS from LM1

### 4.2.1 ULS load configuration

Global bending moments are calculated with the loads that are presented on previous pages. The bridge deck is continuous over the mid support and can freely rotate. A continuous deck will have a maximum hogging bending moment at the mid support and a maximum sagging bending moment somewhere at the midspan of span 1. Both the governing hogging- and sagging bending moments are calculated below. Afterwards, a load envelope can be created.

#### hogging bending moment

Loads on span 1 and span 2 will both increase the hogging bending moment. Therefore, all loads are unfavourable:  $\gamma_G = 1.35$  and  $\gamma_{Q,1} = 1.5$ . The total q-load over both spans consists of the selfweight and the traffic load:  $\gamma_G G_k + \gamma_{Q,1} q_{k,1}$ . The TS consists of  $\gamma_{Q,1} Q_{k,1}$ . For simplicity, the two point loads  $Q_{k,1}$  are taken together. According to influence line theory, maximum hogging bending moment is obtained when the TS is located at  $0.58L$  from the left support. Governing load configuration for maximum hogging bending moment at the middle support is sketched in Figure 4.2. Where:

$$\gamma_G G_k + \gamma_{Q,1} q_{k,1} = 1.35(5h + 4.1) + 1.5 \cdot 9$$

$$\gamma_{Q,1} Q_{k,1} = 1.5 \cdot 200 = 300 \text{ kN}$$

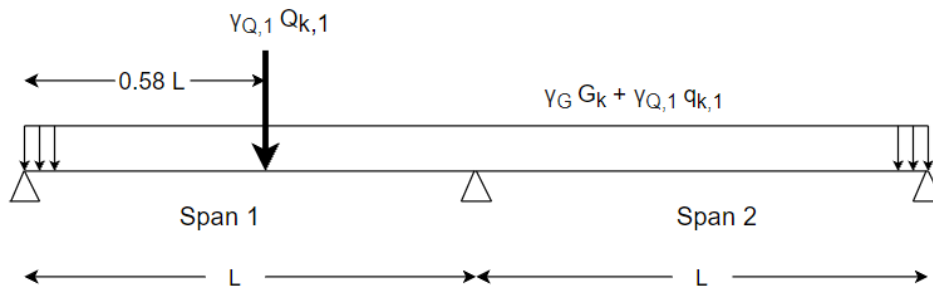


Figure 4.2: ULS loads for max hogging moment at middle support

**sagging bending moment**

The maximum sagging moment is obtained when the q-load on span 1 is highest and the q-load on span 2 is lowest. Therefore, q-load on span 1 is unfavourable:  $\gamma_G = 1.35$  and  $\gamma_{Q,1} = 1.5$ , and q-load on span 2 is favourable:  $\gamma_G = 1.0$  and  $\gamma_{Q,1} = 0.0$ . The TS consists of  $\gamma_{Q,1}Q_k$ , where  $\gamma_{Q,1} = 1.5$ . According to influence line theory, maximum sagging moment is obtained when the TS is located  $0.43L$  from the left support. Governing load configuration for maximum sagging moment at midspan is sketched in Figure 4.3, Where:

**Span 1:**

$$\gamma_G G_k + \gamma_{Q,1} q_{k,1} = 1.35(5h + 4.1) + 1.5 \cdot 9$$

$$\gamma_{Q,1} Q_{k,1} = 1.5 \cdot 200 = 300 \text{ kN}$$

**Span 2:**

$$\gamma_G G_k = 1.0(5h + 4.1)$$

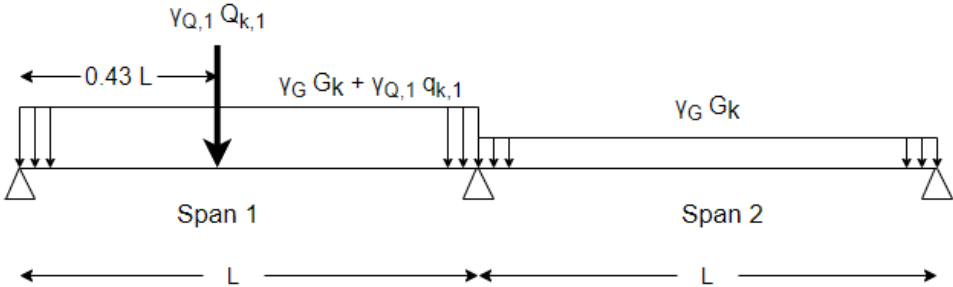


Figure 4.3: ULS loads for max sagging moment at midspan

**4.2.2 ULS bending moments**

The load configurations from previous sections are taken into account to find the governing moments on the bridge deck. The moment on 1 meter width of the highest loaded lane is calculated, see Figure 4.4. It should be noted that this is a conservative approach. In reality, the loads are distributed over a larger part of the deck width.

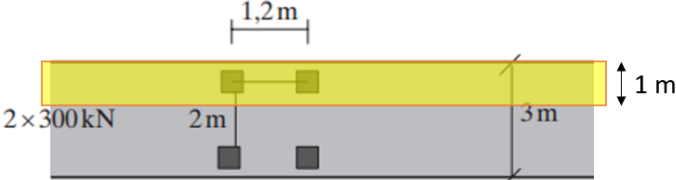


Figure 4.4: Surface of 1 meter width (in yellow) taken into account for bending moment calculation

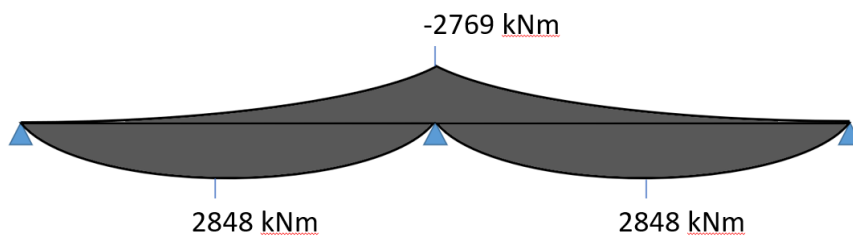
This gives load values as presented in Table 4.3. It should be noted that using these load values is a conservative approximation because there is no distribution over the width of the bridge deck.

$$\begin{aligned} G_k &= (5 h + 4.1) \\ q_k &= 9 \text{ kN/m} \\ Q_k &= 200 \text{ kN}^{[1]} \end{aligned}$$

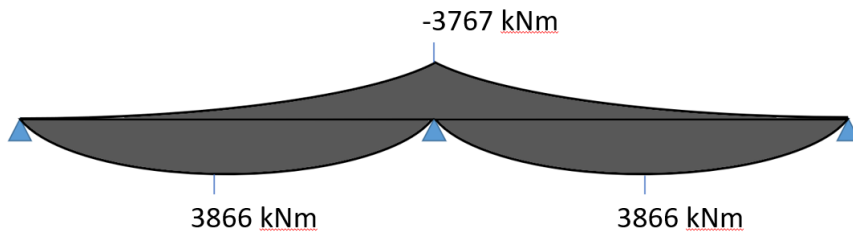
<sup>[1]</sup> 1/3 of the 2x300kN that is exerted on the lane

Table 4.3: Governing load values

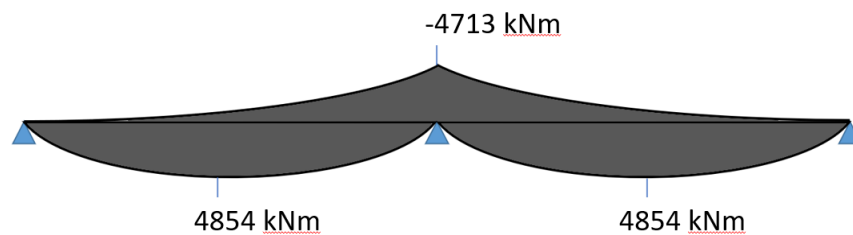
Using the load configurations (section 4.2.1), the maximum ULS hogging and sagging bending moments are calculated for 1 meter width. This is done using MatrixFrame. The load envelope is dependent on the spans of the bridge. The final ULS envelopes with maximum bending moments is presented for spans of 25, 30 and 35 meters in Figures 4.5.



(a) Load envelope for L = 25 m



(b) Load envelope for L = 30 m



(c) Load envelope for L = 35 m

Figure 4.5: ULS load envelopes, bending moments are displayed in kNm per meter width of the deck

### 4.3 Serviceability limit state

For SLS, no partial factors need to be taken into account. Equation 4.3 gives the resulting design actions.

$$E_{d,SLS} = G_k + q_{k,1} + Q_{k,1} \quad (4.3)$$

As said in previous section, these load values are conservative. The SLS load model is also used for the deflection. Using conservative loads for the SLS load model will represent a situation of small occurrence. Besides, Eurocode does not give mandatory deflection limits. Which means that it would not matter that the deflection becomes large. This is discussed later in the report.

#### hogging bending moment

Governing hogging load configuration is the same as presented for ULS (without  $\gamma$  factors). For maximum hogging moment at the middle support, distributed load is  $G_k + q_{k,1}$  on both spans and point load is  $Q_{k,1}$ :

$$G_k + q_{k,1} = (5h + 4.1) + 9$$

$$Q_{k,1} = 200 \text{ kN}$$

#### sagging bending moment

For maximum sagging bending moment, loads on the left span should be high and loads on right span should be low. Loads on the left span are  $G_k + q_{k,1}$  and  $Q_{k,1}$ . Loads on right span exist of only  $G_k$ :

##### Span 1:

$$G_k + q_{k,1} = (5h + 4.1) + 9$$

$$Q_{k,1} = 200 \text{ kN}$$

##### Span 2:

$$G_k = (5h + 4.1)$$

SLS bending moment envelopes are presented in Figure 4.6 for spans of 25, 30 and 35 meters



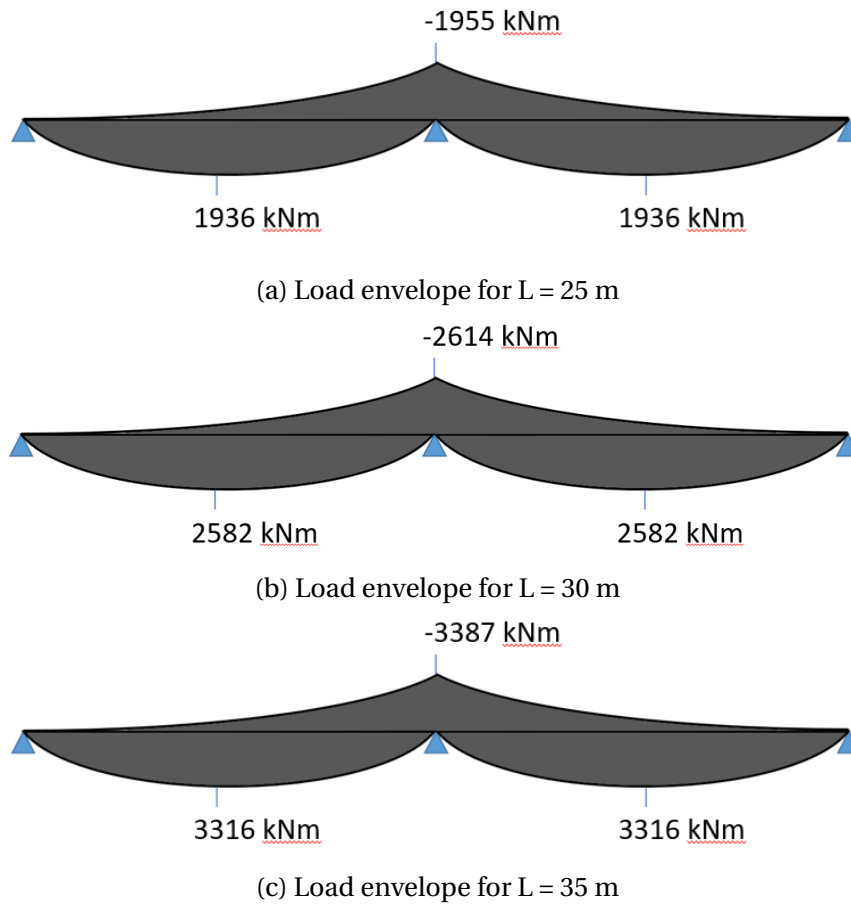


Figure 4.6: SLS load envelopes, bending moments are displayed in kNm per meter width of the deck

## 4.4 Loads for creep

It is assumed that short-term loads do not influence the creep behaviour of the bridge deck. The selfweight of the bridge is always present and will induce creep. However, only taking into account the selfweight for creep deflections might be too optimistic because some lighter traffic loads are present for large fractions of the time. For a conservative approximation, also the smaller UDL traffic load is taken into account for the creep calculations, see Equation 4.4.

$$E_{d,creep} = G_k + q_{k,1} \quad (4.4)$$

The load configuration for creep is presented in Figure 4.7, where:

$$G_k = (5h + 4.1)$$

$$q_{k,1} = 2.5 \text{ kN/m}$$

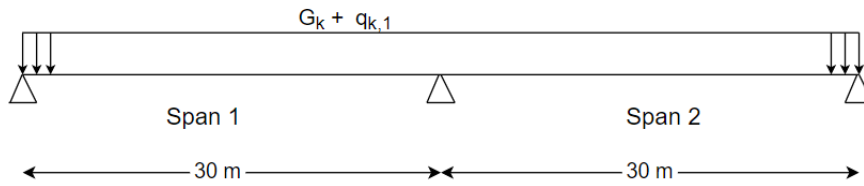


Figure 4.7: Creep load configuration

## 4.5 Guidelines for deflection

For timber design, often the deflections are governing for the cross-sectional dimensions due to its low modulus of elasticity. Eurocode gives several values for the maximum deflection of timber beams and deck systems. It is important to note it is not required to meet these values. The values for beams on two supports from EN 1995-1-1 section 7.2 are given in Equation 4.5. It should be noted that these values are given for beams, which have in general much smaller spans than the 30 meters used in this research.

$$w_{fin} = L/300 - L/150 = 100 - 200mm \quad (4.5)$$

EN 1995-2 gives deflection values specifically for timber bridges. These values are much more strict than the limits from EN 1995-1-1. The deflection values for beams, plates and trusses in timber bridges are given in Equation 4.6.

$$w_{fin} = L/500 - L/400 = 60 - 75mm \quad (4.6)$$

It should be noted that the deflections in Equation 4.6 are not mandatory for bridge design. They are just used as a guideline for this research.

## 5. Cross-sectional Model

Two models are developed in Python to analyse the Initial behaviour of reinforced- and prestressed cross-sections. The first model focuses on a reinforced cross-section (where the reinforcement material is not prestressed). The second model focuses on a prestressed cross-section (where also prestressed material is added to the timber cross-section). The models are used to find the final moment resistance of the timber deck. To quantify the long-term behaviour, the prestress losses calculated with the model in Chapter 7 will be substituted in the Python model to find the decrease in moment resistance over time.

### 5.1 Model description

The reinforcement model was developed first. Afterwards, the reinforcement model was extended to also make it suitable to a prestressed cross-section. In the models, the curvature of the cross-section starts at 0 and is increased incrementally. Using this approach, the deck behaviour can be quantified during the entire loading path (i.e. from zero load up to elastic limit, up to plastification, up to ultimate failure). Corresponding strains within the cross-section can be computed for every curvature increment. Then, stresses in the glulam and reinforcement/prestress material can be calculated using the constitutive relations. The stress-strain relationship for timber that is used in the model is presented in Figure 5.1. This stress-strain relation is based on the elastic-perfectly-plastic concept, as used by Klinger et al [25] and Blaß and Romani [27]. In tension, the stress increases linearly up to the tension strength  $f_{t,y,gl}$ , after which brittle failure happens. In compression, the stress increases linearly up to the yield strength  $f_{c,y,gl}$ . After this point, plastic deformation happens and the stresses remain constant. This means that ductility is included, since the material still has strength after yielding. No ultimate plastic strain is built into the model yet.

### 5.2 Model for reinforced cross-section

The reinforced model is based on the cross-section as sketched in Figure 5.2. The curvature  $\chi$  is increased incrementally. For every small step, the strains in the cross-section can be calculated from the curvature:

$$\epsilon_{t,gl} = \chi \cdot y_2$$

$$\epsilon_{c,gl} = -\chi \cdot y_1$$

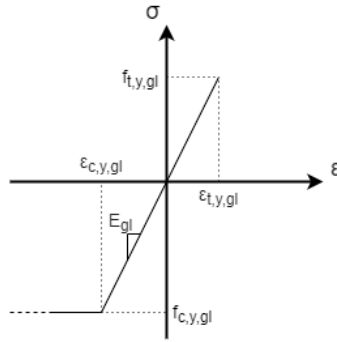


Figure 5.1: Timber stress-strain relationship used for the models

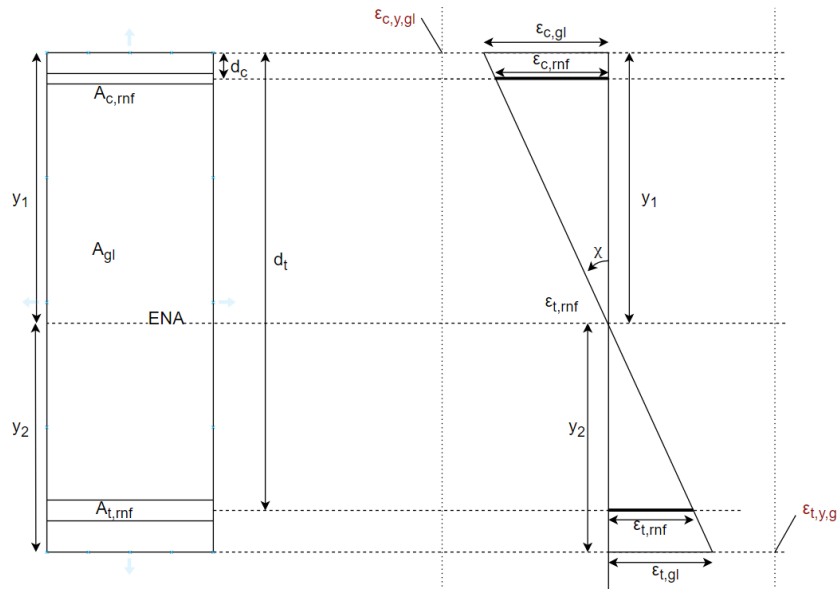


Figure 5.2: Load application on a reinforced cross-section

### 5.2.1 Cross-sectional properties

The Elastic Neutral Axis (ENA) is calculated as the distance  $y_1$  from the upper side of the deck. Following equations are used to find  $y_1$  and  $y_2$ :

$$y_1 = \frac{\sum A_i y_i}{\sum A_i} \quad (5.1a)$$

$$y_2 = h_{gl} - y_1 \quad (5.1b)$$

Where  $A_i$  is the area of each material (timber or reinforcement), and  $y_i$  is the distance from the top of the deck to the centroid of the material.

## 5.2.2 Elastic equations

Based on  $\epsilon_{t,gl}$ , the rest of the strains on the cross-section can be calculated using similar triangles:

$$\epsilon_{t,rnf} = \frac{\epsilon_{t,gl}}{y_2}(d_t - y_1)$$

$$\epsilon_{c,gl} = -\frac{\epsilon_{t,gl}}{y_2}y_1$$

$$\epsilon_{c,rnf} = -\frac{\epsilon_{t,gl}}{y_2}(y_1 - d_c)$$

The corresponding forces and moment are determined as follows (it should be noted that these equations are a function of the curvature  $\chi$ ):

$$F_{t,gl} = \frac{1}{2}\epsilon_{t,gl} \cdot E_{gl} \cdot b_{gl} \cdot y_2$$

$$F_{t,rnf} = \epsilon_{t,rnf} \cdot E_{rnf} \cdot A_{t,rnf}$$

$$F_{c,gl} = \frac{1}{2}\epsilon_{c,gl} \cdot E_{gl} \cdot b_{gl} \cdot y_1$$

$$F_{c,rnf} = \epsilon_{c,rnf} \cdot E_{rnf} \cdot A_{c,rnf}$$

$$M_{el} = -F_{c,rnf} \cdot (y_1 - d_c) - F_{c,gl} \cdot \frac{2}{3}y_1 + F_{t,gl} \cdot \frac{2}{3}y_2 + F_{t,rnf} \cdot (d_t - y_1)$$

The elastic limit strains in Figure 5.2 are calculated as follows:

$$\epsilon_{t,y,gl} = \frac{f_{t,y,gl}}{E_{gl}}$$

$$\epsilon_{c,y,gl} = \frac{f_{c,y,gl}}{E_{gl}}$$

### Elastic tension failure

If on the strains  $\epsilon_{t,gl}$  or  $\epsilon_{c,gl}$  reaches the limit strains, a failure mode occurs. If the tension strain  $\epsilon_{t,gl}$  reaches the limit first, a brittle failure occurs. In this case, an elastic limit moment is calculated based on  $\epsilon_{t,y,gl}$ :

$$\epsilon_{t,rnf} = \frac{\epsilon_{t,y,gl}}{y_2}(d_t - y_1)$$

$$\epsilon_{c,gl} = -\frac{\epsilon_{t,y,gl}}{y_2}y_1$$

$$\epsilon_{c,rnf} = -\frac{\epsilon_{t,y,gl}}{y_2}(y_1 - d_c)$$

$$F_{t,gl} = \frac{1}{2}\epsilon_{t,y,gl} \cdot E_{gl} \cdot b_{gl} \cdot y_2$$

$$F_{t,rnf} = \epsilon_{t,rnf} \cdot E_{rnf} \cdot A_{t,rnf}$$

$$F_{c,gl} = \frac{1}{2}\epsilon_{c,gl} \cdot E_{gl} \cdot b_{gl} \cdot y_1$$

$$F_{c,rnf} = \epsilon_{c,rnf} \cdot E_{rnf} \cdot A_{c,rnf}$$

$$M_{t,el,lim} = -F_{c,rnf} \cdot (y_1 - d_c) - F_{c,gl} \cdot \frac{2}{3}y_1 + F_{t,rnf} \cdot (y_2 - (h_{gl} - d_t)) + F_{t,gl} \cdot \frac{2}{3}y_2$$

### Elastic compression limit

If the compression strain reaches the limit strain before the tension strain reaches the limit, the elastic limit moment is calculated based on  $\epsilon_{c,y,gl}$ :

$$\epsilon_{c,rnf} = \frac{\epsilon_{c,y,gl}}{y_1}(y_1 - d_c)$$

$$\epsilon_{t,gl} = -\frac{\epsilon_{c,y,gl}}{y_1}y_2$$

$$\epsilon_{t,rnf} = -\frac{\epsilon_{c,y,gl}}{y_1}(d_t - y_1)$$

$$F_{c,gl} = \frac{1}{2}\epsilon_{c,y,gl} \cdot E_{gl} \cdot b_{gl} \cdot y_1$$

$$F_{c,rnf} = \epsilon_{c,rnf} \cdot E_{rnf} \cdot A_{c,rnf}$$

$$F_{t,gl} = \frac{1}{2}\epsilon_{t,gl} \cdot E_{gl} \cdot b_{gl} \cdot y_2$$

$$F_{t,rnf} = \epsilon_{t,rnf} \cdot E_{rnf} \cdot A_{t,rnf}$$

$$M_{c,el,lim} = F_{t,rnf} \cdot (y_2 - (h_{gl} - d_t)) + F_{t,gl} \cdot \frac{2}{3}y_2 - F_{c,rnf} \cdot (y_1 - d_c) - F_{c,gl} \cdot \frac{2}{3}y_1$$

### 5.2.3 Plastic equations

Further increasing the curvature  $\chi$  after  $\epsilon_{c,y,gl}$  is reached, will lead to a ductile failure mode. In that case, plastification of the compression side occurs (Figure 5.3). Because of plastic stresses, the ENA shifts downwards to a Plastic Neutral Axis (PNA) for every increment of  $\chi$ . The location of the PNA can be calculated based on equilibrium of forces in the cross-section. Following equations are used to find a new  $y_1$  from equilibrium:

$$\epsilon_{t,gl} = \chi(h_{gl} - y_1)$$

$$\epsilon_{t,rnf} = \chi(d_t - y_1)$$

$$\epsilon_{c,rnf} = -\chi(y_1 - d_c)$$

$$F_{c,gl,pl} = f_{c,y,gl} \cdot b_{gl} \cdot h_{pl}, \quad \text{where } h_{pl} = (y_1 - y_{c,y,gl})$$

$$F_{c,gl,el} = \frac{1}{2}E_{gl} \cdot f_{c,y,gl} \cdot b_{gl} \cdot y_{c,y,gl}$$

$$F_{c,rnf} = E_{rnf} \cdot \epsilon_{c,rnf} \cdot A_{c,rnf}$$

$$F_{t,gl} = \frac{1}{2}E_{gl} \cdot \epsilon_{t,gl} \cdot b_{gl} \cdot (h_{gl} - y_1)$$

$$F_{t,rnf} = E_{rnf} \cdot \epsilon_{t,rnf} \cdot A_{t,rnf}$$

$y_1$  can be calculated from force equilibrium:

$$F_{t,gl} + F_{t,rnf} + F_{c,gl,el} + F_{c,gl,pl} + F_{c,rnf} = 0$$

Then,  $y_2 = h_{gl} - y_1$

The corresponding moment is calculated as follows:

$$M_{pl} = -F_{c,gl,pl} \cdot (y_1 - \frac{1}{2}h_{pl}) - F_{c,gl,el} \cdot \frac{2}{3}y_{c,y,gl} - F_{c,rnf} \cdot (y_1 - d_c) + F_{t,gl} \cdot \frac{2}{3}y_2 + F_{t,rnf} \cdot (d_t - y_1)$$

### Tension failure when plastic compression already occurred

The curvature is increased further up to the point where the tension strain  $\epsilon_{t,gl}$  reaches the elastic limit strain  $\epsilon_{t,y,gl}$ , this point is modelled as the plastic limit of the cross-section. The final curvature  $\chi_{pl,lim}$  at plastic failure is calculated based on equilibrium of forces:

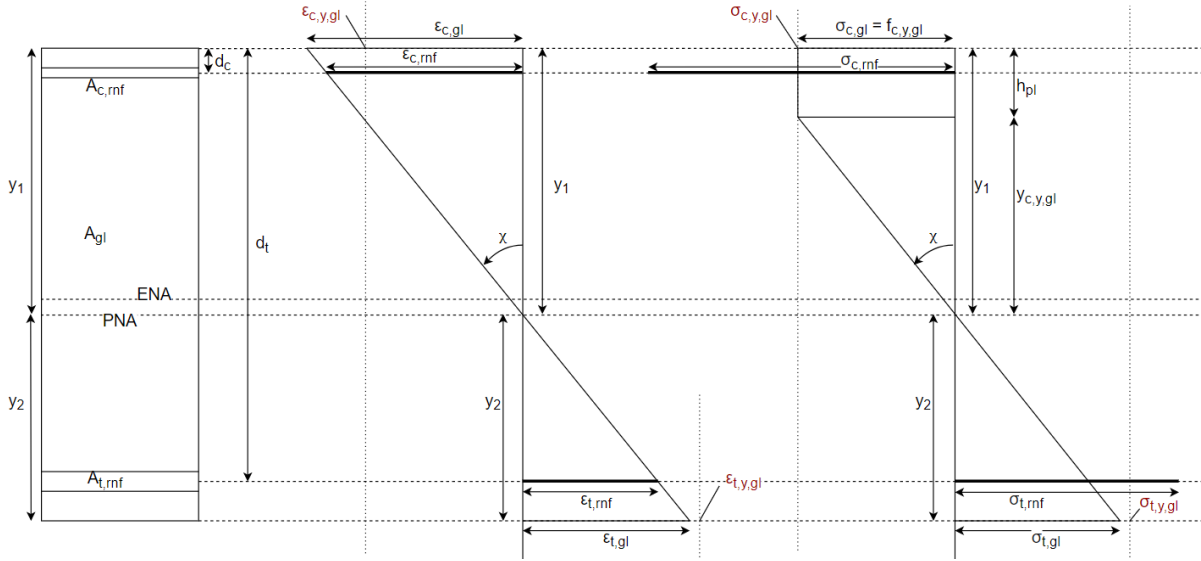


Figure 5.3: Plastic stresses on a reinforced cross-section

The tension limit strain  $\epsilon_{t,y,gl}$  is known,  $y_1$  and  $y_2$  as a function of  $\chi_{pl,lim}$ :

$$y_2 = \frac{\epsilon_{t,y,gl}}{\chi_{pl,lim}} y_1 = h_{gl} - y_2$$

$$\epsilon_{t,rnf} = \frac{\epsilon_{t,y,gl}}{y_2} (d_t - y_1)$$

$$\epsilon_{c,rnf} = -\frac{\epsilon_{t,y,gl}}{y_2} (y_1 - d_c)$$

$$y_{c,y,gl} = -\frac{\epsilon_{c,y,gl}}{\chi_{pl,lim}}$$

$$h_{pl} = y_1 - y_{c,y,gl}$$

$$F_{c,gl,pl} = f_{c,y,gl} \cdot b_{gl} \cdot h_{pl}$$

$$F_{c,gl,el} = \frac{1}{2} f_{c,y,gl} \cdot b_{gl} \cdot y_{c,y,gl}$$

$$F_{c,rnf} = E_{rnf} \cdot \epsilon_{c,rnf} \cdot A_{t,rnf}$$

$$F_{t,rnf} = E_{rnf} \cdot \epsilon_{t,rnf} \cdot A_{t,rnf}$$

$$F_{t,gl} = \frac{1}{2} E_{gl} \cdot \epsilon_{t,y,gl} \cdot b_{gl} \cdot y_2$$

$\chi_{pl,lim}$  can be calculated from force equilibrium:

$$F_{t,gl} + F_{t,rnf} + F_{c,rnf} + F_{c,el,gl} + F_{c,pl,gl} = 0$$

Then, the ultimate limit moment is calculated as follows:

$$M_{pl,lim} = -F_{c,gl,pl} \cdot (y_1 - \frac{1}{2} h_{pl}) - F_{c,gl,el} \cdot \frac{2}{3} y_{c,y,gl} - F_{c,rnf} \cdot (y_1 - d_c) + F_{t,gl} \cdot \frac{2}{3} y_2 + F_{t,rnf} \cdot (d_t - y_1)$$

### 5.3 Model for prestressed cross-section

The model for a reinforced cross-section (Section 5.2) is extended to also be able to analyse a prestressed cross-section. Besides tension reinforcement, also prestress material is present in the bottom. The prestress material with surface  $A_p$  is subjected to an initial prestress force. So in the first stage, only the forces from prestress are exerted on the cross-section of the deck. Corresponding strains are displayed in Figure 5.4. It should be noted that the  $ENA_p$  is calculated based on only  $A_{c,rnf}$ ,  $A_{t,rnf}$  and  $A_{gl}$  and their stiffnesses, so basically the same as in Figure 5.2.  $A_p$  is not taken into account yet because the prestressed material only exerts a force on the cross-section, it does not contribute to the stiffness properties yet. From the point of applying action loads on the cross-section,  $A_p$  will also be taken into account to determine a new ENA.

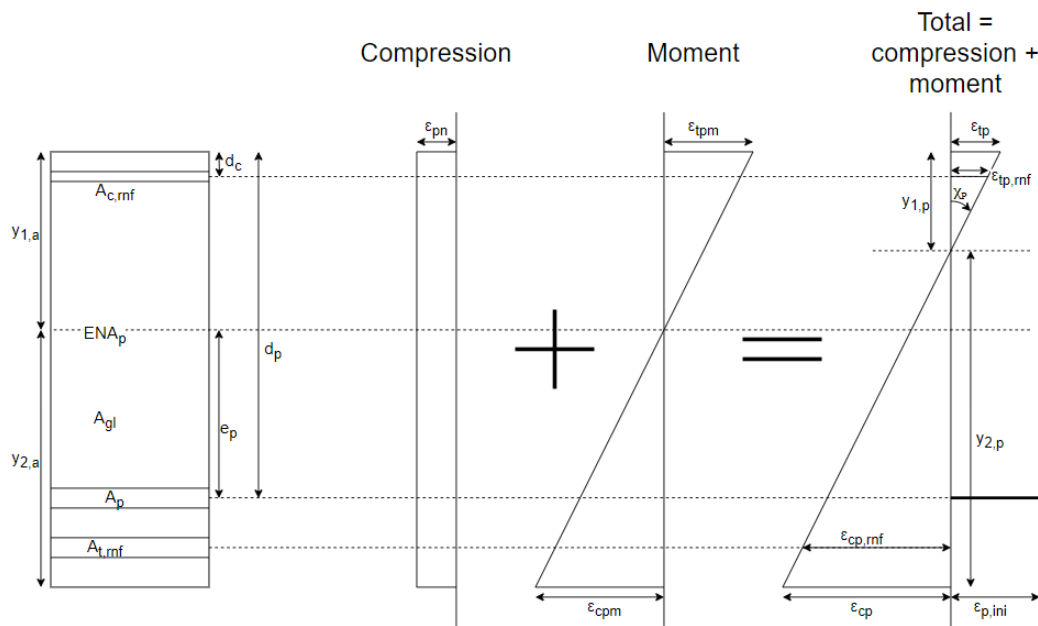


Figure 5.4: Strains due to prestress force only

$$e_p = d_p - y_{1,a}$$

$$M_p = -P \cdot e_p$$

Where the prestress force  $P$  is applied to the bottom reinforcement.

$$\sigma_{p,ini} = \frac{P}{A_{t,rnf}}$$

$$\epsilon_{p,ini} = \frac{\sigma_{p,ini}}{E_{rnf}}$$

Compression due to  $P$ :

$$\epsilon_{pn} = \frac{-P}{EA_{eff,p}}$$

$$\sigma_{pn,gl} = \epsilon_{pn} \cdot E_{gl}$$



Where  $EA_{eff,p}$  is calculated according to Equation 5.2a.  $EA_{eff,p}$  is based on the location of ENA<sub>p</sub>. So on  $A_{c,rnf}$ ,  $A_{t,rnf}$  and  $A_{gl}$ , the prestress material is not taken into account.

$$EA_{eff} = \sum E_i A_i \quad (5.2a)$$

$$EI_{eff} = \sum E_i \left( \frac{1}{12} b_i h_i^3 + A_i y_i^2 \right) \quad (5.2b)$$

Moment due to  $P$ :

$$\epsilon_{tpm} = \frac{M_p \cdot -y_{1,a}}{EI_{eff,p}}$$

$$\sigma_{tpm,gl} = \epsilon_{tpm} \cdot E_{gl}$$

$$\epsilon_{cpm} = \frac{M_p \cdot y_{2,a}}{EI_{eff,p}}$$

$$\sigma_{cpm,gl} = \epsilon_{cpm} \cdot E_{gl}$$

Where  $EI_{eff,p}$  is calculated according to Equation 5.2b. Not taking into account the prestress material, same as for  $EA_{eff,p}$ .

Total strains and stresses due to  $P$ :

$$\epsilon_{tp} = \epsilon_{pn} + \epsilon_{tpm}$$

$$\sigma_{tp,gl} = \epsilon_{tp} \cdot E_{gl}$$

$$\epsilon_{cp} = \epsilon_{pn} + \epsilon_{cpm}$$

$$\sigma_{cp,gl} = \epsilon_{cp} \cdot E_{gl}$$

$$\epsilon_{tp,rnf} = \frac{\epsilon_{tpm}}{y_{1,a}} (y_{1,a} - d_c) + \epsilon_{pn}$$

$$\epsilon_{cp,rnf} = -\frac{\epsilon_{cpm}}{y_{1,a}} (d_t - y_{1,a}) + \epsilon_{pn}$$

Neutral axis after prestress transfer:

$$y_{1,p} = \frac{h_{gl} \cdot \epsilon_{tp}}{\epsilon_{tp} - \epsilon_{cp}}$$

$$y_{2,p} = \frac{h_{gl} \cdot -\epsilon_{cp}}{\epsilon_{tp} - \epsilon_{cp}} = h_{gl} - y_{1,p}$$

Initial curvature due to  $P$ :

$$\chi_P = -\frac{\epsilon_{tp}}{y_{1,p}} = \frac{\epsilon_{cp}}{y_{2,p}}$$

### 5.3.1 Zero tension at bottom fibre

After prestress application, the curvature is incrementally increased (same concept as in the reinforced model). Meaning that for every increment, the action moment is increased by a small step. From this moment on, the prestressed material also contributes to the stiffness of the cross-section. Meaning that a new neutral axis should be calculated. It shifts from the initial one ( $ENA_p$ ) based on only the prestress force, to the ENA that also takes into account the prestress material:  $A_{c,rnf}$ ,  $A_{gl}$ ,  $A_{t,rnf}$  and also  $A_p$  and their stiffnesses. In the model, the curvature is incrementally increasing up to the moment where the total strain in the bottom is zero again. This requires the bottom strain  $\epsilon_{t,gl}$  to be opposite of the bottom strain due to prestress (Figure 5.5):

$$\epsilon_{t,gl} = -\epsilon_{cp}$$

$\chi$  is the running curvature corresponding to the action moment.  $\chi_t$  is the total curvature i.e. the curvature due to the action moment and the prestress load together. Which is calculated as follows:

$$\chi_t = \chi_P + \chi$$

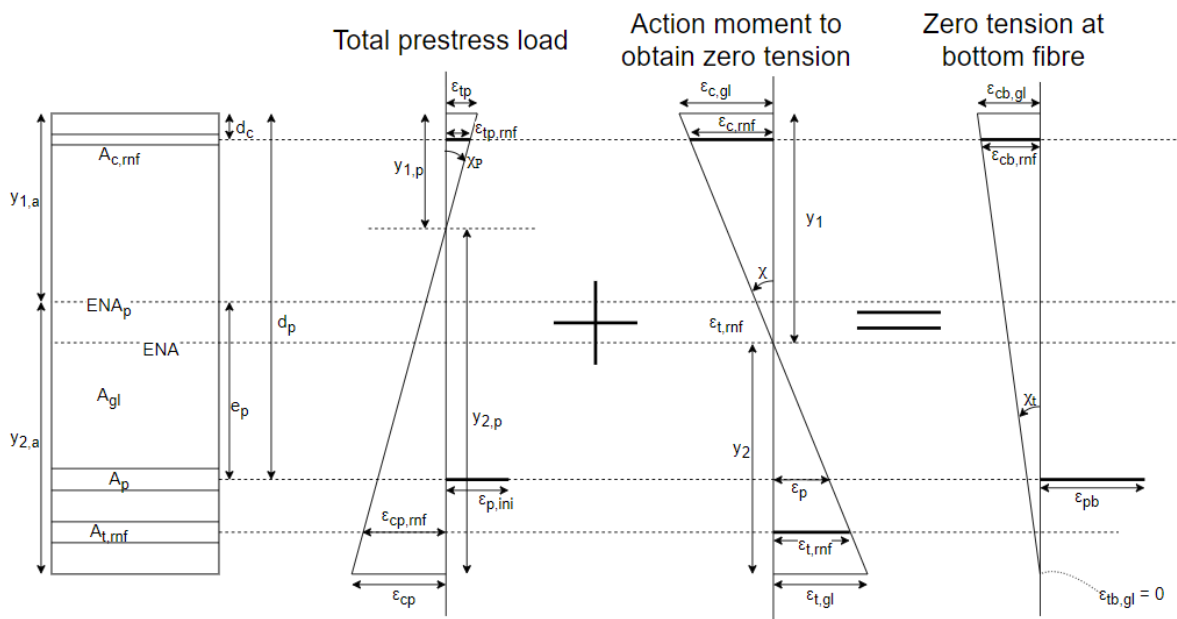


Figure 5.5: Sum of prestress and action moment to obtain zero strain at tension fibre

Based on  $\epsilon_{t,gl}$ , the rest of the strains on the cross-section can be calculated. These strains are based on the action moment only:

$$\epsilon_{t,rnf} = \frac{\epsilon_{t,gl}}{y_2} (d_t - y_1)$$

$$\epsilon_{c,gl} = -\frac{\epsilon_{t,gl}}{y_1} y_1$$

$$\epsilon_{c,rnf} = -\frac{\epsilon_{t,gl}}{y_2}(y_1 - d_c)$$

$$\epsilon_p = \frac{\epsilon_{t,gl}}{y_2}(d_p - y_1)$$

Now, the zero tension situation can be quantified:

$$\epsilon_{tb,gl} = \epsilon_{cp} + \epsilon_{t,gl} = 0$$

$$\epsilon_{tb,rnf} = \epsilon_{cp,rnf} + \epsilon_{t,rnf}$$

$$\epsilon_{cb,rnf} = \epsilon_{tp,rnf} + \epsilon_{c,rnf}$$

$$\epsilon_{cb,gl} = \epsilon_{tp} + \epsilon_{c,gl}$$

$$\epsilon_{pb} = \epsilon_{p,ini} + \epsilon_p$$

### 5.3.2 Up to elastic limit

From the zero tension situation, the curvature is incrementally increased up to the moment where the strain reaches the elastic limit strain  $\epsilon_{c,y,gl}$ . The elastic limit is shown in Figure 5.6, where the elastic limit for compression is reached. It is important to note that the quantities  $\epsilon_{cb,gl}$ ,  $\epsilon_{cb,rnf}$ ,  $\epsilon_{tb,rnf}$ ,  $\epsilon_{tb,gl}$  and  $\epsilon_{pb}$  denote the actual strain on the cross-section, which is a result of the prestress load and the load due to actions. And that the quantities  $\epsilon_{c,gl}$ ,  $\epsilon_{c,rnf}$ ,  $\epsilon_{t,rnf}$ ,  $\epsilon_{t,gl}$  and  $\epsilon_p$  are the result of only the actions.

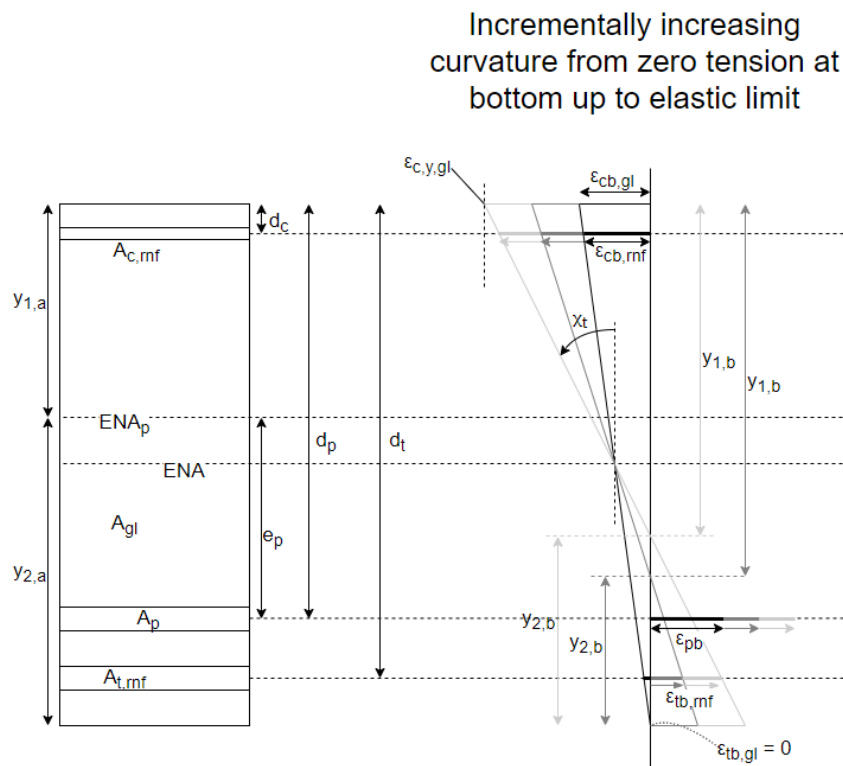


Figure 5.6: increasing action load up to reaching elastic limit strain for compression

Taking this into account, the action moment can be calculated for every increment up to the point where  $\epsilon_{cb,gl}$  reaches the elastic limit  $\epsilon_{c,y,gl}$ . This is where the prestress is able to

resist a higher action moment than with only reinforcement. With reinforcement only, the elastic limit strain is reached when  $\epsilon_{c,gl} = \epsilon_{c,y,gl}$ . With prestress, the elastic limit is reached when  $\epsilon_{cb,gl} = \epsilon_{c,y,gl}$ , where  $\epsilon_{cb,gl} = \epsilon_{tp} + \epsilon_{c,gl}$  with  $\epsilon_{tp} < 0$ . So it takes longer for a prestressed beam to reach the elastic limit. Taking this into account, the final elastic resistant moment is calculated as follows:

$$F_{c,gl} = \frac{1}{2}\epsilon_{c,y,gl} \cdot E_{gl} \cdot b_{gl} \cdot y_1$$

$$F_{c,rnf} = \epsilon_{c,rnf} \cdot E_{rnf} \cdot A_{c,rnf}$$

$$F_{t,gl} = \frac{1}{2}\epsilon_{t,gl} \cdot E_{gl} \cdot b_{gl} \cdot y_2$$

$$F_{t,rnf} = \epsilon_{t,rnf} \cdot E_{rnf} \cdot A_{t,rnf}$$

$$F_p = \epsilon_p \cdot E_p \cdot A_p$$

$$M_{p,el,lim} = F_p \cdot (y_2 - (h_{gl} - d_p)) + F_{t,rnf} \cdot (y_2 - (h_{gl} - d_t)) + F_{t,gl} \cdot \frac{2}{3}y_2 - F_{c,rnf} \cdot (y_1 - d_c) - F_{c,gl} \cdot \frac{2}{3}y_1$$

# 6. Initial behaviour results

## 6.1 Reinforced cross-section

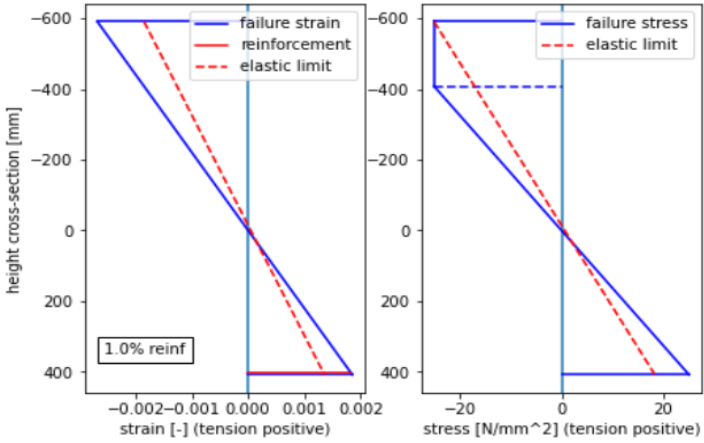
The model for a reinforced cross-section (Section 5.2) is used to quantify the behaviour of a reinforced cross-section. This is elaborated for a reinforced beam in this section.

### 6.1.1 Effect of tension reinforcement

Unstrengthened timber beams in bending generally have a brittle tensile failure. Introducing reinforcement in the tension region will prevent this. A typical failure of a tensile reinforced beam is shown in Figure 6.1a. It can be seen that the compression side of the beam has plastified to a great extent. Almost half of the beam height has reached its compression strength before the tension side reached its tensile strength. This experiment is a good example of greatly improved ductility for reinforced glulam. The numerical model is used to quantify this beam behaviour.



(a) Ductile beam failure [44]



(b) Strains and stresses of a reinforced section 1000x1000 mm

Figure 6.1: experimental- and model beam failure

Figure 6.1b displays a strain- and stress diagram resulting from the model. This cross-section is reinforced only at the tension side of the beam. It can be seen that the neutral axis is shifted from half the beam height towards the tension side of the beam. This causes the compression side to reach its yield strength ( $f_{c,y,gl}$ ) before the tension side reaches its yield strength

( $f_{t,y,gl}$ ). After this, the curvature is increased further, causing the compressive plastification zone ( $h_{pl}$ ) to increase. In order to keep equilibrium of forces, the model calculates a new plastic neutral axis. This can be seen by looking closely at the failure strain, which has a PNA slightly below the ENA. Curvature is increased until the timber fails in tension, this point is modelled as the ultimate failure of the beam.

Figure 6.2 presents this behaviour in terms of moment capacity. A linear moment-curvature relationship exists up to the elastic limit ( $M_{el,limit}$ ). After this point, plastification of the cross-section happens. Because of this, the cross-section shows ductile behaviour to a small extent, which is not found for the beam without reinforcement. The increase in slope of the graph means that the reinforced beam also has a significantly higher stiffness than the non-reinforced beam. This results in a smaller deflection of the beam, which will also be beneficial for the long-term behaviour of the beam (also see Chapter 8).

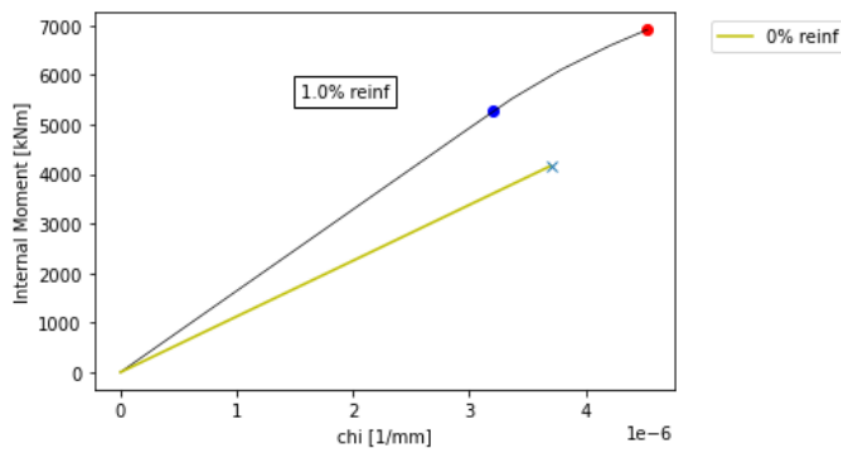


Figure 6.2: Moment-curvature graph of a cross-section 1000 x 1000 mm

### 6.1.2 Effect of reinforcement allocation

A reinforced beam always shows a larger stiffness than a non-reinforced beam. This enhancement is a result of the larger stiffness of the reinforcement material. However, more important is the allocation of the reinforcement. If the reinforcement is placed at a larger distance from the neutral axis, the stiffness increase will be larger. A beam with 100% of the reinforcement at the tension side shows high ductility. However, the effective stiffness of the beam does not increase as much as when the reinforcement would be allocated 50%/50%. Explanation for this is that the neutral axis of a beam shifts towards the reinforcement. So for a 100% tensile reinforced beam, the lever arm of the reinforcement is smaller. Leading to a smaller stiffness. Figure 6.3 presents this behaviour. The stiffness of the beam is at its largest when the reinforcement is allocated 50/50.

Figure 6.4 shows the moment-curvature graphs for varying reinforcement allocations. Also a reference curve is shown for the same cross-section without reinforcement. Compared to this cross-section, all reinforced cross-sections have significantly higher stiffness and moment capacity. The blue and red dots denote the elastic- and plastic moment resistances.

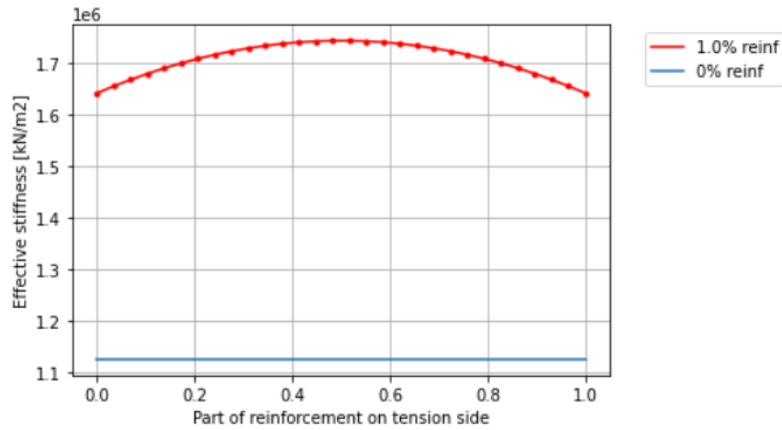


Figure 6.3: Beam flexural stiffness against reinforcement allocation for a beam 1000 x 1000 mm

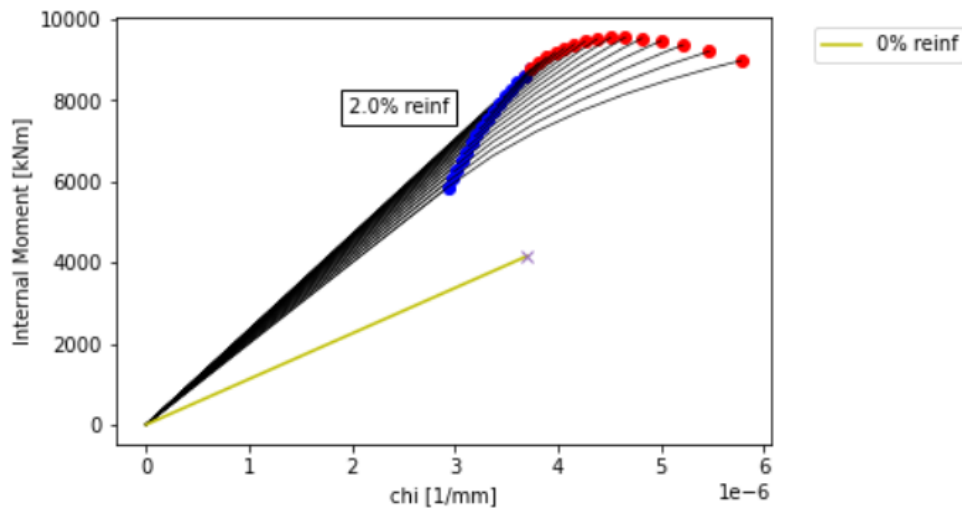


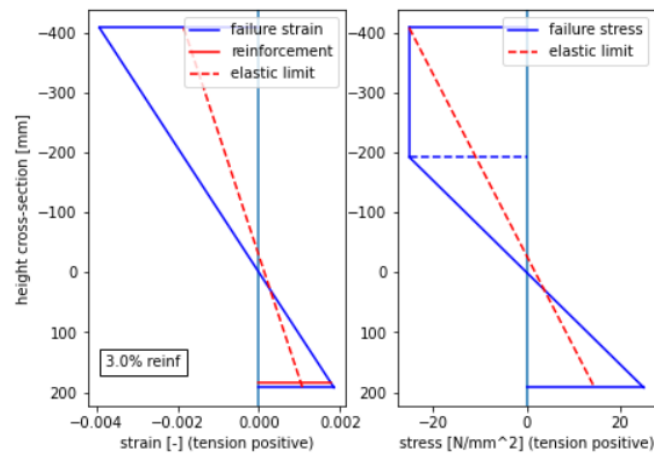
Figure 6.4: Moment-curvature diagrams for varying reinforcement allocations

**Lowest black line: 100% tensile reinforcement.** This configuration will give the highest ductility. After reaching the elastic limit, the cross-section has high deformation capacity. However, the elastic moment resistance is relatively small because the neutral axis is located towards the tensile side (see Figure 6.5a). The final result of this is that the compressive stresses reach the yield stresses relatively early. Also the effective stiffness is relatively small because of a smaller internal lever arm of the reinforcement

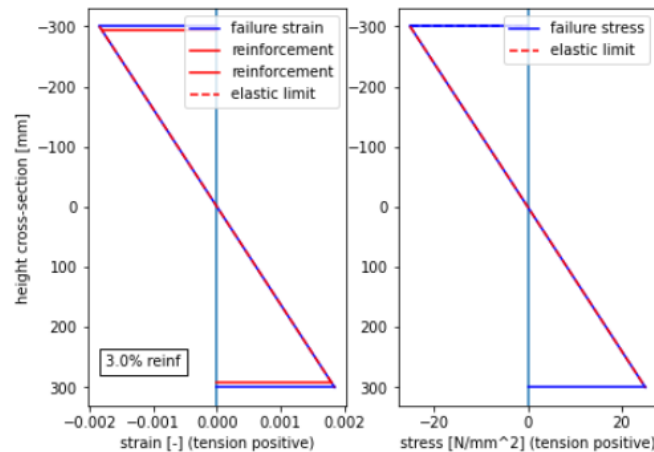
**Highest black line: 50%/50% reinforcement.** This configuration gives high stiffness, which will increase the SLS verification of the beam. However, no ductile behaviour is obtained because failure tensile stresses are reached at the same moment as yield compression stresses. This is a result of the evenly distributed reinforcement, see Figure 6.5b.

**50%/50% up to 100% compressive reinforcement.** After reaching the elastic moment limit, cross-sections with most of the reinforcement in the compression side will not show any

plastification. Therefore, no increase of ultimate moment will happen after the elastic limit. These cross-section fail in a brittle manner.



(a) 100% tensile reinforcement



(b) 50%/50% reinforcement

Figure 6.5: strain- and stress diagrams for different reinforcement allocation

This is explained further with Figure 6.6, where the ultimate moment is plotted against the reinforcement allocation. The ultimate resisting moment is smallest when all reinforcement is placed in the compression side. In this case, the timber will simply fail in tension without further plastification of the cross-section. The ultimate moment is largest when approximately 80% - 90% of the reinforcement is allocated at the tension side. In this case, the optimum balance is found between compressive plastification and lever arm of the reinforcing material. In case of all reinforcement on the tension side, maximum plastification is reached. However, the lever arm of the reinforcement gets smaller and therefore the produced resisting moment is smaller.

It can be seen that the stresses in the compression reinforcement  $\sigma_{c,rnf}$  go up when a higher reinforcement percentage is located in the tension side. This is caused by the increase of compressive strains  $\epsilon_{c,rnf}$  when the neutral axis moves towards the tension side. On the



other side, the stresses in the tension reinforcement  $\sigma_{t,rf}$  are about the same. This is because failure of the beam is modelled when the tensile stresses in the glulam  $\sigma_{t,gl}$  reach the glulam tensile strength  $f_{t,y,gl}$ .

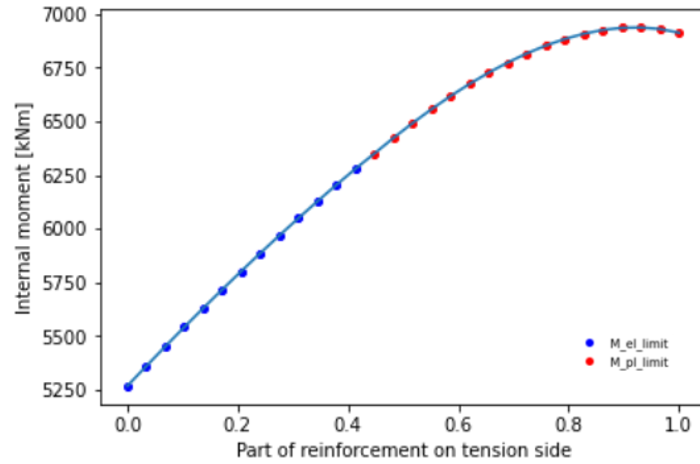


Figure 6.6: Ultimate moment capacity for varying reinforcement allocation

## 6.2 Prestressed cross-section

The model for a prestressed beam is comparable to the previous described model for a reinforced beam. The biggest difference is that the prestressing leads to an initial negative loading of the beam. This is displayed in Figure 6.7 below. Where: (A) constant compression strain  $\epsilon_{pn}$ . (B) linear strain  $\epsilon_{pm}$  due to eccentricity of the prestress load. (C) sum of (A) and (B): total strains due to prestressing  $\epsilon_p$ . Initial tension strain in the prestressed material shown in blue. (D) total stresses due to prestressing  $\sigma_p$ .

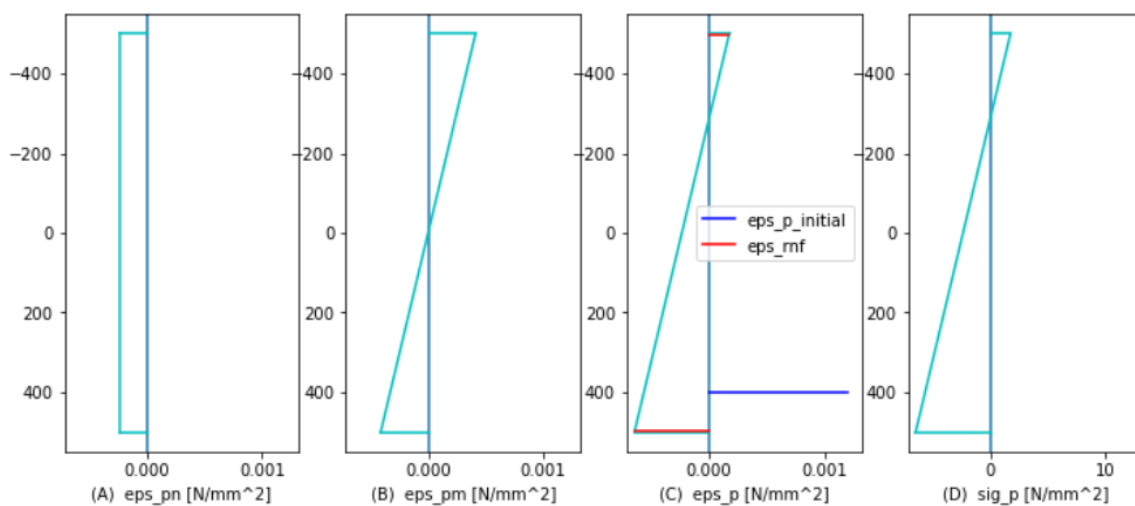


Figure 6.7: Initial loads due to prestressing

A comparison can be seen in Figure 6.8. Both graphs are based on a reinforcement allocation 50%/50% at top and bottom, and also prestress material is added. The right graph is based on zero prestress force, while the left graph is based on a prestress force of 3000 kN. As stated before, a reinforced beam with reinforcement allocation 50%/50% is stiff, but will more likely fail in a brittle manner. The same reinforced beam, with added prestress cables at the bottom side, will fail in compression because of two reasons: (1) the neutral axis shifts towards the lower side of the beam and (2) the compression from prestressing (see Figure 6.7 (A)) causes the compression failure to be reached earlier than the tension failure. This can also be seen in Figure 6.8. The right graph has already reached the limiting elastic strain at the compression side and almost at the tension side. At this loading moment, the prestressed beam almost reached its compression limit, while in tension the strain is much smaller than the limit strain. The prestressed section will be able to plastify to a much greater extend than the non-prestressed section because the curvature can be increased much more until the tension limit is reached.

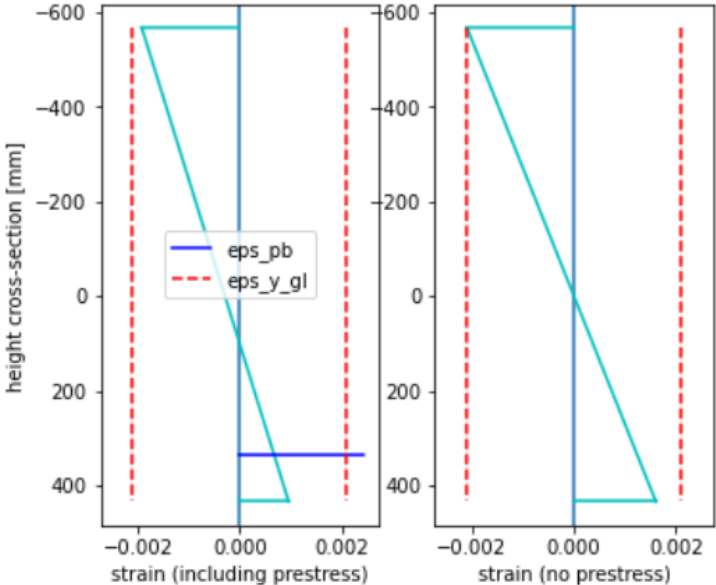


Figure 6.8: strain distribution for a prestressed (left) and only reinforced (right) cross-section

Moment-curvature graphs are presented in Figure 6.9 up to elastic limit. The pure timber deck, without reinforcement, has the lowest stiffness and moment capacity. The reinforced section, without prestress material, has a higher stiffness and moment capacity. For these results, the reinforcement is attached to the bottom and top of the timber deck. By adding prestress material to the already reinforced cross-section, the stiffness and moment capacity will increase further. The prestress cables are assumed to be allocated at  $0.1h_{gl}$  from the bottom of the beam. From Figure 6.9, all plots including prestress have the same stiffness. According to this, the stiffness does not increase with higher prestress forces. However, higher prestress forces will result in negative initial curvatures. Meaning that the prestress forces counteract the actions loads. This will help to reduce the final deflection.

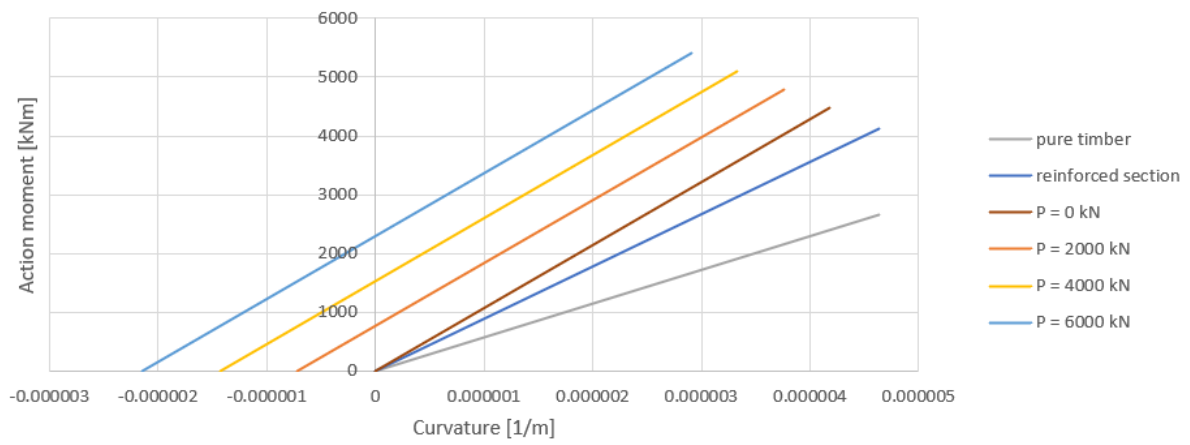


Figure 6.9: Moment-curvature graphs for timber, reinforced and prestressed sections

## 7. Long-term behaviour

The previous parts of the numerical model are only focused on the instantaneous loading of the cross-section. No creep is taken into account. However, creep deflections may play a decisive role in timber design. Creep of timber beams can lead to prestress losses that will decrease the cross-section resistance. In literature, the creep behaviour of timber is often modelled with a formula in the following form:

$$\phi = at^b \quad (7.1)$$

Where  $a$  and  $b$  are material parameters,  $\phi$  is the creep factor, and  $t$  is the time from the initial point of loading.

The benefit of this form is that it can be rewritten into a viscoelastic E-modulus dependent on time. Combining this time-dependent E-modulus with Ordinary Differential Equations (ODE's) enables the quantification of creep deflections over time at every longitudinal point of the bridge deck. In this research, this is done using Maple. This chapter explains how the long-term behaviour is quantified in the model.

### 7.1 Governing ODE's

A bridge deck can be analysed using Ordinary Differential Equations (ODE's). Using this approach, the cross-sectional forces, rotations and deformations can be quantified at every point of the deck. Because of the prestress forces at the beam ends, the timber deck is subjected to axial forces. Forces and deformations due to this effect can be quantified using the ODE for axial deformations. For a slender bridge deck, the deflections are governed by bending. The Euler-Bernoulli ODE system is used for this. Besides bending- and axial deformations, the deck is also subject to shear deformations. The combined effect of bending and shear deformation can be taken into account by using the Timoshenko ODE system. Calculations with the Timoshenko system are done and they show that the difference is about 1% with the Euler-Bernoulli system, these are presented in Appendix D. Because of these results, the shear deformations are neglected. Only the Euler-Bernoulli ODE system is used for the deflections.

### 7.1.1 Axial deformation

The prestress forces exerted on both ends of the bridge deck will cause a shortening. This effect can be covered by the ODE for axial deformation. As a result of an applied load, the deck will shorten. This can be formulated by the axial degree of freedom  $u(x)$ , see Figure 7.1a. The cross-section at longitudinal coordinate  $x$  will displace by  $u(x)$  and the displacement at  $x + dx$  will be  $u(x + dx) = u + du$ . The infinitesimal element  $dx$  undergoes a change in length equal to  $du$ . This deformation is given by the kinematic relation for axial strain:

$$\epsilon = \frac{du}{dx} \quad (7.2)$$

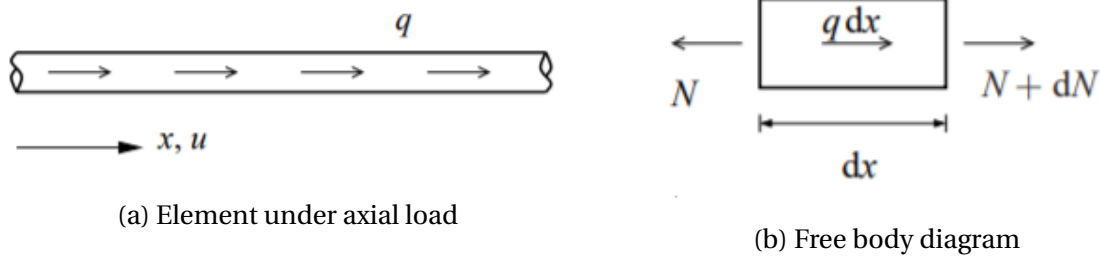


Figure 7.1

The deformations (strain  $\epsilon$ ) can be related to the stress by Hooke's law:

$$\sigma = E\epsilon \quad (7.3)$$

The stress distribution over the total cross-section gives the resulting internal force:

$$N = \int \sigma dA = \int E\epsilon dA = \frac{du}{dx} \int E dA \quad (7.4)$$

For homogeneous cross-sections, the constitutive relation for the normal force can be formulated:

$$N = EA\epsilon \quad (7.5)$$

Figure 7.1b gives the free body diagram of a small segment of the deck with internal forces. The total distributed load is replaced by its resultant  $q dx$ . For equilibrium in horizontal direction, following equilibrium equation is derived:

$$\frac{dN}{dx} = -q \quad (7.6)$$

Substituting the constitutive relations into the equilibrium equation gives the final ODE for axial deformations:

$$EA \frac{d^2 u}{dx^2} = -q \quad (7.7)$$

Where:

$EA$  = the axial stiffness of the beam

$q$  = the external load function exerted parallel to the beam

$u$  = the displacement in longitudinal direction depending on the coordinate  $x$

$x$  = the longitudinal coordinate going from the beginning to the end of the beam

This system can be solved for  $u(x)$  by applying the boundary conditions for the specified case.

### 7.1.2 Bending

For slender cases, beams loaded by vertical loads are governed by bending theory. Due to vertical action loads, bending deflection will occur which can be formulated by the vertical degree of freedom  $w(x)$ . Under the assumption of small displacements, the deflection can be related to the rotation according to Figure 7.2. This gives the first kinematic relation:

$$\phi = -\frac{dw}{dx} \quad (7.8)$$

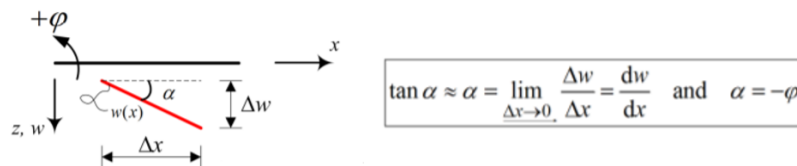


Figure 7.2: Deflection-rotation relation

Then, the curvature can be related to the rotation according to Figure 7.3. This gives the second kinematic relation:

$$\kappa = \frac{d\phi}{dx} \quad (7.9)$$

The constitutive relation for bending is formulated as follows:

$$M = EI\kappa \quad (7.10)$$

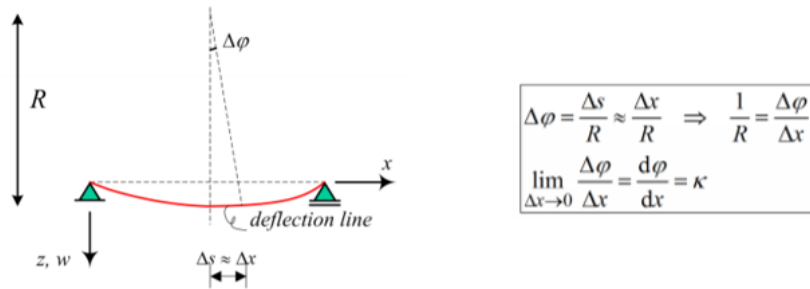


Figure 7.3: Rotation-curvature relation

Substituting Equation 7.8 into Equation 7.9 and substituting the result into Equation 7.10, following relation for the moment is obtained:

$$M = -EI \frac{d^2 w}{dx^2} \quad (7.11)$$

The equilibrium equations below can be derived from the free body diagram in Figure 7.4:

Vertical equilibrium:  $\frac{dV}{dx} = -q$

Moment equilibrium:  $\frac{dM}{dx} = V$

Combining both equilibrium equations gives:

$$\frac{d^2 M}{dx^2} = -q \quad (7.12)$$

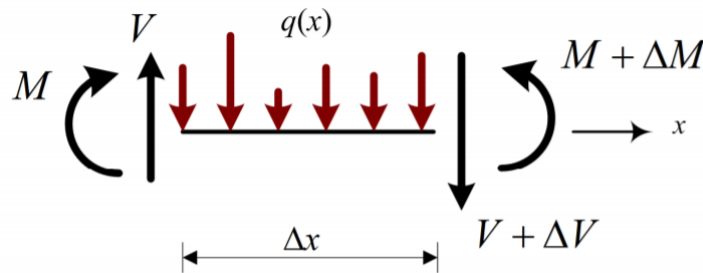


Figure 7.4: Free body diagram for bending ODE

Then the final step to obtain the ODE for bending is substituting Equation 7.11 into Equation 7.12. This gives following ODE that governs the bending deflections:

$$EI \frac{d^4 w}{dx^4} = q \quad (7.13)$$

Where:

$EI$  = the bending stiffness of the beam

$q$  = the external load function in vertical direction

$w$  = the deflection equation depending on the coordinate  $x$

$x$  = the longitudinal coordinate going from the beginning to the end of the beam

This system can be solved for  $w(x)$  by applying the boundary conditions for the specified case.

## 7.2 Deformation functions

To find the deformation functions for the bridge deck, multiple ODE's and boundary conditions must be taken into account, see Figure 7.5. The bridge deck is supported by two side supports and one middle support, therefore it is divided into two deformation fields: span 1 and span 2. Per field, two ODE's for bending are solved and one ODE for axial deformation is solved.

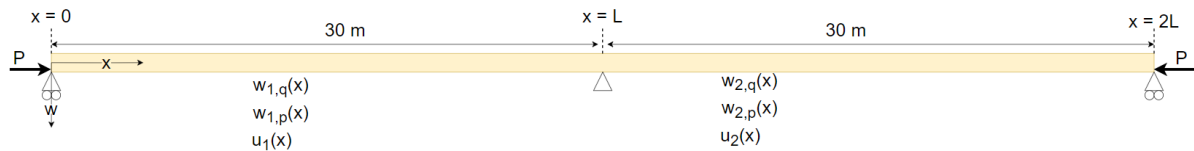


Figure 7.5: Bridge system as input for the ODE's

### 7.2.1 Axial shortening

As stated before, the ODE for axial deformation (Equation 7.14) can be used to model the effect of the prestress forces on the beam ends. In this case, the  $q$ -load in longitudinal direction is zero and the axial ODE becomes:

$$EA \frac{d^2 u_i}{dx^2} = 0 \quad (7.14)$$

Where  $i = 1, 2$

Span 1 is governed by  $u_1(x)$  and span 2 is governed by  $u_2(x)$ . Following boundary conditions apply:

$$\begin{aligned} \text{at } x = 0: & \quad P + N_1 = 0 \\ \text{at } x = L: & \quad u_1 = u_2 = 0 \\ \text{at } x = 2L: & \quad -N_2 - P = 0 \end{aligned}$$

The ODE is solved with use of the software Maple. Using the previous boundary conditions,



following deformation functions for the axial displacement fields are obtained:

$$u_1(x) = -\frac{Px}{EA} + \frac{LP}{EA} \quad (7.15)$$

$$u_2(x) = -\frac{Px}{EA} + \frac{LP}{EA} \quad (7.16)$$

## 7.2.2 Bending deflection

The bending ODE from Equation 7.13 governs the bending deflections due to the action loads and the prestress loads. Both cases are solved separately with an own ODE for bending. The corresponding functions  $w_1$  and  $w_2$  can be determined by solving the ODE's for the boundary conditions:

### ODE for action loads

The bending ODE from Equation 7.13 is used for deflection due to the action loads. In this case, the load  $q_{i,q}$  is the load per field due to the actions on the deck. The ODE for actions loads becomes:

$$EI \frac{d^4 w_{i,q}}{dx^4} = q_{i,q} \quad (7.17)$$

Where  $i = 1, 2$

Span 1 is governed by  $w_{1,q}(x)$  and span 2 is governed by  $w_{2,q}(x)$ . Following boundary conditions apply:

$$\begin{aligned} \text{at } x = 0: & \quad w_{1,q} = 0 \\ \text{at } x = 0: & \quad M_{1,q} = 0 \\ \text{at } x = L: & \quad w_{1,q} = w_{2,q} = 0 \\ \text{at } x = L: & \quad \phi_{1,q} = \phi_{2,q} \\ \text{at } x = L: & \quad M_{1,q} = M_{2,q} \\ \text{at } x = 2L: & \quad w_{2,q} = 0 \\ \text{at } x = 2L: & \quad M_{2,q} = 0 \end{aligned}$$

This gives following deformation functions due to the loads:

$$w_{1,q}(x) = \frac{q_{1,q}x^4}{24EI} - \frac{L(7q_{1,q} - q_{2,q})x^3}{96EI} + \frac{L^3(3q_{1,q} - q_{2,q})x}{96EI} \quad (7.18)$$

$$\begin{aligned} w_{2,q}(x) = & \frac{q_{2,q}x^4}{24EI} - \frac{L(q_{1,q} + 25q_{2,q})x^3}{96EI} + \frac{L^2(q_{1,q} + 9q_{2,q})x^2}{16EI} \\ & - \frac{L^3(11q_{1,q} + 47q_{2,q})x}{96EI} + \frac{L^4(3q_{1,q} + 7q_{2,q})}{48EI} \end{aligned} \quad (7.19)$$

### ODE for prestress loads

The prestress force will cause shortening of the bridge deck (covered with the ODE in Equation 7.14). Besides shortening, prestress will also induce bending moments on the deck. The bending ODE from Equation 7.13 can also be used to determine the deflections due to the prestress loads. Two cases are analyzed: a straight tendon and a parabolic tendon. A straight tendon is easier to analyze. A straight tendon will have a constant moment resistance over the length of the beam because the height of the tendon does not change. The height of the tendon will change for a parabolic tendon and therefore also the moment resistance will vary over the length of the beam.  $q_p$  is the load exerted by the prestress tendons. Following ODE for bending due to prestress is obtained:

$$EI \frac{d^4 w_{i,p}}{dx^4} = q_p \quad (7.20)$$

Where:

$i = 1, 2$  for span 1 or 2.

$q_p = P \cdot \frac{d^2 z_i}{dx^2}$  [1], depends on the prestress force  $P$  and the tendon profile  $z_i$ .

$$^{[1]} q_p = \frac{P}{R} \text{ [24]}, \quad \text{where } \frac{1}{R} = \kappa = \frac{d^2 z}{dx^2}$$

### Straight tendon

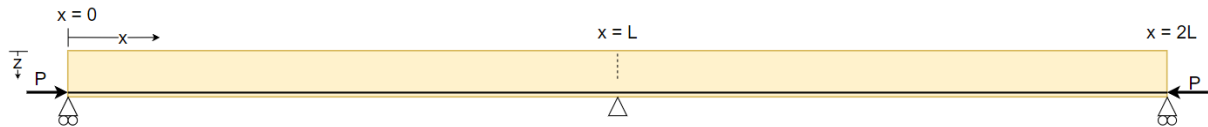


Figure 7.6: Layout straight tendon

For a straight tendon, the load  $q_p = 0$ . Following boundary conditions apply:

$$\begin{aligned} \text{at } x = 0: & \quad w_{1,p} = 0 \\ \text{at } x = 0: & \quad M_{1,p} = M_p \\ \text{at } x = L: & \quad w_{1,p} = w_{2,p} = 0 \\ \text{at } x = L: & \quad \phi_{1,p} = \phi_{2,p} \\ \text{at } x = L: & \quad M_{1,p} = M_{2,p} \\ \text{at } x = 2L: & \quad w_{2,p} = 0 \\ \text{at } x = 2L: & \quad M_{2,p} = M_p \end{aligned}$$

Where  $M_p = -P \cdot e_{end}$ , and  $e_{end}$  is the eccentricity of the tendon at the beam ends.

Following deformation functions due to prestressed straight tendons are obtained:

$$w_{1,p}(x) = -\frac{e_{end} P x^3}{4EI} + \frac{e_{end} P x^2}{2EI} - \frac{L e_{end} P x}{4EI} \quad (7.21)$$

$$w_{2,p}(x) = \frac{e_{end}Px^3}{4EIL} - \frac{e_{end}Px^2}{EI} + \frac{5Le_{end}Px}{4EI} - \frac{e_{end}PL^2}{2EI} \quad (7.22)$$

### Parabolic tendon

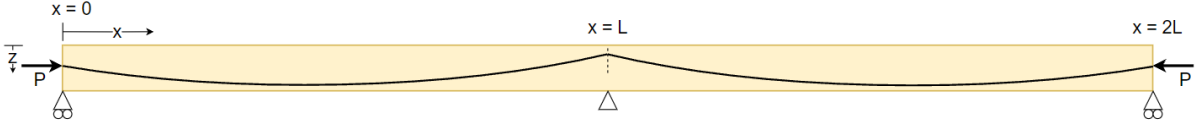


Figure 7.7: Layout parabolic tendon

For a parabolic tendon, the load  $q_p = P \cdot \frac{d^2 z_i}{dx^2}$ . Following boundary conditions apply:

$$\begin{aligned} \text{at } x = 0: & \quad w_{1,p} = 0 \\ \text{at } x = 0: & \quad M_{1,p} = M_p \\ \text{at } x = L: & \quad w_{1,p} = w_{2,p} = 0 \\ \text{at } x = L: & \quad \phi_{1,p} = \phi_{2,p} \\ \text{at } x = L: & \quad M_{1,p} = M_{2,p} \\ \text{at } x = 2L: & \quad w_{2,p} = 0 \\ \text{at } x = 2L: & \quad M_{2,p} = M_p \end{aligned}$$

Where  $M_p = P \cdot e_{end}$ , and  $e_{end}$  is the eccentricity of the tendon at the beam ends.

Following deformation functions due to prestressed parabolic tendons are obtained:

$$w_{1,p}(x) = \frac{q_p x^4}{24EI} - \frac{(q_p L^2 - 4e_{end}P)x^3}{16EIL} - \frac{e_{end}Px^2}{2EI} + \frac{L(q_p L^2 + 12e_{end}P)x}{48EI} \quad (7.23)$$

$$w_{2,p}(x) = \frac{q_p x^4}{24EI} - \frac{(13q_p L^2 + 12e_{end}P)x^3}{48EIL} + \frac{(5q_p L^2 + 8e_{end}P)x^2}{8EI} - \frac{L(29q_p L^2 + 60e_{end}P)x}{48EI} + \frac{L^2(5q_p L^2 + 12e_{end}P)}{24EI} \quad (7.24)$$

### Total deflection

The total bending deflections can be determined by the sum of the deflections due to the loads  $w_{i,q}$  and the prestress  $w_{i,p}$ . It should be noted that the deflection due to the prestress is negative and that of the action loads is positive. Then, following equations apply for the total bending deflections:

$$w_{1,b}(x) = w_{1,q}(x) + w_{1,p}(x) \quad (7.25)$$

$$w_{2,b}(x) = w_{2,q}(x) + w_{2,p}(x) \quad (7.26)$$

### 7.2.3 Instantaneous displacements

Up to now, the axial shortening and bending deflections represent the instantaneous displacements of the bridge deck. This means that using the equations for  $u_1(x)$ ,  $u_2(x)$ ,  $w_{1,b}(x)$  and  $w_{2,b}(x)$  will only give the instantaneous displacements because they are based on the initial E-modulus of the timber deck. In Section 7.4 is explained how the time-dependence is incorporated in the equations through a viscoelastic E-modulus.

## 7.3 Strains

The strains over the cross-section of the timber deck can be determined using the ODE relations. This is done for the axial shortening and the bending deflections. Later on, the viscoelastic E-modulus is substituted into these strain functions to obtain the time-dependent strains.

### 7.3.1 Axial strains

From Equation 7.2, it holds that the strains are equal to the derivative of the displacement fields, this gives the strain functions below. It can be seen that the strains due to the compressive prestress forces are constant over the length of the deck. Also they are not dependent on the height coordinate  $z$ . The axial strains are constant at every point and are not dependent on the longitudinal and vertical coordinates  $x$  and  $z$ .

$$\epsilon_{1,n} = \frac{du_1}{dx} = -\frac{P}{EA} \quad (7.27)$$

$$\epsilon_{2,n} = \frac{du_2}{dx} = -\frac{P}{EA} \quad (7.28)$$

### 7.3.2 Bending strains

In contradiction to the axial strains, the bending strains are dependent on both coordinates  $x$  and  $z$ . The bending strains can be derived from the total bending deflections in Equations 7.25 and 7.26. Following relation is used to determine the bending strains:

$$\epsilon_{i,b} = \kappa_{i,b} \cdot z_i = -\frac{d^2 w_{i,b}}{dx^2} \cdot z_i \quad (7.29)$$

Where  $i = 1, 2$

Using Equation 7.29, the strains due to bending for fields 1 and 2 become:

### ***Straight tendon***

$$\epsilon_{1,b}(x) = \left( \frac{3e_{end}Px}{2EIL} - \frac{e_{end}P}{EI} - \frac{q_{1,q}x^2}{2EI} + \frac{L(7q_{1,q} - q_{2,q})x}{16EI} \right) z_1 \quad (7.30)$$

$$\epsilon_{2,b}(x) = \left( -\frac{3e_{end}Px}{2EIL} + \frac{2e_{end}P}{EI} - \frac{q_{2,q}x^2}{2EI} + \frac{L(q_{1,q} + 25q_{2,q})x}{16EI} - \frac{L^2(q_{1,q} + 9q_{2,q})}{8EI} \right) z_2 \quad (7.31)$$

### ***Parabolic tendon***

$$\epsilon_{1,b}(x) = \left( -\frac{q_p x^2}{2EI} + \frac{3(q_p L^2 - 4e_{end}P)x}{8EIL} + \frac{e_{end}P}{EI} - \frac{q_{1,q}x^2}{2EI} + \frac{L(7q_{1,q} - q_{2,q})x}{16EI} \right) z_1 \quad (7.32)$$

$$\epsilon_{2,b}(x) = \left( -\frac{q_p x^2}{2EI} + \frac{13(q_p L^2 + 12e_{end}P)x}{8EIL} - \frac{5q_p L^2 + 8e_{end}P}{4EI} - \frac{q_{2,q}x^2}{2EI} + \frac{L(q_{1,q} + 25q_{2,q})x}{16EI} - \frac{L^2(q_{1,q} + 9q_{2,q})}{8EI} \right) z_2 \quad (7.33)$$

### **7.3.3 $z_1$ and $z_2$ for tendon layouts**

To find the losses in the prestress material, the strains in the prestress material must be calculated. Therefore,  $z_1$  and  $z_2$  in Equations 7.30 to 7.33 are based on the prestress tendon profile.

For straight tendons, the values for  $z_1$  and  $z_2$  are constant over the length of the deck.

For parabolic tendons, the values for  $z_1$  and  $z_2$  are dependent on the longitudinal coordinate  $x$ . The layout for a parabolic tendon profile is presented in Figure 7.8. If reinforced is present, it is attached to the top and bottom of the deck. At the beam ends, the prestress tendons are attached at half of the beam height so that no negative prestress moment is exerted at that location. The tendons are allocated  $0.1h_{gl}$  from the bottom at their lowest position. This is assumed to prevent the timber below the cable to be too thin. The same is applied to the cable at the highest position at  $x = L$ .

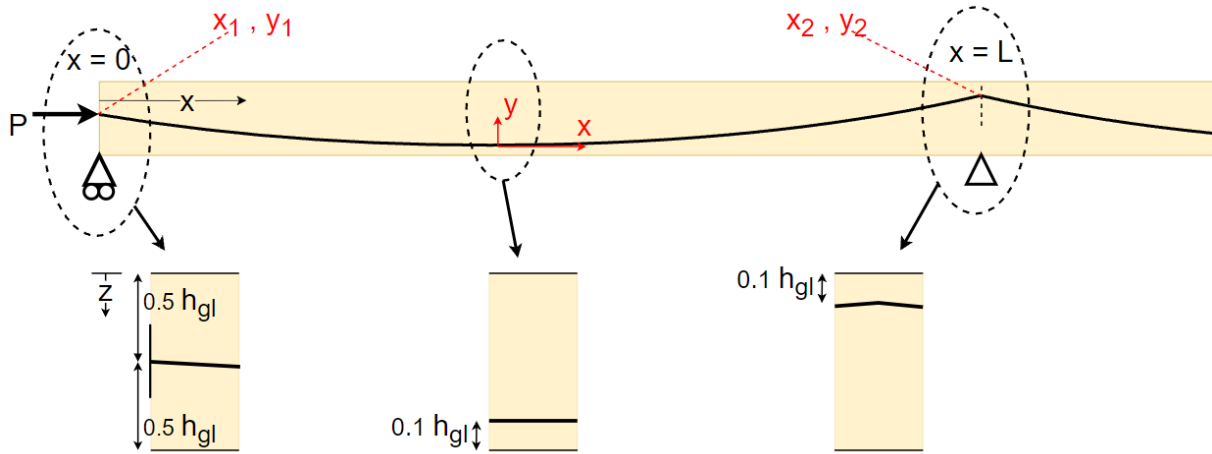


Figure 7.8: Deck configuration

The tendon location  $z_1$  can be written as a function of the  $x$ -coordinate. First a local coordinate system is applied to the lowest point of the tendons, presented with red in Figure 7.8. The tendon is of the form  $y = ax^2$ .

**At the left beam end:**

$$y_1 = ax_1^2 \quad (7.34a)$$

$$e_{end} = ax_1^2 \quad (7.34b)$$

$$a = \frac{e_{end}}{x_1^2} \quad (7.34c)$$

Where  $e_{end}$  is equal to  $0.5h_{gl} - 0.1h_{gl} = 0.4h_{gl}$

**At the middle support:**

$$y_2 = ax_2^2 \quad (7.35a)$$

Where  $x_2 = L + x_1$  and  $y_2 = e_{end} + e_{midspan} = e_{end} + 0.5h_{gl} - 0.1h_{gl}$

$$e_{end} + e_{midspan} = a(L + x_1)^2 \quad (7.35b)$$

Equation 7.34c and 7.35b can be solved for  $a$  and  $x_1$ . With this, a parabolic equation for the vertical tendon location  $z_1$  is found. In the same way, a parabolic equation for the tendons at span 2 is found for  $z_2$ .  $z_1$  and  $z_2$  are substituted in the deformation and strains equations from Section 7.3.2. Now, the creep deformations and creep strains of the prestress tendons can be calculated.

## 7.4 Time-dependent E-modulus

The bridge deck will be subject to time-dependent deformations due to creep phenomena. This section explains how the time-dependence is incorporated in the Maple model.

### 7.4.1 Findley's power law

Findley's power law [12] is used to be able to model the creep deformations of the bridge deck. This law assumes a viscoelastic E-modulus that decreases over time according to Equation 7.36. Because of this decreasing E-modulus, the deformation will increase over time.  $E_v(t)$  can be substituted into the deformation functions and strain functions from previous section to obtain time-dependent deformation functions.

$$E_v(t) = \frac{E_0 E_t}{E_t + E_0 t^n} \quad (7.36)$$

Where:

$E_0$  = the initial elastic modulus of the material, independent of time

$E_t = \frac{\sigma_0}{m}$  = a modulus which characterizes the time-dependent behaviour

$n$  = material constant

$\sigma_0 = E_0 \epsilon_0$  = the stress due to instantaneous loading for the creep load model

$m$  = stress-dependent coefficient

$t$  = time after loading

The material constants  $m$  and  $n$  govern Equation 7.36. They depend on the long-term material behaviour. They can be determined from creep strain curves. The creep strain function is given by Equation 7.37. In this research, the values for  $m$  and  $n$  are determined based on experiments from literature.

$$\epsilon(t) = \epsilon_0 + m \cdot t^n \quad (7.37)$$

Where:

$\epsilon(t)$  = total time-dependent strain

$\epsilon_0$  = stress-dependent initial elastic strain

### 7.4.2 Material parameters m and n

Literature studies are used to quantify the material parameters  $m$  and  $n$  from Equation 7.37. Then, rewriting this into Equation 7.36 will give the viscoelastic E-modulus that is dependent on time:  $E_v(t)$ . This modulus can be substituted for  $E$  in the ODE's so that they become dependent on time.

## O’Ceallaigh’s experiments

O’Ceallaigh et al [38] [39] did experiments to glulam beams reinforced with Basalt FRP in a Relative Humidity of 65% - 90%. According to Eurocode 5, this corresponds to CC3. All experimental conditions can be found in Table 7.1. They measured the total strains over a time period of 525 days, which corresponds to 12600 hours. This is done using strain gauges at the tension- and compression faces of the glulam beams. For this research, the red curve is fitted to these creep strains, see Figure 7.9. The blue and grey curves are the observed creep strains for the bottom- and top side of the beam. To be safe, the curve is fitted slightly above the largest creep strains. The formula for this curve is given in Equation 7.38.

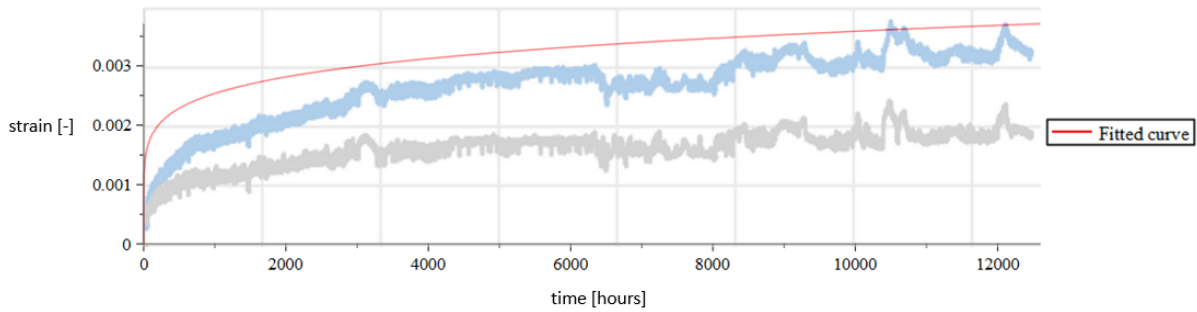


Figure 7.9: Creep strain curve fitted to the experimental results of O’Ceallaigh

$$\epsilon(t) = 0.00009 \cdot t^{0.13} \quad (7.38)$$

This is the creep curve for the strains applicable to the experiments of O’Ceallaigh et al. To make it generally applicable, the factor 0.00009 should be divided by the instantaneous strain from O’Ceallaighs experiment ( $\epsilon_{inst,oc} = 0.00064$ ):

$$\epsilon_{oc}(t) = \epsilon_0 + \epsilon_0 \frac{0.00009}{\epsilon_{inst,oc}} \cdot t^{0.13} = \epsilon_0 + \overbrace{\epsilon_0 \cdot 0.14}^m t^{\overbrace{0.13}^n} \quad (7.39)$$

Duration	525 days
Climate	Relative Humidity 65% to 90% (CC3)
Temperature	Constant at 20 +- 2°C
Cross-section	98 x 125 mm
Span	2300 mm
Reinforcement	Basalt FRP at tension side (non-prestressed)
Loading configuration	Four point bending

Table 7.1: Experimental program O’Ceallaigh [38] [39]



## Willebrands' literature studie

Willebrands [36] did a literature study to attain a quantitative approximation of creep behaviour of timber elements. Several curves were fitted on experiments of Gowda et al [37] and Abdul-Wahab et al [45]. The experiment of Gowda is the most representative for the case of the timber deck. Both sawn and glulam spruce beams where tested in a Relative Humidity of 60% to over 85% for more than a few weeks per year, which is between CC2 and CC3. All experimental conditions can be found in Table 7.2. In contradiction to the strain curve of O'Ceallaigh, Gowda presents its results in terms of a creep factor  $\phi(t)$ . Willebrands fitted the curve in Figure 7.10 and Equation 7.40 to these experiments.

$$\phi(t) = 0.125 \ln(0.2t + 1) \quad (7.40)$$

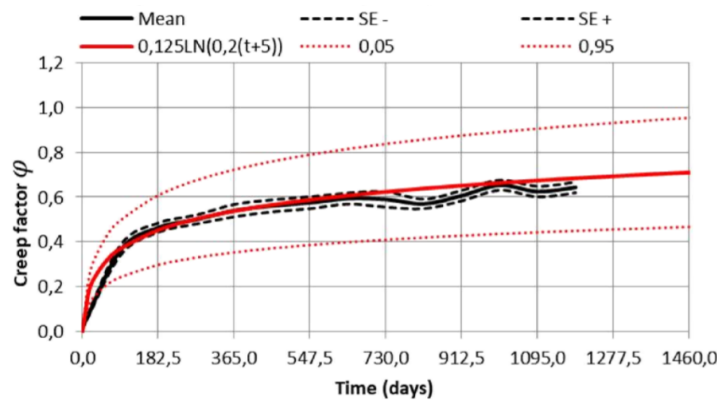


Figure 7.10: Willebrands' fit to Gowda's experiments

The curve of Willebrands in Equation 7.40 cannot be rewritten into the viscoelastic modulus because it is not of the form  $a \cdot t^b$ . Therefore, Willebrands equation is approximated with a function of this form. Which gives following creep function:

$$\phi_{wi}(t) = 0.34 \cdot t^{0.11} \quad (7.41)$$

To make this creep function applicable for Findley's model, it should be rewritten into a strain function. This can be done easily by multiplying the creep function with the instantaneous strain. Doing this, the creep strains in the form of Findley's law for Willebrands creep function can then be written as:

$$\epsilon_{wi}(t) = \epsilon_0(1 + \phi_{wi}(t)) = \epsilon_0 + \overbrace{\epsilon_0 \cdot 0.34}^m t^{\overbrace{0.11}^n} \quad (7.42)$$

Duration	4 years
Climate	CC2-CC3
Temperature	-5 to 20°C
Cross-section	(1): 50 x 150 mm, (2): 90 x 180 mm
Span	(1): 5000 mm, (2): 6500 mm
Reinforcement	No reinforcement
Loading configuration	Four point bending

Table 7.2: Experimental program Gowda [37]

### Creep curves

Both creep curves are displayed in Figure 7.11 up to  $t = 43800$  hours, which is equal to 50 years. The model is not executed for time spans bigger than 50 years because those time spans take too much calculation time. The increase of the creep curves is only 7% from 50 to 100 years. To check the effect of increased creep curves, also a sensitivity analysis is done with increased creep curves (Section 8.1.2). The creep curves can be rewritten into the creep strain equations in Equations 7.39 and 7.42. Then they can be implemented in the Findley model. From Figure 7.11 can be seen that curves from O’Ceallaigh and Willebrands differ by a factor of approximately 2. Multiple reasons could be of influence on these different creep curves. First, the fact that the tests of O’Ceallaigh were on reinforced beams while the tests of Gowda were on unreinforced beams. The Difference in experimental conditions might also have an influence. Besides, the experiments were carried out over a time span of 1.5 and 4 years for O’Ceallaigh and Gowda respectively. After these time spans the results were extrapolated, as shown in Figure 7.11. All these factors have an influence on the final creep curves of Figure 7.11, meaning that they are subject to uncertainty. Therefore, also a sensitivity analysis is made to check how this influences the final creep behaviour of the bridge deck. This is done in Section 8.1.2.

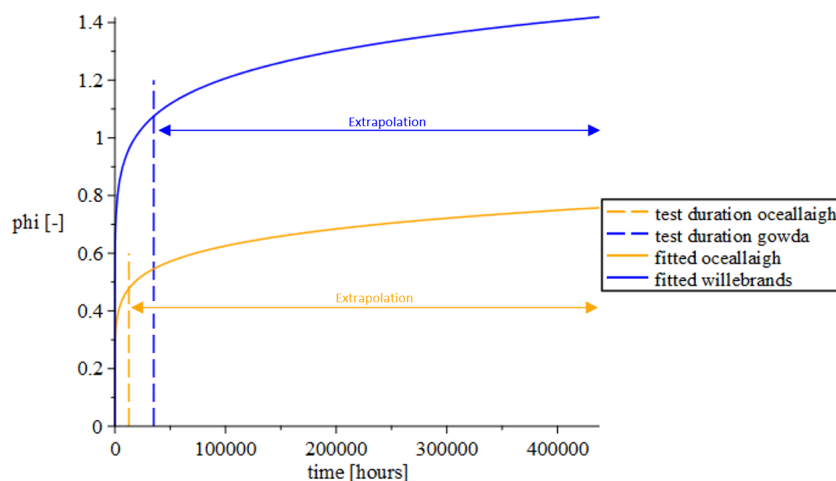


Figure 7.11: Creep curves

### 7.4.3 Equation for $E_v(t)$

In Section 7.4.2, the creep behaviour of O'Ceallaigh and Willebrands researches are written in the form of Findley's creep strain function:

$$\epsilon_{oc}(t) = \epsilon_0 + \overbrace{\epsilon_0 \cdot 0.14}^{m_{oc}} t^{\overbrace{0.13}^{n_{oc}}} \quad (7.43)$$

$$\epsilon_{wi}(t) = \epsilon_0 + \overbrace{\epsilon_0 \cdot 0.34}^{m_{wi}} t^{\overbrace{0.11}^{n_{wi}}} \quad (7.44)$$

In these creep strain functions, the material parameter  $m$  is dependent on the instantaneous strain  $\epsilon_0$ . If the  $m$  and  $n$  values are substituted into Equation 7.36 for the viscoelastic strains, following viscoelastic E-modulus is obtained:

$$E_t = \frac{E_0 \epsilon_0}{m} \quad (7.45)$$

If the factors  $m_{oc}$  or  $m_{wi}$  are substituted in this formula, the instantaneous strain  $\epsilon_0$  disappears from the formula for  $E_t$ . Filling in  $m_{oc}$ ,  $n_{oc}$  and  $m_{wi}$ ,  $n_{wi}$  gives following equations for the viscoelastic E-moduli according to Findley:

$$E_{v,oc}(t) = \frac{7.143 E_0^2}{7.143 E_0 + E_0 t^{0.13}} \quad (7.46)$$

$$E_{v,wi}(t) = \frac{2.941 E_0^2}{2.941 E_0 + E_0 t^{0.11}} \quad (7.47)$$

$E_{v,wi}(t)$  will be used to model the time-dependent strains due to the axial loads of the prestress force.  $E_{v,wi}(t)$  can be substituted into the axial strain Equations 7.27 and 7.28 to obtain the strains as a function of time, this is presented in Equation 7.48 The axial deformation of the prestressed timber deck can be schematized as a pure timber deck (no prestress cables) with external compressive forces on the beam ends. Therefore, the viscoelastic E-modules based on Willebrands (Equation 7.47) is used, which is also based on creep behaviour of non-reinforced and non-prestressed timber beams.

$$\epsilon_{1,n}(t) = -\frac{P}{E_{v,wi}(t)A} \quad (7.48a)$$

$$\epsilon_{2,n}(t) = -\frac{P}{E_{v,wi}(t)A} \quad (7.48b)$$

$E_{v,oc}(t)$  will be substituted in the bending strain Equations 7.49 and 7.49b for a straight tendon and Equations 7.32 and 7.33 for a parabolic tendon, this is presented in Equation 7.49

and 7.50. Unlike the behaviour in axial compression, in bending the prestress cables will also take part in resisting the exerted bending moment. The creep strains in bending are modelled with  $E_{v,oc}(t)$  because the research of O'Ceallaigh is based on reinforced timber members. In the case that it would be prestressed, the final strains would be lower because of the counteracting prestress moment. Meaning that it is conservative to use the strain measurements from O'Ceallaigh for bending.

### Straight tendon

$$\epsilon_{1,b}(x) = \left( \frac{3e_{end}Px}{2E_{v,oc}(t)IL} - \frac{e_{end}P}{E_{v,oc}(t)I} - \frac{q_{1,q}x^2}{2E_{v,oc}(t)I} + \frac{L(7q_{1,q} - q_{2,q})x}{16E_{v,oc}(t)I} \right) z_1 \quad (7.49a)$$

$$\epsilon_{2,b}(x) = \left( -\frac{3e_{end}Px}{2E_{v,oc}(t)IL} + \frac{2e_{end}P}{E_{v,oc}(t)I} - \frac{q_{2,q}x^2}{2E_{v,oc}(t)I} + \frac{L(q_{1,q} + 25q_{2,q})x}{16E_{v,oc}(t)I} - \frac{L^2(q_{1,q} + 9q_{2,q})}{8E_{v,oc}(t)I} \right) z_2 \quad (7.49b)$$

### Parabolic tendon

$$\epsilon_{1,b}(x, t) = \left( -\frac{q_p x^2}{2E_{v,oc}(t)I} + \frac{3(q_p L^2 - 4e_{end}P)x}{8E_{v,oc}(t)IL} + \frac{e_{end}P}{E_{v,oc}(t)I} - \frac{q_{1,q}x^2}{2E_{v,oc}(t)I} + \frac{L(7q_{1,q} - q_{2,q})x}{16E_{v,oc}(t)I} \right) z_1 \quad (7.50a)$$

$$\epsilon_{2,b}(x, t) = \left( -\frac{q_p x^2}{2E_{v,oc}(t)I} + \frac{13(q_p L^2 + 12e_{end}P)x}{8E_{v,oc}(t)IL} - \frac{5q_p L^2 + 8e_{end}P}{4E_{v,oc}(t)I} - \frac{q_{2,q}x^2}{2E_{v,oc}(t)I} + \frac{L(q_{1,q} + 25q_{2,q})x}{16E_{v,oc}(t)I} - \frac{L^2(q_{1,q} + 9q_{2,q})}{8E_{v,oc}(t)I} \right) z_2 \quad (7.50b)$$

$E_{v,oc}(t)$  will also be substituted in the deflection Equations 7.25 and 7.26. For the parabolic tendons, this gives Equations 7.51a and 7.51b. These equations will be used to model the creep deflections of the bridge deck.

$$w_{1,b}(x, t) = \frac{q_{1,q}x^4}{24E_{v,oc}(t)I} - \frac{L(7q_{1,q} - q_{2,q})x^3}{96E_{v,oc}(t)I} + \frac{L^3(3q_{1,q} - q_{2,q})x}{96E_{v,oc}(t)I} + \frac{q_p x^4}{24E_{v,oc}(t)I} - \frac{(q_p L^2 - 4e_{end}P)x^3}{16E_{v,oc}(t)IL} - \frac{e_{end}Px^2}{2E_{v,oc}(t)I} + \frac{L(q_p L^2 + 12e_{end}P)x}{48E_{v,oc}(t)I} \quad (7.51a)$$

$$\begin{aligned}
w_{2,b}(x, t) = & \frac{q_{2,q}x^4}{24E_{v,oc}(t)I} - \frac{L(q_{1,q} + 25q_{2,q})x^3}{96E_{v,oc}(t)I} + \frac{L^2(q_{1,q} + 9q_{2,q})x^2}{16E_{v,oc}(t)I} - \frac{L^3(11q_{1,q} + 47q_{2,q})x}{96E_{v,oc}(t)I} \\
& + \frac{L^4(3q_{1,q} + 7q_{2,q})}{48E_{v,oc}(t)I} + \frac{q_p x^4}{24E_{v,oc}(t)I} - \frac{(13q_p L^2 + 12e_{end}P)x^3}{48E_{v,oc}(t)IL} + \frac{(5q_p L^2 + 8e_{end}P)x^2}{8E_{v,oc}(t)I} \\
& - \frac{L(29q_p L^2 + 60e_{end}P)x}{48E_{v,oc}(t)I} + \frac{L^2(5q_p L^2 + 12e_{end}P)}{24E_{v,oc}(t)I}
\end{aligned} \tag{7.51b}$$

#### 7.4.4 Viscoelastic stiffnesses $E_v I$ and $E_v A$

For a non-reinforced prestressed beam, the stiffness of the timber is used. In this case, the stiffnesses can simply be calculated as  $E_v(t)I$  and  $E_v(t)A$ . However, for a prestressed beam that is also reinforced on the upper and lower sides, the stiffnesses should be recalculated for every timestep. This is done using the transformed section method [46]. First, the section is transformed into a section with one reference material.

$$\alpha = E_{rnf}/E_v(t) \tag{7.52}$$

$$A_{t,rnf,trans} = \alpha A_{t,rnf} \tag{7.53a}$$

$$A_{c,rnf,trans} = \alpha A_{c,rnf} \tag{7.53b}$$

The Elastic Neutral Axis (ENA) should be calculated according to:

$$y = \frac{\sum A_{i,trans} y_i}{\sum A_{i,trans}} \tag{7.54}$$

Where  $A_{i,trans}$  is the transformed surface of every material,  $y_i$  is the distance between the centroid of every material and the top of the total section, and  $y$  is the distance of the top of the section and the neutral axis of the total section. Then, the bending- and axial stiffnesses can be calculated according to:

$$E_{v,oc}(t)I = \sum E_v(t) \left( \frac{1}{12} b_{i,trans} h_i^3 + A_i y_i^2 \right) \tag{7.55a}$$

$$E_{v,wi}(t)A = \sum E_v(t) b_{i,trans} h_i \tag{7.55b}$$

Where  $E_{v,oc}(t)$  and  $E_{v,wi}(t)$  are the viscoelastic moduli at a certain point in time,  $b_{i,trans}$  is the transformed width of every material,  $h_i$  is the height of the material, and  $A_{i,trans}$  is the

transformed surface of every material. As explained in section 7.5, the bending deflections is based on the research from O'Ceallaigh, and the axial deformation is based on the research from Willebrands. Therefore  $EI = E_{v,oc}(t)I$  and  $EA = E_{v,wi}(t)A$

## 7.5 time-dependent P

By inserting the viscoelastic E-moduli in previous section, the strain and deflection Equations 7.48, 7.50 and 7.51 become dependent on time. Because of these changing strains over time, the prestress force  $P$  will also be dependent on time. When the strains in the prestress material decrease, the prestress force will decrease and also the other way around. This time-dependent prestress force is calculated numerically because both the strains and the prestress force are dependent on each other. This is done using a loop over the  $x$ -coordinate within a loop over the time. For every time step, the corresponding creep strains and prestress force are calculated based on a convergence criterion as explained in this section.

### 7.5.1 Starting principle

At the initial moment ( $t = t_0 = 0$ ), the prestress force is  $P_0$  and the initial strains are divided into axial and bending strains (as explained in Section 7.2)  $\epsilon_{i,n}(t = t_0)$  and  $\epsilon_{i,b}(x, t = t_0)$ , with  $i = 1, 2$ . These strains are calculated based on the creep load model from Section 4.4. This part calculates the initial strains ( $t = t_0$ ) for every  $x$ -value.

### 7.5.2 First time step

With  $t$  going from  $t = t_0$  to  $t = t_1$ , the viscoelastic E-moduli decrease and as a result the strains increase. To find the difference in strains, the strains at the starting criterium ( $t = t_0$ ) are stored as  $\epsilon_a$ , for bending (b) and axial (n), see Equation 7.56. These strains are based on the initial prestress force and the initial bending- and axial stiffnesses.

$$\epsilon_{a,b} = \epsilon_{i,b}(x, t = t_0) \quad (7.56a)$$

$$\epsilon_{a,n} = \epsilon_{i,n}(x, t = t_0) \quad (7.56b)$$

And the strains for the first time step ( $t = t_1$ ) are stored as in Equation 7.57. For this timestep, the stiffnesses have decreased according to the relations in section 7.4.4.

$$\epsilon_{b,b} = \epsilon_{i,b}(x, t = t_1) \quad (7.57a)$$

$$\epsilon_{b,n} = \epsilon_{i,n}(x, t = t_1) \quad (7.57b)$$

To find the corresponding prestress losses due to the increased strains, first the change in strains is calculated:

$$\delta\epsilon_b = \epsilon_{b,b} - \epsilon_{a,b} \quad (7.58a)$$

$$\delta\epsilon_n = \epsilon_{b,n} - \epsilon_{a,n} \quad (7.58b)$$

Corresponding change in prestress losses:

$$\delta P_b = \delta\epsilon_b E_p A_p \quad (7.59a)$$

$$\delta P_n = \delta\epsilon_n E_p A_p \quad (7.59b)$$

And resulting prestress force due to bending and axial creep:

$$P_{1,tot} = P_0 + \delta P_b + \delta P_n \quad (7.60)$$

### 7.5.3 Convergence criterion

The calculated prestress force at time  $t = t_1$  in Equation 7.60 is different from the initial prestress force  $P_0$ , therefore new iterations should be done to obtain new strains. This is done within a loop until convergence is reached. First the new  $\epsilon_a$  and  $\epsilon_b$  are calculated.  $\epsilon_a$  is equal to the  $\epsilon_b$  from the previous iteration and  $\epsilon_b$  is calculated with  $\epsilon_{i,b}(x, t = t_1)$  and  $\epsilon_{i,n}(x, t = t_1)$  based on the prestress force  $P_{1,tot}$  calculated from the previous iteration:

$$\epsilon_{a,b} = \epsilon_{b,b} \quad (7.61a)$$

$$\epsilon_{a,n} = \epsilon_{b,n} \quad (7.61b)$$

$$P = P_{1,tot} \quad (7.62)$$

$$\epsilon_{b,b} = \epsilon_{i,b}(x, t = t_1) \quad (7.63a)$$

$$\epsilon_{b,n} = \epsilon_{i,n}(x, t = t_1) \quad (7.63b)$$

Then, the new prestress force is calculated according to following equations:

$$\delta\epsilon_b = abs(\epsilon_{a,b}) - abs(\epsilon_{b,b}) \quad (7.64a)$$

$$\delta\epsilon_n = \text{abs}(\epsilon_{a,n}) - \text{abs}(\epsilon_{b,n}) \quad (7.64b)$$

$$\delta P_b = \delta\epsilon_b E_p A_p \quad (7.65a)$$

$$\delta P_n = \delta\epsilon_n E_p A_p \quad (7.65b)$$

$$P_{1,tot} = P + \delta P_b + \delta P_n \quad (7.66)$$

The model loops through these equations until the convergence criterion is reached. The convergence criterion is reached when  $\delta P_n + \delta P_b < 1$  Newton. When this point is reached, the right prestress force and strains at time  $t = t_1$  are known. With this prestress force as input, also the right deflection of the deck at the actual x-coordinate can be determined with the formulas for  $w_{i,b}(x, t)$  from Equations 7.51a and 7.51b.

#### 7.5.4 General principle

For time steps bigger than  $t_1$ , same approach as from Equations 7.61 to 7.66 is used. This is generalized in next equations. First, values for  $\epsilon_a$  are calculated based on the prestress force  $P_{1,tot}$  calculated for previous time step  $t = t_{n-1}$ .

$$\epsilon_{a,b} = \epsilon_{b,b}(x, t = t_{n-1}) \quad (7.67a)$$

$$\epsilon_{a,n} = \epsilon_{b,n}(x, t = t_{n-1}) \quad (7.67b)$$

$$P = P_{1,tot} \quad (7.67c)$$

Then, values for  $\epsilon_b$  are calculated based on the new prestress force  $P$  and decreased stiffnesses based on the time:

$$\epsilon_{b,b} = \epsilon_{i,b}(x, t = t_n) \quad (7.67d)$$

$$\epsilon_{b,n} = \epsilon_{i,n}(x, t = t_n) \quad (7.67e)$$

$$\delta\epsilon_b = \text{abs}(\epsilon_{a,b}) - \text{abs}(\epsilon_{b,b}) \quad (7.67f)$$

$$\delta\epsilon_n = \text{abs}(\epsilon_{a,n}) - \text{abs}(\epsilon_{b,n}) \quad (7.67g)$$



$$\delta P_b = \delta \epsilon_b E_p A_p \quad (7.67h)$$

$$\delta P_n = \delta \epsilon_n E_p A_p \quad (7.67i)$$

$$P_{1,tot} = P + \delta P_b + \delta P_n \quad (7.67j)$$

Then, according to the convergence principle, there is iterated towards a solution at time  $t = t_n$  which has a prestress force and strains that correspond to each other. Using the equations presented in this section, the creep strains and corresponding prestress losses can be calculated for every time instant.

# 8. Long-term results

This chapter presents the results from the long-term model that is described in Chapter 7. For all results, FRP is used for the input values of the reinforcement and the prestress tendons:

Elastic modulus:  $E = 250\,000\text{ N/mm}^2$   
 Maximum strength:  $f = 1500\text{ N/mm}^2$

## 8.1 Deflection

The final deflection is the sum of the instantaneous SLS deflections and the creep deflections. Both quantities are analysed in this section.

### 8.1.1 SLS deflection

For the maximum instantaneous deflections of the deck, the SLS load model from section 4.3 is used. With the ODE system from section 7.2, the instantaneous deflections can be determined. These are presented in Figure 8.1 for the location with the highest deflection. It can be seen that the total instantaneous deflection linearly depends on the initial prestress force. All graphs are calculated with parabolic tendons, except for graph (D).

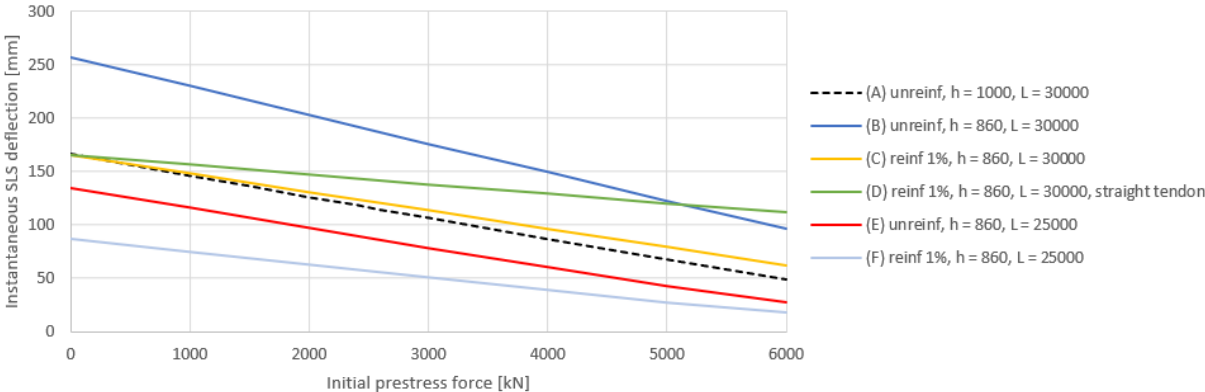


Figure 8.1: Instantaneous deflections bases on SLS load model

For the instantaneous deflection:  $t = 0$ . An initial E-modulus of  $13500\text{ N/mm}^2$  is used, so no time-dependent decrease is present. The structural height of the timber deck has a large

influence on the instantaneous deflection. Increasing the structural height from 860 (B) to 1000 mm (A) results in a decrease in deflection of 35-48%, depending on the initial prestress force. By adding 1% (0.5% top, 0.5% bottom) reinforcement (C) to an unreinforced deck (B), the deflections decrease by 35%. The span also has a large influence on the initial deflections. Decreasing the span from 30000 to 25000 mm will decrease the deflection by 47-71% (depending on the initial prestress force), both for a reinforced and non-reinforced section. Further analysis of the effect of the span on the output is given in Section 8.3

The SLS deflections of the straight tendons (D) are up to 79% higher than the SLS deflections of the parabolic tendons (C). This is further explained by Figures 8.2 and 8.3. These graphs present the instantaneous SLS moment- and deflection graphs for a prestress force of 3000 kN. Straight prestress tendons are less efficient in decreasing the final deflection of the deck. This can be seen by the moment lines of both tendon profiles. The parabolic tendons counteract the moments from the action loads, while the straight tendons do not exert a maximum counteracting moment at the location where the action moments are highest.

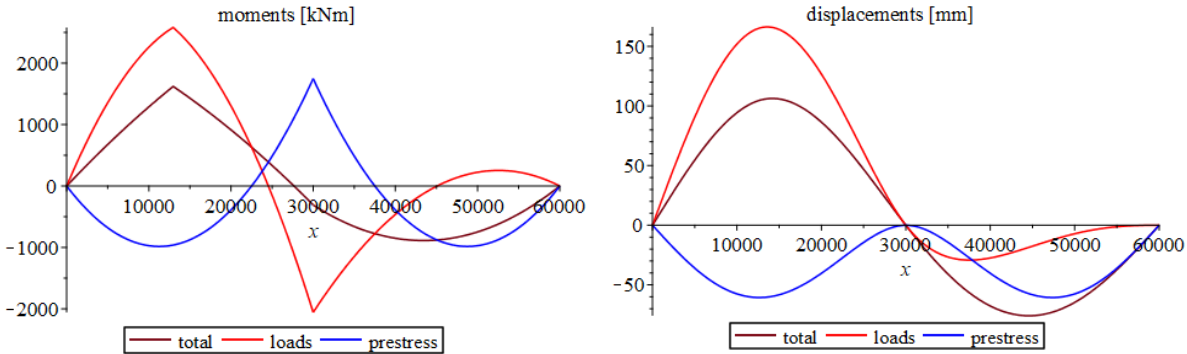


Figure 8.2: Moment- and deflections plots for parabolic tendons (P = 3000 kN)

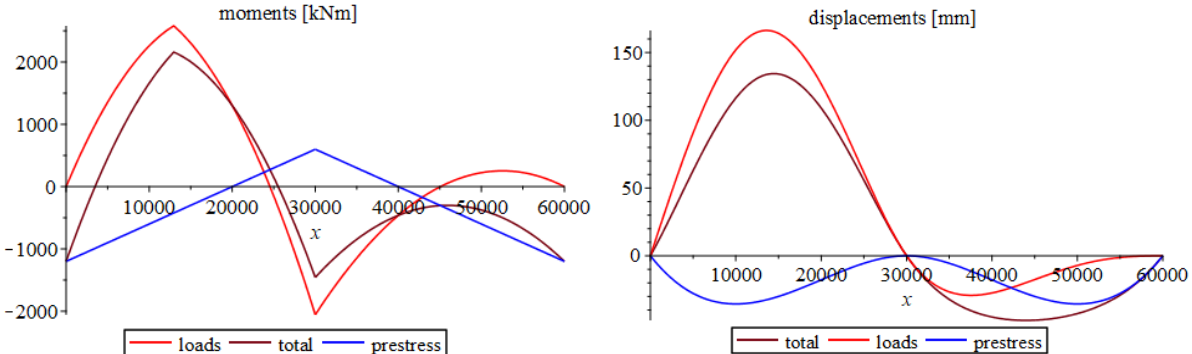


Figure 8.3: Moment- and deflections plots for straight tendons (P = 3000 kN)

Besides the deflections, parabolic tendons are more beneficial for the moment resistance of the deck. To resist the negative hogging moment at the midspan of the deck, a tendon at the upper side of the cross-section is desired. This is not the case with straight tendons. While

parabolic tendons are located at the lower side where the action moment is positive, and at the upper side where the action moment is negative.

### **8.1.2 Creep deflection**

The time-dependent creep deflection is calculated according to the model as described in Chapter 7. For every timestep and x-value, the creep deflections are calculated based on the creep load model. The load model for creep loads is the same for span 1 and 2, see Section 4.4. Therefore, the model is only used to produce results for span 1, since results for span 2 will be the same but mirrored. To explain the behaviour according to the model, the creep deflection is visualized for prestress forces from 0 to 6000 kN in Figure 8.4. The time  $t$  is given in hours, where 438000 hours corresponds to 50 years. The behaviour is based on an unreinforced cross-section with parabolic prestress tendons. It should be noted that positive deflections are in the downward direction. From Figure 8.4 can be concluded that up to an initial prestress force of around 2200 kN, both the instantaneous deflection and the deflection after 50 years are positive (in downward direction). This means that creep results in an increasing deflection over time. At  $P = 2600$  kN, the prestress causes a negative instantaneous deflection because the loads exerted by the prestress force are larger than the loads of the creep load model. However, due to creep of the prestress material, prestress force is lost and therefore the deck creeps in positive direction. This means that creep still causes a deflection in positive direction (downwards). This effect disappears from an initial prestress force of 4000 kN. From that moment, the prestress force is large enough to cause a creep deflection in negative direction (upwards). This can be seen at an initial prestress force of 6000 kN, where the prestress loads are so large that the bridge deck will creep in upward direction.

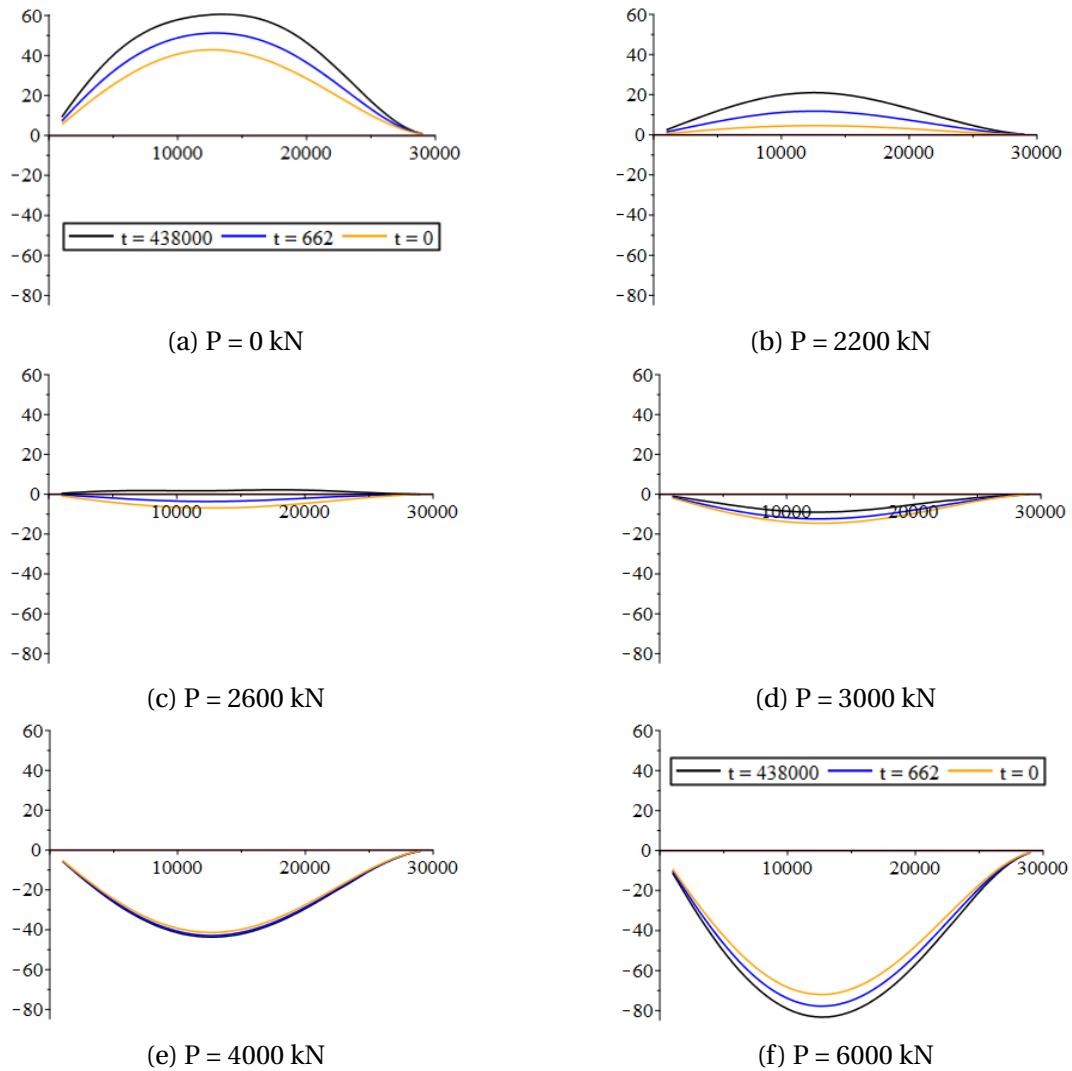


Figure 8.4: Creep deflections for varying initial prestress forces

As mentioned in Section 7.4.2, the creep curves used as input for the model are subject to uncertainty. Therefore, the sensitivity of the creep deflection to changes in the creep curves are analyzed. First for a non-reinforced prestressed deck with parabolic tendons, second for a reinforced prestressed deck with parabolic tendons and third for a reinforced straight tendon prestressed deck that is reinforced. The creep deflection is calculated for varying creep curves. This is done for three creep curves (see Figure 8.5):

- The original creep curves as determined in Section 7.4.2. Where  $m_{oc} = 0.14$ ,  $n_{oc} = 0.13$ ,  $m_{wi} = 0.34$  and  $n_{wi} = 0.11$ .
- Conservative creep curves, where the curve of O’Ceallaigh is increased with +100% and the curve of Willebrands with +50%. The curve of Willebrands was already far above the curve of O’Ceallaigh, therefore the curve of O’Ceallaigh is increased with a larger amount.

- Optimistic creep curves, where the curves of O’Ceallaigh and Willebrands are decreased with -50%.

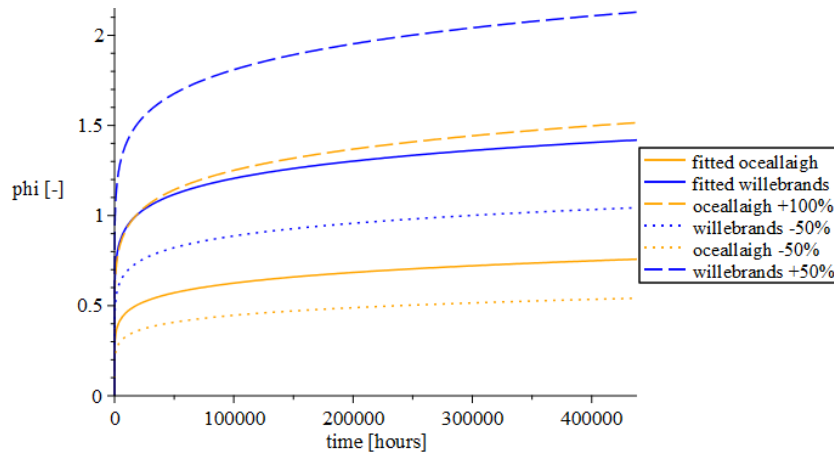


Figure 8.5: Varying creep curves as input for sensitivity analysis

The creep deflection is calculated as follows:

$$w_{creep} = w_{t50} - w_{t0} \quad (8.1)$$

### Non-reinforced deck, no prestress tendons

A reference value of creep deflection is calculated based on a deck without reinforcement and without prestress tendons (a pure timber deck). This is done in Figure 8.6 for the different creep curves. The corresponding deflection values can be found in Table 8.1

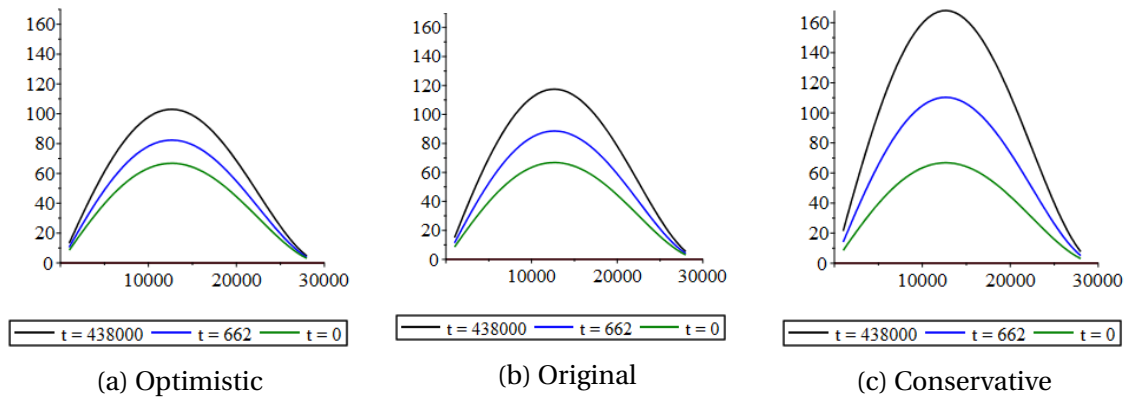


Figure 8.6: Instantaneous- and creep deflections of a pure timber deck

From the table can be seen that the creep will increase the deflection by a very large percentage: 76% for the original creep curve and 149% for the conservative creep curve. The creep deflections are also presented based on Eurocode for Climate Class 2 and Climate Class 3.

	optimistic	original	conservative	Eurocode CC2	Eurocode CC3
$w_{t0}$	67	67	67	67	67
$w_{t50}$	103	118	167	121	201
$w_{creep}$	36 (+53%)	51 (+76%)	100 (+149%)	54 (+81%)	134 (+200%)

Table 8.1: Deflection values for a pure timber deck [mm]

### Non-reinforced deck, parabolic tendons

The different creep curves from Figure 8.5 are implemented in the model. The final creep deflections (at the location where they are largest) for a non-reinforced deck are presented in Figure 8.7 for varying initial prestress forces. A large decrease in creep deflection is obtained with respect to the pure timber beam. For a prestress force up to 2000 kN, the creep deflection decreases to around 27 mm. This is almost half of the creep of the pure timber beam. For very large prestress forces, the creep deflection becomes negative. Meaning that the deck will creep in upward direction.

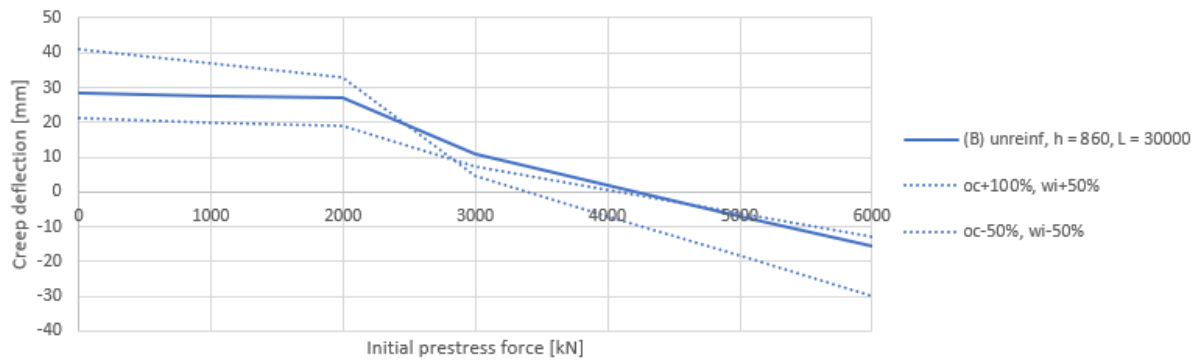


Figure 8.7: Creep deflections for unreinforced deck (L = 30 m)

For initial prestress forces of 0 and 6000 kN, following changes in creep deflection are calculated with respect to the original creep deflection of (B):

	oc+100%, wi+50%	oc-50%, wi-50%
P = 0 kN	+12.9 mm (+45%)	-7.0 mm (-25%)
P = 6000 kN	-14.2 mm (+89 %)	+2.8 mm (-18%)

Table 8.2: Non-reinforced: creep deflection results with different creep curve input

### Reinforced deck, parabolic tendons

The same as previous section is done, now with a 1% reinforced deck. Where 0.5% is allocated at the top, and 0.5% is allocated at the bottom. The results are presented in Figure

8.8. It can be seen that the creep deflections significantly decrease with respect to the unreinforced deck (B). It should be noted that for a prestress force of slightly below 6000 kN, the creep deflection is zero. Meaning that the creep due to the prestress load exactly compensate the creep due to the creep load model.

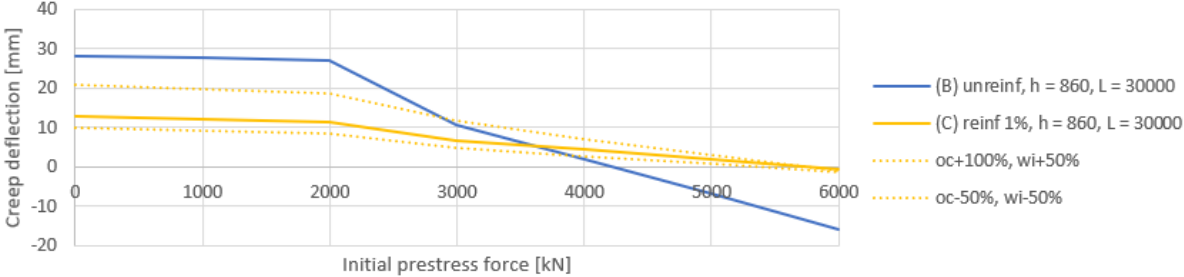


Figure 8.8: Creep deflections for reinforced deck (L = 30 m)

For initial prestress forces of 0 and 6000 kN, following changes in creep deflection are calculated with respect to the creep deflection of (C):

	oc+100%, wi+50%	oc-50%, wi-50%
P = 0 kN	+7.9 mm (+61%)	-3.1 mm (-24%)
P = 6000 kN	-0.5 mm (+94 %)	-0.7 mm (+144%)

Table 8.3: Non-reinforced: creep deflection results with different creep curve input

The absolute changes at P = 6000 kN are small. The percentage changes are large because of the small creep deflection of (C) at P = 6000 kN, which are all close to 0.

**Reinforced deck, straight tendons**

The creep deflection are calculated for a 1% reinforced deck with straight prestress tendons. The results are presented in Figure 8.9. It can be seen that the creep deflections slightly increase with respect to the reinforced deck with parabolic tendons (D).

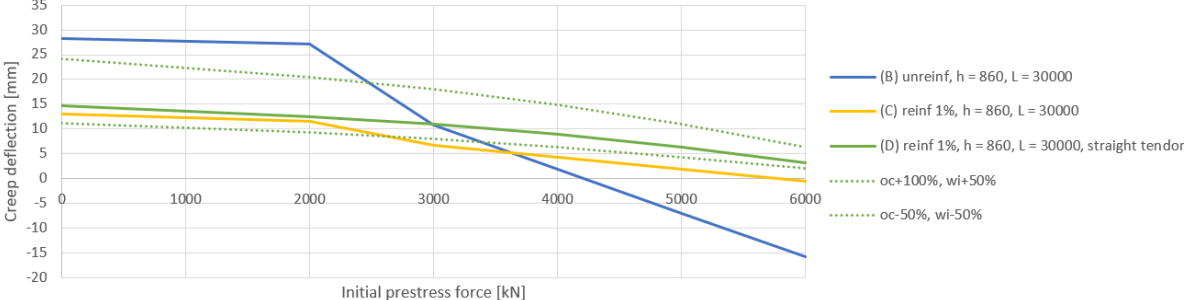


Figure 8.9: Creep deflections for reinforced deck with straight tendons (L = 30 m)



For initial prestress forces of 0 and 6000 kN, following changes in creep deflection are calculated with respect to the creep deflection of (D):

	oc+100%, wi+50%	oc-50%, wi-50%
P = 0 kN	+9.3 mm (+63%)	-3.5 mm (-24%)
P = 6000 kN	+3.1 mm (+93 %)	-1.2 mm (-36%)

Table 8.4: Non-reinforced: creep deflection results with different creep curve input

### 8.1.3 Total deflection

The total final deflection is the sum of the instantaneous deflection (Section 8.1.1) and the creep deflection  $w_{creep}$  (Section 8.1.2), this is displayed in Figure 8.10. Also the total deflections based on the conservative and optimistic creep curves are displayed. According to the outcomes of the model, the creep deflections are small with respect to the instantaneous SLS deflections. The conservative creep deflections (based on oc+100% and wi+50%) are small with respect to the instantaneous deflections. For the unreinforced deck (B), the increase from SLS deflection to the total deflection (for oc+100% and wi+50%) is 16.0% at maximum. For the reinforced deck (C) this percentage is 12.6%, and for the deck with straight tendons (D) this percentage is 14.5%

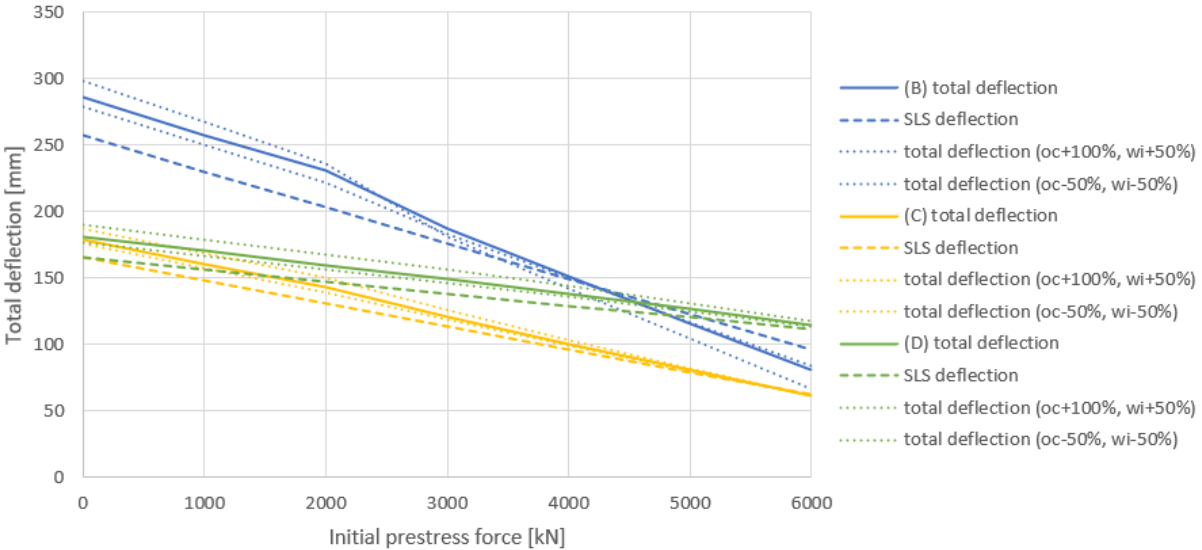


Figure 8.10: Deflections at t = 50 years including uncertainty of creep curves

### 8.2 Moment decrease

Because of the long-term creep of the timber deck, losses will occur in the prestress material. This will change the bending moment resistance over time. The model as explained in

Chapter 7 is used to analyze this behaviour. The model is executed for timesteps up to 50 years (= 438000 hours) and for 50 x-values over span l.

### 8.2.1 Creep strains

Executing the model results in a matrix for the bending strains  $\epsilon_b$  over time, and a matrix for the axial strains  $\epsilon_n$  over time. As explained in Section 7.3, the strains are calculated at the location of the prestress tendons, denoted with  $z_i$ . To find the change in strains  $\Delta\epsilon_{tot}$  (= creep strains) with respect to the initial strains, the initial strains are subtracted from the strains calculated at every time instant:

$$\text{Axial creep strains: } \Delta\epsilon_{n,t} = \epsilon_{n,t} - \epsilon_{n,t0} \quad (8.2a)$$

$$\text{Bending creep strains: } \Delta\epsilon_{b,t} = \epsilon_{b,t} - \epsilon_{b,t0} \quad (8.2b)$$

$$\text{Creep strains: } \Delta\epsilon_{tot} = \Delta\epsilon_{n,t} + \Delta\epsilon_{b,t} \quad (8.2c)$$

In Section 8.2.2, these creep strains are used to determine the moment resistance decrease due to creep of the prestress tendons. The creep strains are calculated for varying values for the initial prestress force. To sketch the behaviour, this is presented in Figure 8.11 - 8.13 for a prestressed deck with parabolic tendons, no reinforcement. Where  $t$  is the time in hours,  $t = 438000$  hours corresponds to 50 years. The horizontal axis is the longitudinal coordinate  $x$ . What can be seen from the increasing initial prestress force, is that at a certain point the moments due to prestress become larger than the moments due to the creep load moment. This implies that the initial deflection will be negative, which means a deflection in upward direction. Therefore, the bending creep strains in Figure 8.13 become negative. Also, with increasing initial prestress force, the strains due to axial shortening become relatively larger while the bending strains become smaller. For an initial prestress force of 1000 kN, the axial strains are relatively small. Increasing the prestress force to 3000 kN and 5000 kN will give much larger strains due to axial shortening.

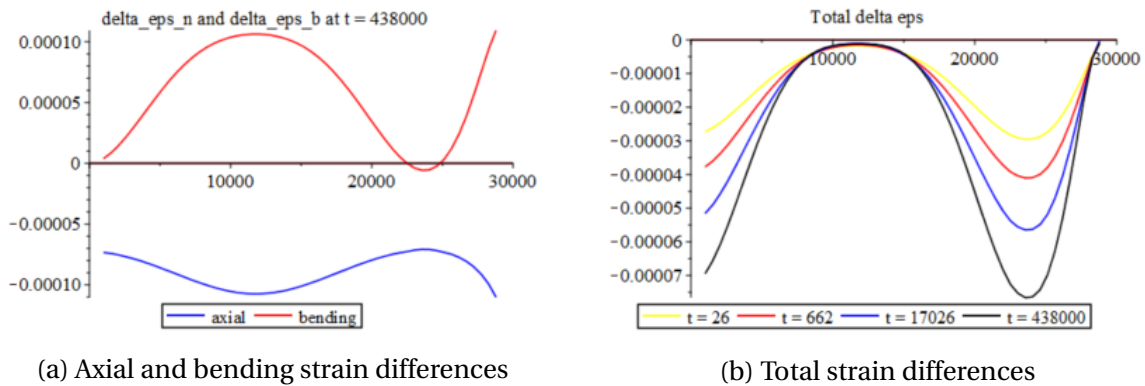
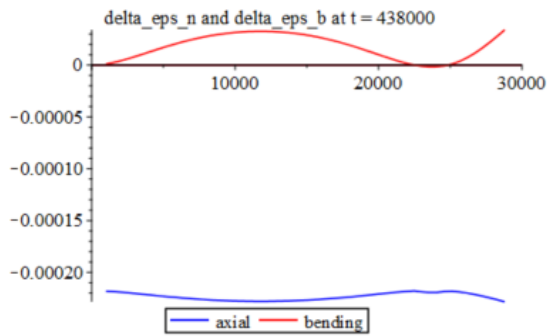
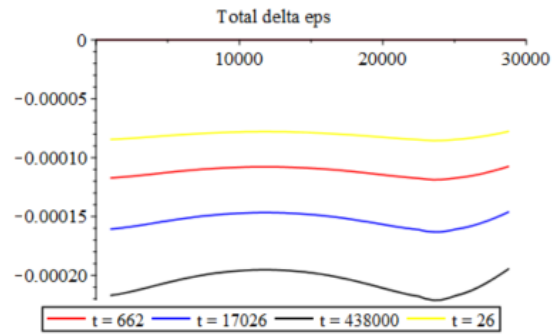


Figure 8.11: Strain differences for P = 1000 kN

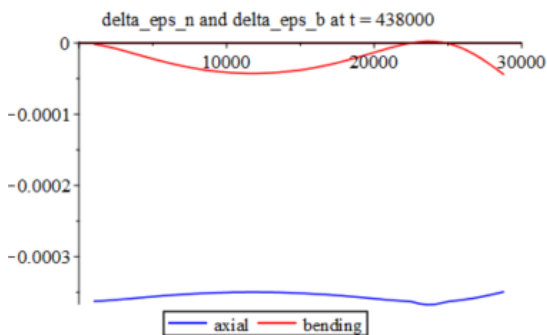


(a) Axial and bending strain differences

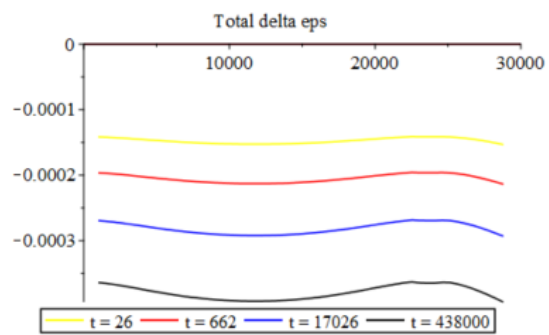


(b) Total strain differences

Figure 8.12: Strain differences for P = 3000 kN



(a) Axial and bending strain differences



(b) Total strain differences

Figure 8.13: Strain differences for P = 5000 kN

## 8.2.2 Moment decrease

The creep strains are calculated for the governing location, where the action moment is largest. With these creep strains, the decrease in moment resistance can be calculated. The creep strains are presented for varying initial prestress forces in Figure 8.14. The models are executed for prestress forces up to 6000 kN. For prestress forces bigger than 6000 kN, the models give initial bending stresses ( $\sigma_{cp}$ ) of in between 15 to 18 N/mm<sup>2</sup>, which already comes close the maximum bending strength of timber. So higher prestress forces could lead to failure of the deck. The graphs in Figure 8.14 are not linear. This is most clear in the graphs for the unreinforced variants (A) and (B) between an initial prestress force of 2000 - 3000 kN. It can also be seen from the unreinforced variant with smaller span (E), where the non-linearity occurs between 1000 and 2000 kN. Also the reinforced variants show this non-linearity. In these cases the non-linearity is smaller because of their increased stiffness. Only the variant with the straight prestress tendons (D) seems to have a graph without non-linearities. The non-linearity is explained by the total moment that changes sign. At lower initial prestress forces, the total moment (creep load model + prestress loads) is still positive. In this case the creep load model causes bigger moments than the prestress loads. By

increasing the initial prestress force, the prestress moments become higher than the creep load model, leading to a negative deflection. According to the model, this non-linearity due to change of moment sign is bigger for the unreinforced variants. It also stands out that decreasing the span from  $L = 30000$  to  $25000$  mm, increases the strain losses: graph (E) is below (B) and graph (F) is below graph (C).

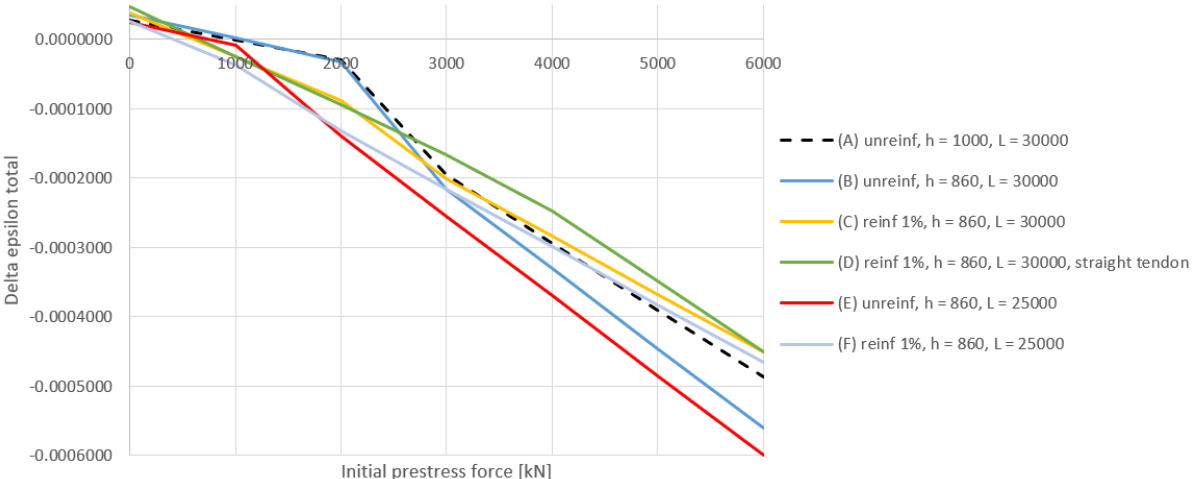


Figure 8.14: Change in strains of the prestress material due to creep

The creep strains are also calculated based on the conservative creep curves from Figure 8.5. These are presented in Figure 8.15. The creep strains increase up to 37% and 39% for an unreinforced (B) and reinforced (C) deck respectively. For the reinforced deck with straight tendons (D), the creep strains increase up to 31%. The creep strains for the deck with the straight tendons are smaller than those of the deck with parabolic tendons. The reason for this is that the bending creep strains become relatively larger than the axial creep strains because the deflections for the straight tendons are larger than the parabolic tendons.

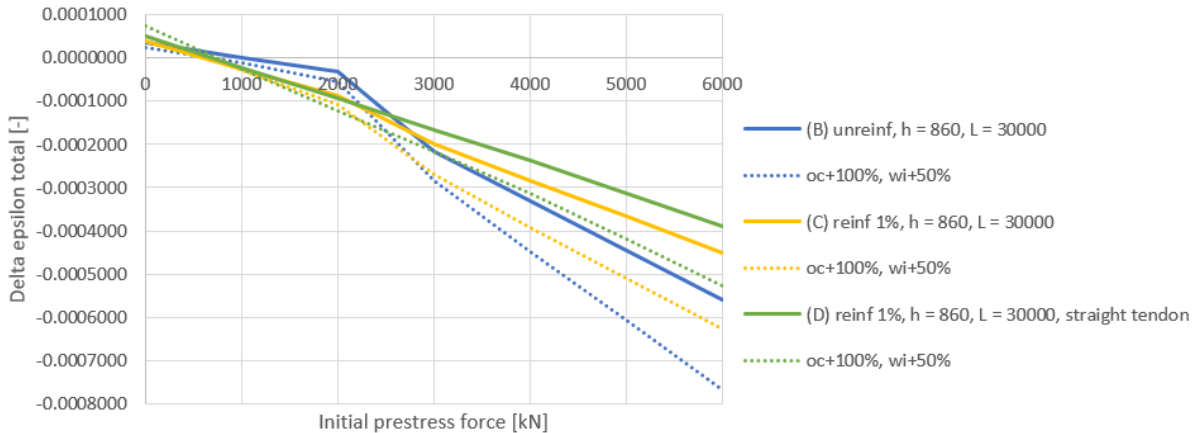


Figure 8.15: Change in strains (solid line), change in strains for conservative creep curves (dotted line)

The Python model is used to calculate the decreased bending moment resistance due to the creep strains. The creep strains  $\Delta\epsilon_{tot}$  are substituted into the Python model for a prestressed cross-section. At the initial elastic bending moment resistance, the strain in the prestress material is  $\epsilon_{tb,rf}$  (see Section 5.3.2). By taking into account the creep strains in the prestress material, the change in strains should be summed up with this initial strain. Then, the final strain will be:

$$\epsilon_{tb,rf,t} = \epsilon_{tb,rf} + \Delta\epsilon_{tot} \tag{8.3}$$

By substituting Equation 8.3 into the Python model, the decreased elastic bending moment resistance of the cross-section at  $t = 50$  years ( $= 438000$  hours) can be calculated. The resulting final resistance is presented in Figure 8.16. Only the reinforced- (B) and non-reinforced (C) decks with parabolic tendons are shown. The deck with straight tendons (D) has the same initial resistance as the reinforced deck (C). For clarity of the figure, (D) is not shown. The percentual bending resistance decrease is shown in Figure 8.17, also for the deck with straight tendons. The percentage is the decrease of the bending resistance at 50 years with respect to the initial bending resistance.

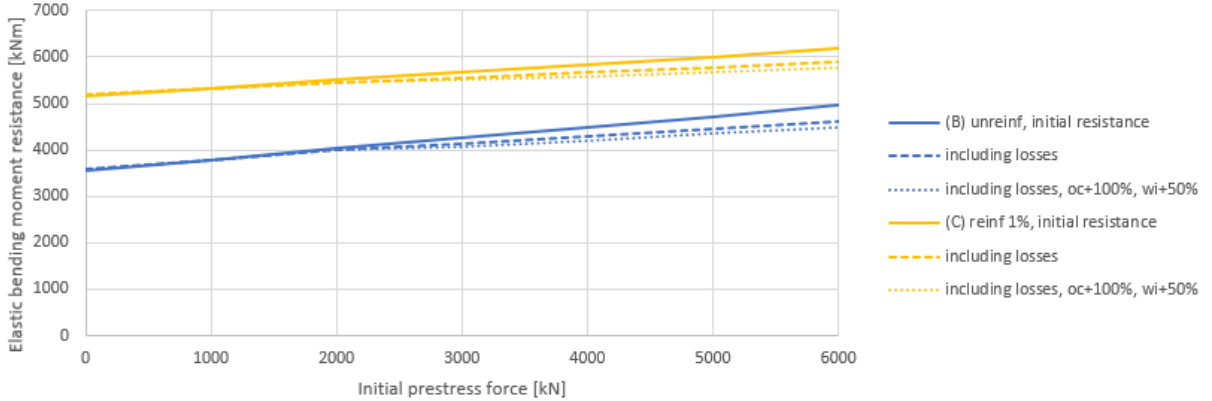


Figure 8.16: Final elastic resistances due to creep strains in prestress material

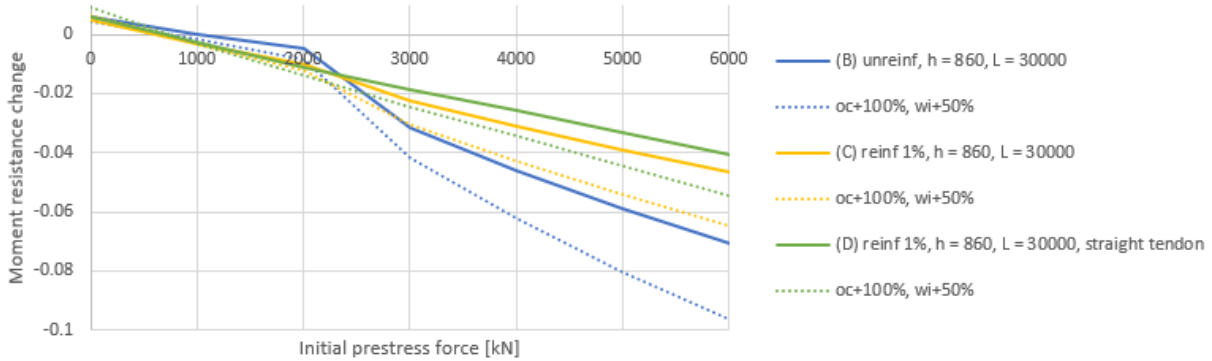


Figure 8.17: Change bending moment resistance at  $t = 50$  years

According to the model, the straight tendons have an elastic bending moment decrease of 4.0% based on the original creep curve. With the conservative creep curve, this percentage decrease becomes 5.6%. The reinforced section with parabolic tendons has a slightly larger bending moment decrease of 4.8% (original creep curve) and 6.6% (conservative creep curve). For a non-reinforced section, the bending moment decrease is much larger than the reinforced sections: 7.1% and 9.8%.

It can be seen that for initial prestress forces up to approximately 2000 kN, the graphs in both figures show a linear behaviour along the increasing prestress force. After 2000 kN, a non-linear behaviour occurs because at that point, the strain changes from Figure 8.14 also show a non-linear behaviour. The reason for the non-linear behaviour is that around a prestress force of 2000 kN, the moment due to prestress becomes bigger than the moment due to the creep loads. From that point, the strains due to bending creep also become negative, resulting in higher total strain changes according to Equation 8.2.

### **8.3 Span variation**

The span length  $L$  is varied to analyze the effect of the slenderness of the bridge deck. For the previous results, the span was kept constant at 30 meters (unless stated otherwise). In this section, spans of 25 and 35 will be analyzed. Resistance and deflections graphs are produced based on a reinforced deck with parabolic prestress tendons. Interpretation of these results regarding the slenderness is presented in the conclusion in Chapter 10.

#### **8.3.1 L = 25 meters**

The deflection is presented in Figure 8.18 for structural deck heights of 860, 760 and 700 mm. If also the asphalt layer of 140 mm is taken into account, these deck heights correspond to a slenderness of 25.0, 27.8 and 29.8 respectively. The total deflection is based on the original creep curve. For the deck with a height of 700 mm, also the total deflection based on the conservative creep curve is displayed. The total deflection decreases due to prestressing are 79%, 73% and 68% for deck heights of 860, 760 and 700 mm.

The elastic bending moment resistance is presented in Figure 8.19. The resistance including losses is based on the original creep curve. For the deck with a height of 700 mm also the resistance based on the conservative creep curve is displayed. For a span of 25 meters, the maximum ULS bending moment is 2848 kNm, see Figure 4.5a. From the graph can be seen that all resistances are above the ULS bending moment. The increase of bending moment resistance (including losses) for  $P = 6000$  kN with respect to zero prestress force is 13.9%, 15.8% and 17.1% for deck heights of 860, 760 and 700 mm.

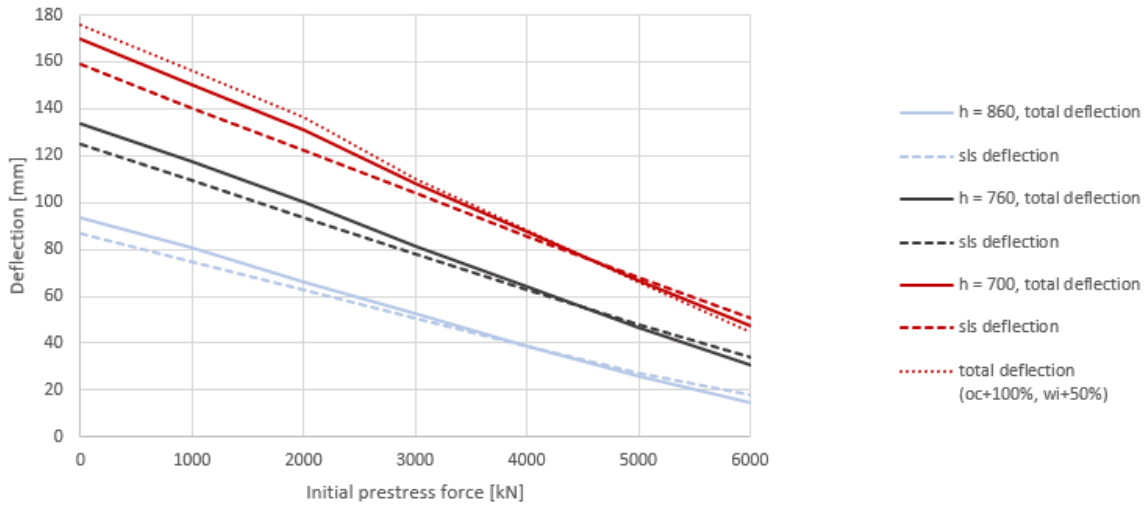


Figure 8.18: Deflections for varying initial prestress force based on a span of 25 meters

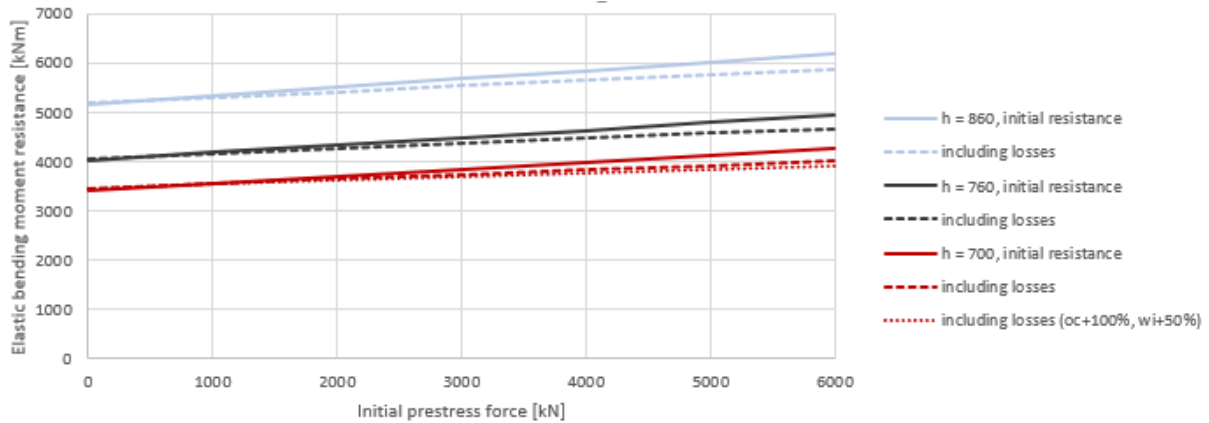


Figure 8.19: Elastic bending moment resistances for varying initial prestress forces based on a span of 25 meters

### 8.3.2 L = 35 meters

The deflection is presented in Figure 8.20 for structural deck heights of 900, 1000 and 1100 mm. The total height of the deck also includes an asphalt layer of 140 mm. The total deck heights are larger than the initial objective (see Section 1.4.2) of 1000 mm. However, also concrete solution have larger deck height for spans of over 35 meters. The slenderness of these total deck heights including asphalt layer is 33.7, 30.7 and 28.2. It can be seen that the deflection of the slender deck of 900 mm high deck becomes very large. The total deflection decreases due to prestressing are 51%, 56% and 61% for deck heights of 900, 1000 and 1100 mm.

The elastic bending moment resistance is displayed in Figure 8.21. For a span of 35 meters, the maximum action moment in ULS is 4854 kNm, see Figure 4.5c. It can be seen that the

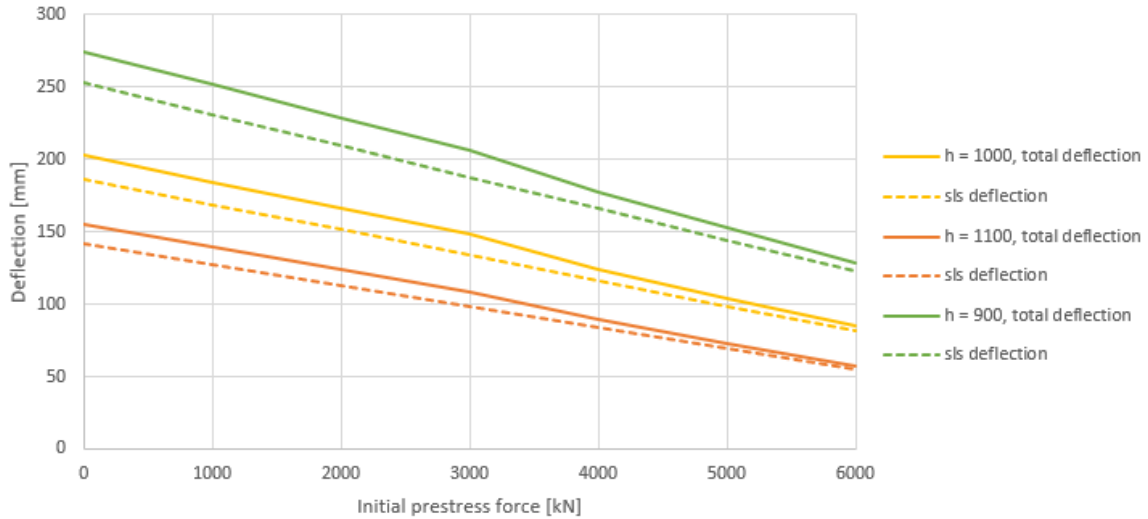


Figure 8.20: Deflections for varying initial prestress force based on a span of 35 meters

bending moment resistance is still larger than the action moment. The increase of bending moment resistance (including losses) for  $P = 6000$  kN with respect to zero prestress force is 13.0%, 12.2% and 11.1% for deck heights of 900, 1000 and 1100 mm.

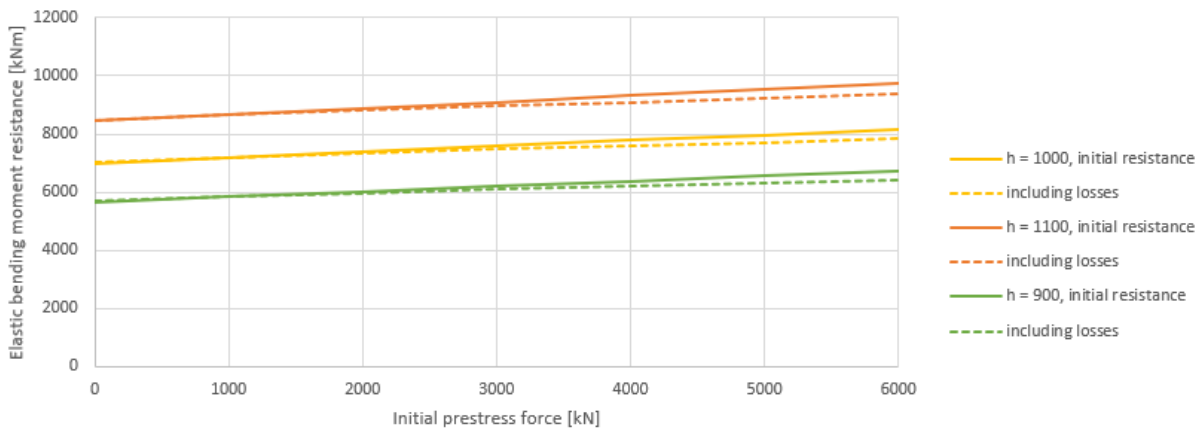


Figure 8.21: Elastic bending moment resistances for varying initial prestress forces based on a span of 35 meters



## 9. Discussion

In practice, the creep deflections should be calculated according to the  $k_{def}$  factor from Eurocode 5. According to Eurocode, the deflections should be based on SLS loads. To obtain the creep deflections, the SLS deflections should be multiplied by  $k_{def}$ . This is a very conservative assumption because in reality, the actual loads are much smaller than the SLS loads for a large part of the time. For more realistic results, the creep model in this research is based on a conservative approximation of 'normal' traffic loads. According to Eurocode, a service class 2 already gives a  $k_{def}$  factor of 1.8. Going to a service class 3,  $k_{def}$  even increases this factor to 3. These factors give much more conservative creep deflections than the creep deflections calculated from the long-term model in this research.

The creep model in this research gives a more realistic calculation for creep deformations of a timber deck. The conservative approach of Eurocode would give much larger deflections, resulting in increased deck height. Meaning that it would be more difficult to compete to the slenderness of reinforced concrete variants. However, some factors still cause uncertainty in the creep model of this research. Creep of the timber deck is based on two models from literature: the one of Gowda [37] for axial behaviour, and the one from O'Ceallaigh [38] for bending behaviour. The boundary conditions of both literature studies are different from those of the bridge deck in this research. The duration of Gowda was 4 years and of O'Ceallaigh was 1.5 year. The creep curves were then extrapolated, see Figure 7.11. Meaning that there is a significant uncertainty of creep behaviour up to 50 years, which is used for this research. Besides, both literature studies experimented with beams that had much smaller dimensions than the timber deck for this research. Also the climate conditions of O'Ceallaigh were kept constant at 20°C, with a regulated humidity. This is very different from an outdoor climate. All these factors incorporate uncertainty in the creep curves. To check whether the results are accurate, experiments with reinforced- and prestressed timber decks should be done. These experiments should be done based on longer periods of time. Then, less uncertainty will be caused by extrapolation of the creep curves. Also, the dimensions of the beams from Gowda and O'Ceallaigh are not representative for the dimensions of the bridge deck. It is unknown whether larger dimensions might induce more creep deflections. The long-term model can be calibrated based on more representative experiments with timber decks, increasing the final reliability of the outputs.

In this research, only the elastic bending moment resistance is taken into account for a prestressed deck. No increase of plastic moment resistance is taken into account. According to Section 6.1.1 and 6.1.2, the elastic bending moment resistance for a reinforced deck can

be increased by 30 to 40% before reaching the plastic resistance. It is expected that approximately the same bending moment increase can be obtained by a prestressed deck. Therefore, the elastic bending moment resistances can be increased to a plastic bending moment resistance. However, according to the results, the deflection is the governing factor for the maximum slenderness of the deck. Therefore, no plastic moment resistance for a prestressed deck is taken into account. For further optimization steps, implementation of a plastic moment resistance for a prestressed deck can be done in future work.

# 10. Conclusion

## Reinforcement- and prestressing layouts

The results of the cross-sectional model show that there exists a trade-off between stiffness and the ability to plastify. A timber deck with reinforcement in the tension side will be able to reach a higher bending moment resistance because of plastification of the cross-section. A timber deck with evenly distributed reinforcement over tension and compression side (50%/50%) will have the highest stiffness. However, a 50%/50% reinforced deck will also show a brittle failure. Adding prestress to a 50%/50% reinforced deck introduces a constant compression stress and a counteracting moment. The compression stress causes the tension in the bottom to be smaller and the compression in the top to be larger, which will trigger plastification instead of brittle failure. Therefore, prestressing a 50%/50% reinforced deck will, besides large stiffness, also incorporate ductility. After reaching the elastic bending moment resistance, the resistance will increase due to plastification of the deck. Therefore, more safety is taken into account

## Time-dependent deformations

The time-dependent deformations are calculated using the long-term model that is based on ODE relations combined with the viscoelastic E-modulus. Based on the long-term model, creep deformations are calculated for deck sections with or without additional reinforcement, straight or parabolic prestress tendons, different deck heights and different spans.

With respect to a pure timber deck (non-reinforced, non-prestressed), the long-term model gives large decreases in creep deflections. The pure timber deck had a creep deflection of 51 mm based on the original creep curve. According to the model, this creep deflection is reached after 50 years. By adding prestress tendons and/or reinforcement, decreased creep deflections were obtained. Following cases were investigated:

1. **Non-reinforced, parabolic tendons**
2. **Reinforced deck, parabolic tendons**
3. **Reinforced deck, straight tendons**

For these cases, decreased creep deflections were obtained (based on the original creep curves). Based on the original creep curve, the creep deflection of a pure timber deck was 51 mm. The decreased creep deflections for cases 1, 2, and 3 are displayed as  $w_{creep}$  in Table

10.1. A range of  $w_{creep}$  is given since it depends on the prestress force. The values correspond to a prestress force from 0 to 6000 kN. The creep deflection based on the conservative creep curve (oc+100%, wi+50%) is 100 mm for the pure timber deck. For cases 1, 2 and 3, creep deflections based on the conservative curve are displayed as  $w_{creep}(oc + 100\%, wi + 50\%)$  in Table 10.1. For the creep deflections based on the original and conservative creep curves, cases 1 and 2 will creep in upward direction for higher prestress forces. So: by choosing the right prestress force, the creep deflection can be decreased to 0. In this case, the creep due to the action loads is exactly compensated by the creep due to the prestress loads.

According to Section 8.1.2, deck with prestress forces up to 2000 kN result in the largest creep deflections. Even in these cases, the creep deflections are only a relatively small percentage of the total deflection. These percentages are displayed in Table 10.1 for the conservative creep curves. Even based on these conservative creep curves, the percentages are 16% at max. The other part of the total deflection exists of the instantaneous deflection based on the SLS load model

	$w_{creep}$ (for P = 0 to 6000 kN)	$w_{creep}$ (oc+100%, wi+50%)	Part of creep deflection to total deflection (oc+100%, wi+50%)
1	28 to -15 mm	41 to -30 mm	16%
2	13 to 0 mm	21 to -1 mm	13%
3	15 to 4 mm	24 to 6 mm	15%

Table 10.1: Creep deflection decrease for different deck cases, L = 30 m and h = 860 mm

**According to the results from the long-term model, it can be concluded that the creep deflection can be decreased to zero by choosing the right prestress force.** It should be noted however, that the instantaneous deflections based on the SLS loads play a much bigger role in the total deflection. From the graphs in Sections 8.1.1 and 8.3 can be seen that a large decrease in instantaneous deflection is obtained by incorporating prestress. This is summarized in Table 10.2 for different cases. The percentage in Table 10.2 is the decrease in deflection with respect to a deck section with 0 prestress force. Depending on the height of the deck, the decrease in instantaneous deflection may vary. It can also be seen that the straight tendons are less efficient in decreasing the deflection than the parabolic tendons. Based on the results of the model, it can be concluded that prestressing decreases the instantaneous deflection by a great amount.

unreinf, parabolic tendon, L = 25 m	-79%	for h = 860
unreinf, parabolic tendon, L = 30 m	-58 to -71%	for h = 800 to 1000 mm
reinf, parabolic tendon, L = 25 m	-68 to -80%	for h = 700 to 860 mm
reinf, parabolic tendon, L = 30 m	-60 to -62%	for h = 800 to 860 mm
reinf, parabolic tendon, L = 35 m	-51 to -61%	for h = 900 to 1100 mm
reinf, straight tendon, L = 30 m	-32%	for h = 860

Table 10.2: Instantaneous deflection decrease by incorporating a prestress force of 6000 kN

## Long-term prestress losses and final deck resistance

Because of creep, prestress losses will occur due to shortening of the prestress tendons. This is modelled with the long-term model. The creep strains become larger with increasing prestress force. Therefore, the decrease in bending moment resistance becomes larger for increased prestress forces. Because of uncertainty in the original creep curves, the creep strains were also calculated for the conservative creep curves (oc+100%, wi+50%). This resulted in significant increase of creep strains: up to 31 - 39% with respect to the original creep curves (depending on the deck configuration). By implementing these creep strains into the cross-sectional model, the decreased elastic bending moment resistances due to the prestress losses were found. From the graphs in Section 8.2.2 and 8.3 can be seen that the decrease in bending moment resistances is relatively small. The percentual decrease of the elastic bending moment resistance is presented in Table 10.3. These bending moment decreases are based on an initial prestress force of 6000 kN. For smaller initial prestress forces, the bending moment decrease will be smaller because a smaller initial prestress force will induce less prestress losses.

	original creep curve	conservative creep curve (oc+100%, wi+50%)
unreinf, parabolic tendon (L = 25 m, h = 860 mm)	-7.8 %	-11.2%
unreinf, parabolic tendon (L = 30 m, h = 860 mm)	-7.1%	-9.8%
reinf, parabolic tendon (L = 25 m, h = 700 mm)	-5.6%	-7.2%
reinf, parabolic tendon (L = 30 m, h = 860 mm)	-4.8%	-6.6%
reinf, parabolic tendon (L = 35 m, h = 1000 mm)	-4.1%	-6.0%
reinf, straight tendon (L = 30 m, h = 860 mm)	-4.0%	-5.6%

Table 10.3: Decrease of elastic bending moment resistance at  $t = 50$  years for an initial prestress force of 6000 kN

Taking into account the decrease of elastic bending moment over time, the total moment increase due to prestressing is presented in Table 10.4. The bending moment increase is calculated with respect to a prestress force of 0 kN. It stands out that a larger *unreinforced* span will increase the percentual increase of bending moment resistance, while a larger *reinforced* span will decrease the percentual increase of bending moment resistance.

	original creep curve	conservative creep curve (oc+100%, wi+50%)
unreinf, parabolic tendon (L = 25 m, h = 860 mm)	28.6%	23.4%
unreinf, parabolic tendon (L = 25 m, h = 860 mm)	31.6%	25.6%
reinf, parabolic tendon (L = 25 m, h = 700 mm)	17.1%	14.4%
reinf, parabolic tendon (L = 30 m, h = 860 mm)	15.2%	11.9%
reinf, parabolic tendon (L = 35 m, h = 1000 mm)	11.1%	9.3%
reinf, straight tendon (L = 30 m, h = 860 mm)	14.8%	13.0%

Table 10.4: Increase of elastic bending moment resistance at  $t = 50$  years for  $P_{ini} = 6000$  kN

## Slenderness

All deck configurations are subdivided into following groups:

- **Pure timber decks:** no reinforcement and prestress tendons are present
- **Reinforced deck:** 1% reinforcement is present in a 50% top, 50% bottom configuration. No prestress is added.
- **Prestressed deck:** prestressed tendons with parabolic profile, prestress force is 6000 kN. Contains no reinforcement.
- **Prestressed- and reinforced deck:** prestress tendons with parabolic layout, prestress force is 6000 kN. In combination with 1% reinforcement in a 50% top, 50% bottom configuration.
- **Straight tendons and reinforcement:** prestressed deck with straight tendons, prestress force is 6000 kN. In combination with 1% reinforcement in a 50% top, 50% bottom configuration.

### Slenderness for deflection

The total deflections at  $t = 50$  years are plotted against the slenderness for all deck configurations in Figure 10.1. As a reference, the deflection values from Section 4.5 are also presented in the figure. The plots show a clear distinction between the different deck configuration groups, shown in blue, grey, green, and yellow. The pure timber group shows the largest deflections. A clear decrease of deflection for the same slenderness is found for the reinforced group. According to the plots, a larger slenderness can be obtained by prestress (green group) than by reinforcement (grey group). The average line of the prestressed-reinforced decks (yellow group) lies slightly below the only prestressed decks (green group). So a little slenderness increase can be obtained by reinforcing an already prestressed deck. The reinforced- and prestressed deck with straight tendons show larger total deflections.

Eurocode gives guidelines of deflections for timber bridges:  $L/500$  to  $L/400$ , see Section 4.5. These deflection values can be reached with a prestressed- and reinforced deck according to the results. Taken into account a deflection limit of  $L/400$ , a slenderness of around 31 can be reached. The guidelines for deflections of beams give limits of  $L/300$  to  $L/150$ . For  $L/300$ , a slenderness of up to 33 can be reached. No results are produced for higher slendernesses. If the results would be extrapolated, a slenderness of over 35 could probably be reached according to the model for the limit  $L/150$ .

### Slenderness for strength

The relative bending moment resistance at 50 years is plotted against the slenderness in Figure 10.2. The relative bending moment is calculated by the elastic bending moment resistance at  $t = 50$  years divided by the ULS moment from Section 4.2.2. Meaning that for all points above a relative bending moment resistance of 1.0, following applies: elastic resistance > ULS action.

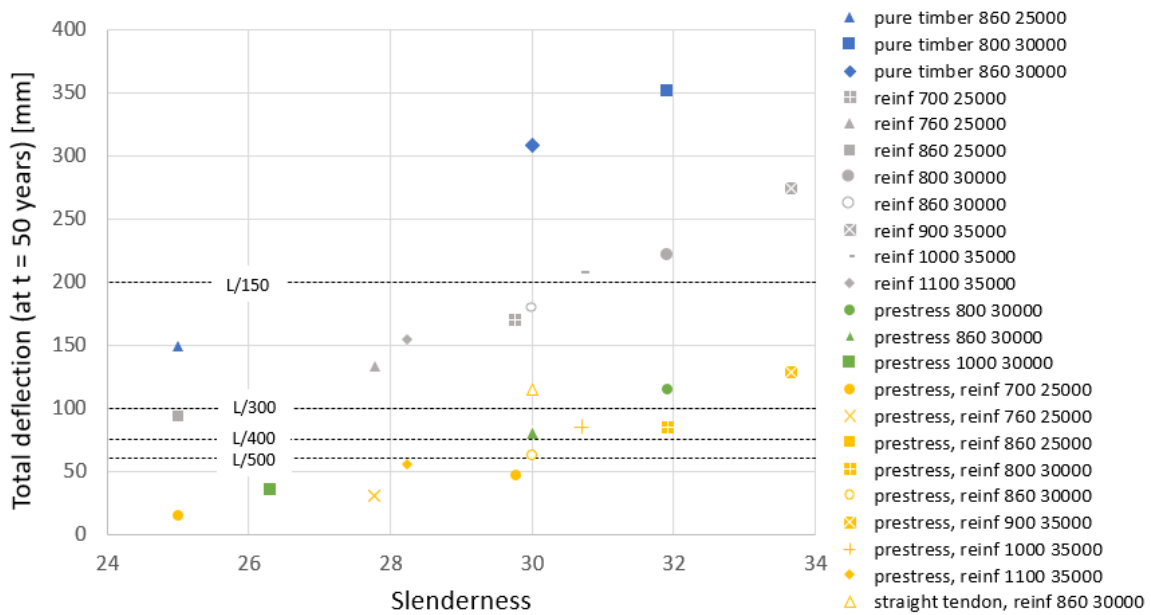


Figure 10.1: Slenderness and corresponding deflection for all investigated deck configurations (values in the legend are structural deck height  $h_{timber}$  and span  $L$ )

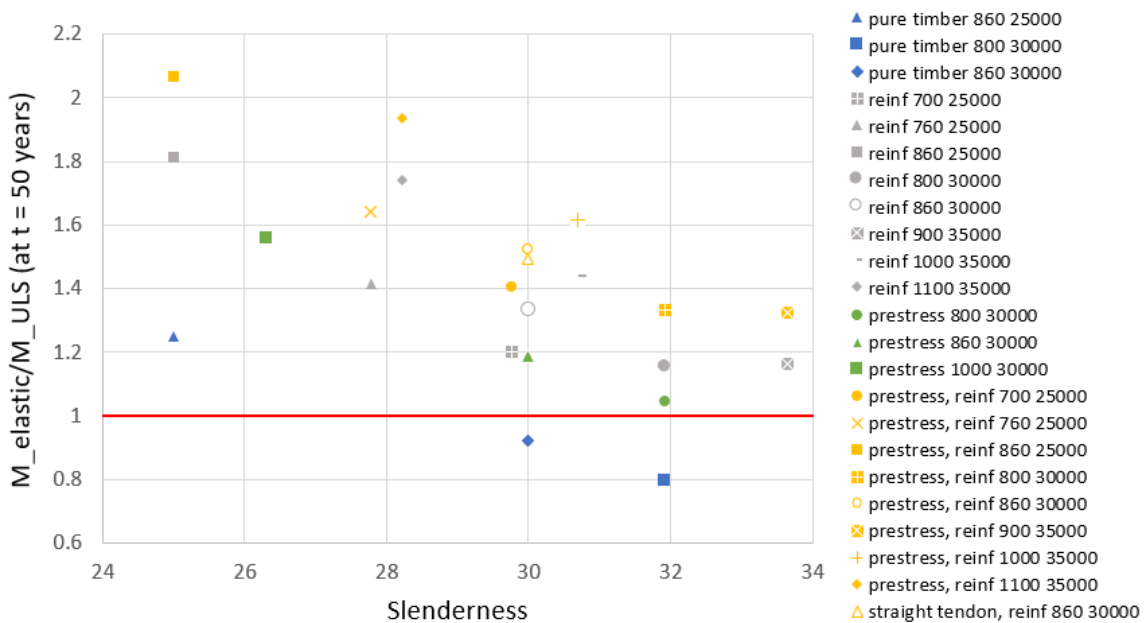


Figure 10.2: Slenderness and corresponding relative bending moment resistance for all investigated deck configurations (values in the legend are structural deck height  $h_{timber}$  and span  $L$ )

It can be seen that, on average, the group of prestressed- and reinforced decks (yellow) have the largest relative bending moment resistance. The prestressed group (green) has smaller relative bending moment resistance than the reinforced group (grey). This is because the

reinforcement allocation is 50% top, 50% bottom. This results in a larger elastic bending moment resistance than a prestress tendon in the bottom of the deck section. According to Section 6.2, the deck sections of the prestressed group will be able to plastify (= increased plastic moment resistance) after reaching the elastic bending moment resistance due to the fact that the tendons are located at the lower side of the beam. The reinforced deck will fail at the elastic limit because with a 50%-50% configuration, the maximum tension stress is reached at the same moment as the maximum compression stress. Meaning that the beam will fail on tension before plastification will happen.

Based on the results, a slenderness of at least 34 can be reached with a prestressed- and reinforced deck. It should be noted that the results are based on an elastic bending moment resistance. The prestressed- and reinforced deck will be able to reach an increased plastic bending moment resistance after reaching the elastic limit. Therefore, it is expected that a slenderness of over 36 can be reached for the bending moment resistance.

### **Final slenderness**

The goal for this research was a timber deck with a slenderness of around 30. With this slenderness, timber bridge variants are able to compete to reinforced concrete variants. According to the outcomes of the models, a slenderness of 31 can be reached based on the deflection guidelines of Eurocode. Depending on the strictness of the deflection limits required by the client, the slenderness might be increased to 33. If there are no requirements regarding deflections, the maximum slenderness should be based on strength. In this case a slenderness of at least 34 can be reached. If also the plastic bending moment resistance would be taken into account, the slenderness could reach 36 according to the results.



# Bibliography

- [1] Lefebvre, D. & Richard, G., “Design and construction of a 160-metre-long wood bridge in mistissini, québec,” in *Internationales Holzbau-Forum*, 2014.
- [2] Lu, Y., Cui, P. & Li, D., “Carbon emissions and policies in china’s building and construction industry: Evidence from 1994 to 2012,” *Building and Environment*, vol. 95, pp. 94–103, 8 2015.
- [3] Gan, V.J.L., Chan, C.M., Tse, K.T., Lo, I.M.C. & Cheng, J.C.P., “A comparative analysis of embodied carbon in high-rise buildings regarding different design parameters,” *Journal of Cleaner Production*, vol. 161, pp. 663–675, 5 2017.
- [4] Olivier, J.G.J., Janssens-Maenhout, G. & Peters, J.A.H.W., “Trends in global co<sub>2</sub> emissions,” tech. rep., PBL Netherlands Environmental Assessment Agency, 2012.
- [5] Zubizarreta, M., Cuadrado, J., Orbe, A. & García, H., “Modeling the environmental sustainability of timber structures: A case study,” *Environmental Impact Assessment Review*, vol. 78, 7 2019.
- [6] T. Johnson, “Comparison of environmental impacts of steel and concrete as building materials using the life cycle assessment method,” tech. rep., Massachusetts Institute of Technology, The address of the publisher, 6 2006.
- [7] Hildebrandt, J., Hagemann, N. & Thrän, D. , “The contribution of wood-based construction materials for leveraging a low carbon building sector in europe,” *Sustainable Cities and Society*, vol. 34, pp. 405–418, 7 2017.
- [8] haitsma beton. <https://www.haitsma.nl/bruggen-viaducten/algemeen/>. Accessed: 26-02-2021.
- [9] romein. <https://www.romein.nl/producten/bruggen-en-viaducten/rhe-brug/>. Accessed: 26-02-2021.
- [10] “Duurzaamheid als ontwerpcriterium voor beton - toegespitst op co<sub>2</sub>,” tech. rep., STUTECH/STUFIB, 10 2014.
- [11] Mettem, C.J., *timber bridges*. Spon Press, 2011.
- [12] Bank, L.C. & Mosallam, A.S., “Creep and failure of a full-size fiber-reinforced plastic pultruded frame,” *Composites Engineering*, vol. 2, pp. 213–227, 2 1991.

- [13] O’Born, R., “Life cycle assessment of large scale timber bridges: A case study from the world’s longest timber bridge design in norway,” *Transportation Research Part D: Transport and Environment*, vol. 59, pp. 301–312, 3 2018.
- [14] Abrahamsen, R.B., “Bridge across rena river - world’s strongest timber bridge.” SWECO, 2008.
- [15] Tjeerdsma, B. & Bongers, F., “The making of a traffic timber bridge of acetylated radiata pine,” in *European Conference on Wood Modification*, 1 2009.
- [16] Lugt, P. van der & Vogtlander, J., “Wood acetylation: A potential route towards climate change mitigation,” in *ECO-ARCHITECTURE*, vol. 142, 7 2014.
- [17] Ekholm, K, *Performance of Stress-Laminated-Timber Bridge Decks*. PhD thesis, Chalmers University of Technology, 2013.
- [18] “Design of timber structures,” tech. rep., Swedish Wood, 2006.
- [19] Dahl, K., Bovim, N.I. & Malo, K.A., “Evaluation of stress laminated bridge decks based on full scale tests,” WCTE 2006, 2006.
- [20] Ekholm, K., Kliger, R. & Crocetti, R., “Full-scale ultimate-load test of a stress-laminated-timber bridge deck,” *Journal of Bridge Engineering*, 7 2012.
- [21] Brooks, K.M., “Assessment of the environmental effects associated with wooden bridges preserved with creosote, pentachlorophenol, or chromated copper arsenate,” tech. rep., United States Department of Agriculture, 9 2000.
- [22] Franke, S., Franke, B. & Harte, A.M., “Failure modes and reinforcement techniques for timber beams – state of the art,” *Construction and Building materials*, vol. 97, pp. 2–13, 7 2015.
- [23] D’Aveni, A. & D’Agata, G., “Post-tensioned timber structures: New perspectives,” *Construction and Building Materials*, vol. 153, pp. 216–224, 10 2017.
- [24] Walraven, J.C. & Braam, C.R., *Prestressed Concrete*. 2019.
- [25] Kliger, R., Al-Emrani, M., Johansson, M. & Crocetti, R., “Strengthening timber with cfrp or steel plates - short and long-term performance,” 1 2008.
- [26] Gentile, C., Svecova, D. & Rizkalla, S.H., “Timber beams strengthened with gfrp bars: Development and applications,” *Journal of Composites for Construction*, vol. 6, pp. 11–20, 2 2002.
- [27] Blaß, H.J. & Romani, M., “Design model for frp reinforced glulam beams,” 2001.
- [28] Hoseinpour, H., Valluzzi, M.R., Garbin, E. & Panizza, M., “Analytical investigation of timber beams strengthened with composite materials,” *Construction and Building Materials*, vol. 191, pp. 1242–1251, 8 2018.

- [29] Kliger, M., Haghani, R., Brunner, M., Harte, A.M. & Schober, K., “Wood-based beams strengthened with frp laminates: improved performance with pre-stressed systems,” *European Journal of Wood and Wood Products*, 5 2016.
- [30] Yang, H., Ju, D., Liu, W. & Lu, W., “Prestressed glulam beams reinforced with cfrp bars,” *Construction and Building Materials*, vol. 109, pp. 73–83, 4 2016.
- [31] Brunner, M. & Schnueriger, M., “Timber beams strengthened by attaching prestressed carbon frp laminates with a gradiented anchoring device,” 2005.
- [32] “Bonding of timber,” Tech. Rep. 1, COST, 3 2008.
- [33] Brady, J.F. & Harte, A.M., “Prestressed frp flexural strengthening of softwood glue - laminated timber beams,” 1 2008.
- [34] Luca, V. De & Marano, C., “Prestressed glulam timbers reinforced with steel bars,” *Construction and Building materials*, vol. 30, pp. 206–217, 5 2012.
- [35] Palermo, A., Giorgini, S., Stefano, P. & Buchanan, A.H., “Potential of longitudinal post-tensioning for short-to-medium span timber bridges,” *Structural Engineering International*, 04 2018.
- [36] Willebrands, A., “Differential vertical shortening in timber-concrete high-rise structures,” 11 2017.
- [37] Gowda, C., Korteesmaa, M. & Ranta-Maunus, A., *Long term creep tests on timber beams on heated and non-heated environments*. Espoo: Technical Research Centre of Finland (VTT), 1996.
- [38] O’Ceallaigh, C., Sikora, K., McPolin, D. & Harte, A.M., “The mechano-sorptive creep behaviour of basalt frp reinforced timber elements in a variable climate,” *Engineering Structures*, vol. 200, 9 2019.
- [39] O’Ceallaigh, C., Sikora, K., McPolin, D. & Harte, A.M., “Modelling the hygro-mechanical creep behaviour of frp reinforced timber elements,” *Construction and Building materials*, vol. 259, 6 2020.
- [40] Fragiacomio, M. & Davies, M., “Long-term behavior of prestressed lvl members. i: Experimental tests,” *Journal of Structural Engineering*, 02 2011.
- [41] Fragiacomio, M. & Davies, M., “Long-term behavior of prestressed lvl members. ii: Analytical approach,” *Journal of Structural Engineering*, 03 2011.
- [42] Toratti, T., “Creep of timber beams in a variable environment,” *Materials Science*, 1992.
- [43] Lantsoght, E.O.L., Veen, C. van der & Walraven, J., “Recommendations for the shear assessment of reinforced concrete slab bridges from experiments,” *Structural Engineering International*, 04 2013.

- [44] Blaß, H.J. & Romani, M., “Reinforcement of glulam beams with frp reinforcement,” 2000.
- [45] Abdul-Wahab, H., Taylor, G., Price, W. & Pope, D., “Measurement and modelling of long-term creep in glued laminated timber beams used in structural building frames,” *The structural Engineer*, vol. 76, pp. 271–281, 1998.
- [46] Shekarchi, M., Oskouei, A.V. & Raftery, G.M., “Flexural behavior of timber beams strengthened with pultruded glass fiber reinforced polymer profiles,” *Composite Structures*, vol. 241, 2 2020.

# Appendices

## A. Design options

First, a logical cross-section design of the deck must be chosen. This is a difficult task regarding the endless options that are possible. Regarding the scope of this research, the final goal is a timber deck system with a restricted height of  $\pm 1000$  mm. Therefore, truss systems and arch solutions can already be dropped. Looking at existing concrete bridge designs, it can be seen that several structural forms are often used. Most simple form is a design with longitudinal beams that carry the load from the deck to the supports. More optimal solutions that are often used are box girder type decks. Which have several mechanical advantages over beam systems. Also concrete slab decks are used. They are less efficient in terms of material use, but increase the slenderness of the deck. These structural options are checked in terms of timber design.

Properties of timber decks can further be increased by applying high grade lamellae on the outsides of the deck, this can increase the moment resistance to a great extent. An other option of increasing the capacity of a timber deck is by reinforcing it. From concrete members we know that this reinforcement can also be prestressed to obtain even better member properties.

### A.1 Multi Criteria Analysis

Previous concepts are all analysed in terms of timber design using a Multi Criteria Analysis (MCA). Every criteria is given a certain weight factor up to 10 to include its relative importance. The criteria that are taken into account are explained below. The MCA and outcomes are presented in Figure A.1. It can be seen that the box type and slab type score high. With a sensitivity analysis is checked how weight factors and input influence the MCA outcome. This also results in a low score for the beam type, so this option is not considered further. The sensitivity analysis gives a small score increase of the box type. The final conclusion is that the slab type is the best option for a slender deck design. The box type is the best option for an optimal balance between the slenderness and the rest of the criteria. Therefore, both these types will be analysed further.

**Cross-section height** of the deck is the most important criteria (also see the problem statement in section 1.2) according to client demands. A big focus lies on the slender design of the bridge deck. Therefore this criteria is given weight factor 10.

**Transverse force distribution** will help to spread the loads over the total width of the deck.

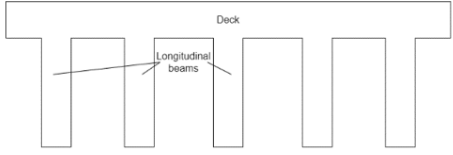
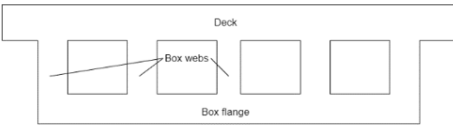
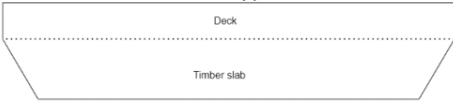
	Cross-section height	Transverse force distribution	Ease of fabrication	Material efficiency	Ease of prestress application	
<b>Weight</b>	<b>10</b>	<b>8</b>	<b>5</b>	<b>4</b>	<b>5</b>	TOTAL
<b>Beam type</b>						
	0	3	10	6	5	123
<b>Box type</b>						
	6	8	6	10	7	229
<b>Slab type</b>						
	10	10	0	2	8	228

Figure A.1: MCA of the three proposed bridge deck solutions

Low transverse force distribution induces high local loads. Therefore, only a small part of the total cross-section is used, requiring increased dimensions. So, good transverse force distribution is important for slender designs.

**Ease of fabrication** also considers the transportation possibilities and on site assembling of the structural parts. Fabrication difficulties can increase the total project costs. However, it is considered of less importance than previous criteria.

**Material efficiency** is obtained by allocating material further from the neutral axis, which will decrease the total required amount of material. However, this is at the expense of the slenderness. Which is in this case much more important than an efficient material use.

**Ease of prestress application** will ultimately decrease costs. Prestress cables can easily be located in slots where some small timber lamellae are left out. The difficult part is the connection between the ends of the cables and the deck. More deck material makes it easier to connect high prestress forces to the deck ends because changes of timber crushing is smaller.

## A.2 Cross-section analysis

First simple cross-section resistance calculations are made to be able to compare the slab deck and box deck for several strengthening options (see Figure A.2). For these options, only the moment resistance is considered because in general, this is the governing factor for horizontal slender members. This moment resistance is calculated per unity width. So the total slab bridge cross-section is composed of multiple times alternative (1). And the total box girder cross-section is composed of multiple I-profiles as in (2) to (7).

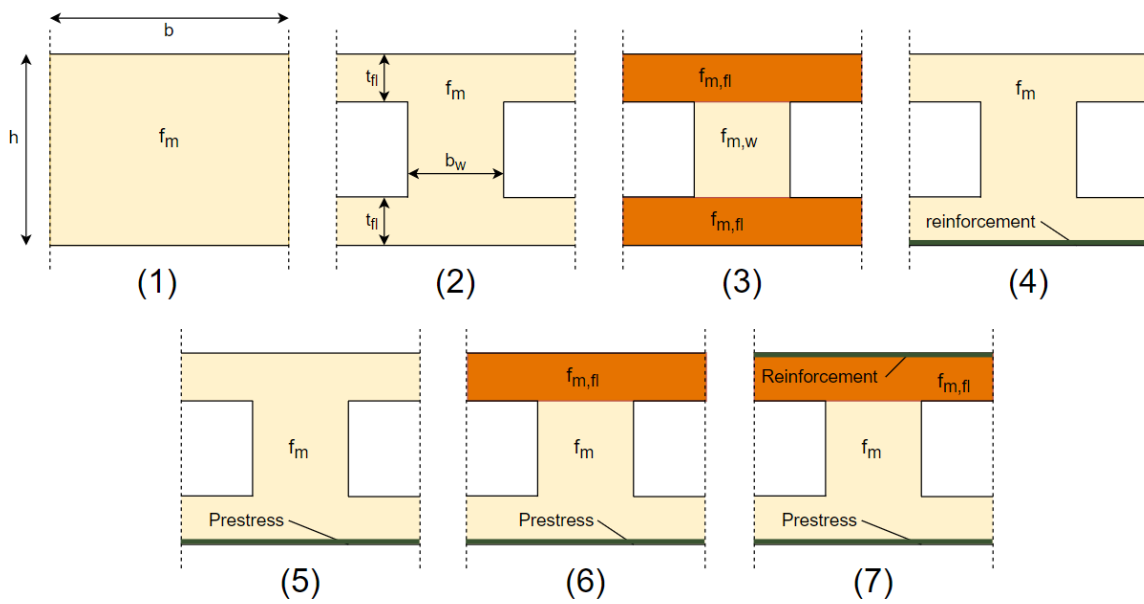


Figure A.2: Deck options

The governing equations to calculate the resistance for the different design options can be found in Appendix B.

### A.2.1 Calculations

A first estimation of the resistance of the previous deck options is done by inserting some first values as input parameters. The options (1), (2), (3) and (4) are compared to each other. Options (5), (6) and (7) are not yet calculated because these are combinations of the other options. Calculations of (5), (6) and (7) are done in later stage of this research.

Input parameters:

$$h = 800 \text{ [mm]}$$

$$b = 1000 \text{ [mm]}$$

$$h_w = 400 \text{ [mm]}$$

$$b_w = 400 \text{ [mm]}$$

$$t_{fl} = 200 \text{ [mm]}$$

$$t_{rnf} = 20 \text{ [mm]}$$

$$f_m = 25 \text{ [N/mm}^2\text{]}$$

$$f_{m,fl} = 40 \text{ [N/mm}^2\text{]}$$

$$f_{m,w} = 25 \text{ [N/mm}^2\text{]}$$

$$E_{gl} = 12000 \text{ [MPa]}$$

$$E_{fl} = 16000 \text{ [MPa]}$$

$$E_w = 12000 \text{ [MPa]}$$

$$E_{rnf} = 200000 \text{ [MPa]}$$



Following resistance moments are obtained for the different options:

	$M_{R,el}$	$M_{R,pl}$	
(1)	2667	-	[kNm]
(2)	2467	-	[kNm]
(3)	3893	-	[kNm]
(4)	3243	4174	[kNm]

Table A.1: Resistance moments for different cross-sections

### A.3 Design choice

From the comparison between option (1) and (2) follows that the full timber slab has a slightly higher capacity. However, the box section requires much less material and is therefore more efficient. Which is the basic idea of an I-beam. Then, two methods of further increasing the capacity of a box section are applied. These methods result in much higher resistant moments and could therefore reach higher slenderness. Conclusions about the ultimate moment resistance of option (3) and (4) can not really be drawn since the input values are still chosen from possible ranges. For these input values, option (4) has a slightly higher ultimate moment resistance than option (3). However, the biggest advantage of the reinforced section (4) is that it shows plastic behaviour. This happens because the high stiffness of the reinforcement allows for a great downward shift of the neutral axis of the cross-section. This causes the ductile compression failure to happen earlier than the brittle tensile failure. This leads to an overall ductile failure mode in bending. Meaning that after reaching the elastic limit, plastic deformations allow for further increased capacity. This way, elastic behaviour only has to go up to the serviceability limit state. After this point, the ultimate limit states can be reached by plastic behaviour. This makes the cross-section more efficient since a bigger part of the material reaches its capacity. The problem of option (3) is that it is likely to fail in a brittle manner. No plastic deformations will occur before the maximum capacity is reached. This means that only elastic material behaviour can be used, also in the ultimate limit states. This makes option (3) a less optimal solution than option (4). Another possibility of further increasing the capacity of (4) is by prestressing the reinforcement material (5). This prestressing exerts an initial moment that compensates the moment from loading, meaning that a higher action moment can be applied. Also an initial compression force is exerted on the cross-section by prestress, which will trigger the ductile compression failure in the top of the beam.

For previous stated reasons, a bridge deck option with prestressed reinforcement (5) is regarded as the most promising design for a slender timber deck. This option is further investigated in this research. In a prestressed timber cross-section, the compression failure may be present too dominantly. Therefore, also options (6) and (7) might be analysed for a stronger compression side of the beam.

# B. Governing equations

This Appendix gives the governing equations for the deck sections (1) to (4) in Figure B.1. For simplicity, deck sections (5) to (7) are not calculated.

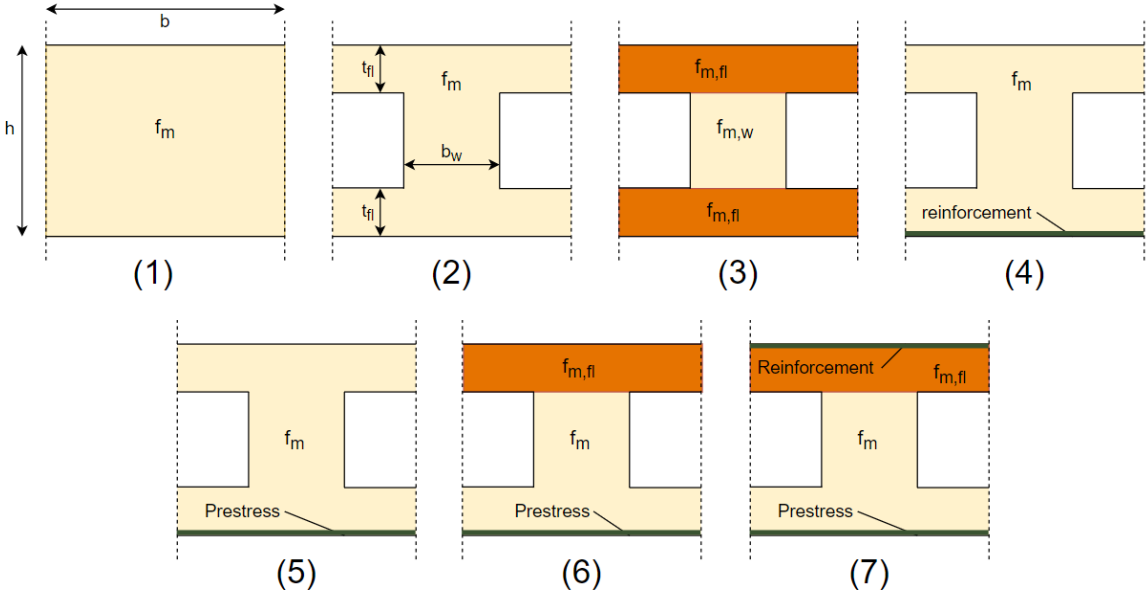


Figure B.1: Deck options

## B.1 Timber slab (1)

The timber slab resistance can be calculated with following simple formulas. A timber cross-section is very likely to have a brittle failure at the elastic limit. Therefore, only an elastic resistant moment can be taken into account.

$$I_{slab} = \frac{1}{12} \cdot b \cdot h^3$$

$$M_R = \frac{f_m \cdot I_{slab}}{h/2}$$

## B.2 Timber box section (2)

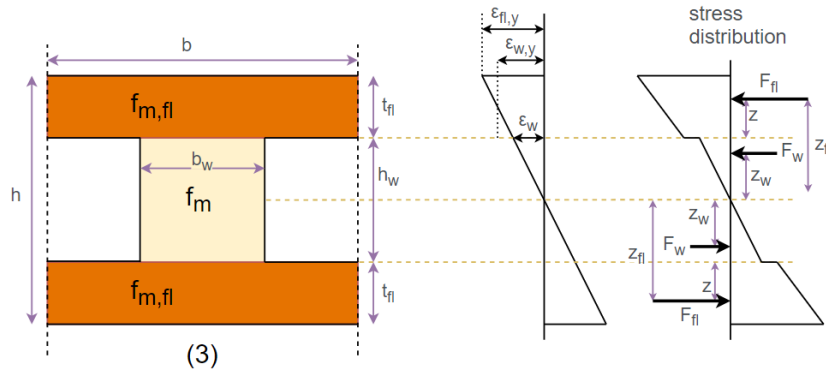
The moment resistance of a part of a multibox girder can be calculated with the same formulas as for the slab type (1).

$$I_{box} = \frac{1}{12} \cdot b \cdot h^3 - \frac{1}{12} \cdot (b - b_w) \cdot (h - 2t_f)^3$$

$$M_R = \frac{f_m \cdot I_{box}}{h/2}$$

## B.3 Hybrid timber box section (3)

The resistant moment of a hybrid timber section can be calculated based on the strain and stress diagram. Again, only an elastic moment resistance is taken into account.



Maximum elastic strains (after these limits, the timber yields):

$$\epsilon_{fl,y} = \frac{f_{m,fl}}{E_{fl}}$$

$$\epsilon_{w,y} = \frac{f_{m,w}}{E_w}$$

Strain at the web when top of the flange reaches maximum elastic strain:

$$\epsilon_w = \frac{\epsilon_{fl,y}}{h/2} \cdot \frac{h_w}{2}$$

Corresponding Forces:

$$F_{fl} = E_{fl} \cdot 0.5(\epsilon_{fl,y} + \epsilon_w) \cdot b \cdot t_{fl}$$

$$F_w = E_w \cdot 0.5\epsilon_w \cdot b_w \cdot \frac{h_w}{2}$$

Lever arms of the forces:

$$z_w = \frac{2}{3} \cdot \frac{h_w}{2}$$

$$z_{fl} = z + \frac{h_w}{2}$$

where  $z$  is the centroid of a rectangle with one skewed side:

$$z = \frac{\frac{1}{2}(\epsilon_{fl,y} - \epsilon_w) \cdot t_{fl} \cdot \frac{2}{3} t_{fl} + \epsilon_w \cdot t_{fl} \cdot \frac{1}{2} t_{fl}}{\frac{1}{2}(\epsilon_{fl,y} - \epsilon_w) \cdot t_{fl} + \epsilon_w \cdot t_{fl}}$$

Moment resistance:

$$M_R = 2 \cdot F_{fl} \cdot z_{fl} + 2 \cdot F_w \cdot z_w$$

## B.4 Reinforced timber box section (4)

### Elastic equations

For the reinforced section, an elastic and plastic resistance can be calculated. Putting reinforcement in the lower side of the box flange will trigger the ductile compression failure in bending. Therefore, an elastic- and a plastic resistant moment is calculated.

Calculating the elastic neutral axis:

$$A_{fl,t} = b \cdot t_{fl}$$

$$A_w = b_w \cdot h_w$$

$$A_{fl,b} = b \cdot (t_{fl} - t_{rnf})$$

$$A_{rnf} = b \cdot t_{rnf}$$

Distance from top of the section to centre of gravity of the specific part:

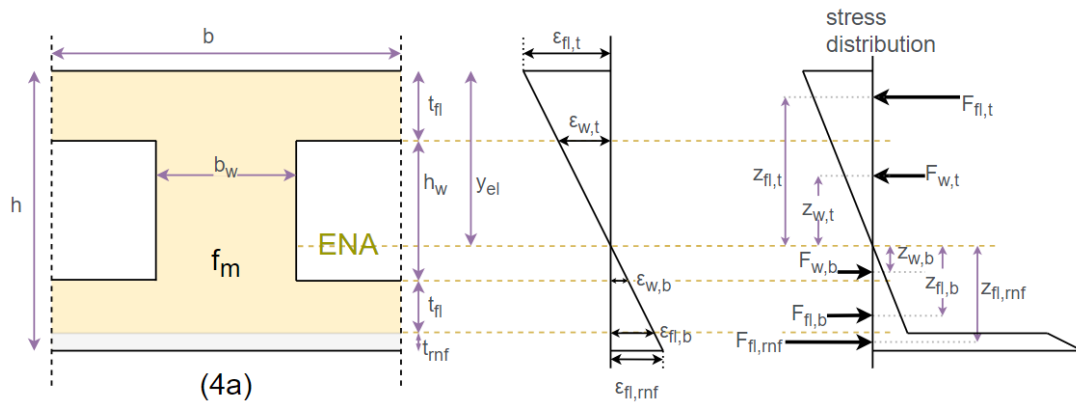
$$y_{fl,t} = \frac{t_{fl}}{2}$$

$$y_w = (t_{fl} + \frac{h_w}{2})$$

$$y_{fl,b} = t_{fl} + h_w + \frac{t_{fl} - t_{rnf}}{2}$$

$$y_{rnf} = h - \frac{t_{rnf}}{2}$$

$$y_{el} = \frac{E_{gl} \cdot A_{fl,t} \cdot y_{fl,t} + E_{gl} \cdot A_w \cdot y_w + E_{gl} \cdot A_{fl,b} \cdot y_{fl,b} + E_{rnf} \cdot A_{rnf} \cdot y_{rnf}}{E_{gl} \cdot (A_{fl,t} + A_w + A_{fl,b}) + E_{rnf} \cdot A_{rnf}}$$



Strain values (based on similar triangles):

$$\epsilon_{fl,t} = \frac{f_m}{E_{gl}}$$

$$\epsilon_{w,t} = \frac{\epsilon_{fl,t}}{y_{el}} \cdot (y_{el} - t_{fl})$$

$$\epsilon_{w,b} = \frac{\epsilon_{fl,t}}{y_{el}} \cdot (t_{fl} + h_w - y_{el})$$

$$\epsilon_{fl,b} = \frac{\epsilon_{fl,t}}{y_{el}} \cdot (h - y_{el} - t_{rnf})$$

$$\epsilon_{fl,rnf} = \frac{\epsilon_{fl,t}}{y_{el}} \cdot (h - y_{el})$$

Corresponding forces:

$$F_{fl,t} = E_{gl} \cdot \frac{1}{2} (\epsilon_{fl,t} + \epsilon_{w,t}) \cdot t_{fl} \cdot b$$

$$F_{w,t} = E_{gl} \cdot \frac{1}{2} \epsilon_{w,t} \cdot (y_{el} - t_{fl}) \cdot b_w$$

$$F_{w,b} = E_{gl} \cdot \frac{1}{2} \epsilon_{w,b} \cdot (t_{fl} + h_w - y_{el}) \cdot b_w$$

$$F_{fl,b} = E_{gl} \cdot \frac{1}{2} (\epsilon_{w,b} + \epsilon_{fl,b}) \cdot (t_{fl} - t_{rnf}) \cdot b$$

$$F_{fl,rnf} = E_{rnf} \cdot \frac{1}{2} (\epsilon_{fl,b} + \epsilon_{fl,rnf}) \cdot t_{rnf} \cdot b$$

Leverarms of the forces:

$$z_{fl,t} = \frac{\frac{1}{2} (\epsilon_{fl,t} - \epsilon_{w,t}) \cdot t_{fl} \cdot \frac{2}{3} t_{fl} + \epsilon_{w,t} \cdot t_{fl} \cdot \frac{1}{2} t_{fl}}{\frac{1}{2} (\epsilon_{fl,t} - \epsilon_{w,t}) \cdot t_{fl} + \epsilon_{w,t} \cdot t_{fl}} + (y_{el} - t_{fl})$$

$$z_{w,t} = \frac{2}{3} (y_{el} - t_{fl})$$

$$z_{w,b} = \frac{2}{3} (t_{fl} + h_w - y_{el})$$

$$z_{fl,b} = \frac{\frac{1}{2} (\epsilon_{fl,b} - \epsilon_{w,b}) (t_{fl} - t_{rnf}) \cdot \frac{2}{3} (t_{fl} - t_{rnf}) + \epsilon_{w,b} (t_{fl} - t_{rnf}) \cdot \frac{1}{2} (t_{fl} - t_{rnf})}{\frac{1}{2} (\epsilon_{fl,b} - \epsilon_{w,b}) \cdot (t_{fl} - t_{rnf}) + \epsilon_{w,b} \cdot (t_{fl} - t_{rnf})} + (t_{fl} + h_w - y_{el})$$

$$z_{fl,rnf} = \frac{\frac{1}{2} (\epsilon_{fl,rnf} - \epsilon_{fl,b}) t_{rnf} \cdot \frac{2}{3} t_{rnf} + \epsilon_{fl,b} \cdot t_{rnf} \cdot \frac{1}{2} t_{rnf}}{\frac{1}{2} (\epsilon_{fl,rnf} - \epsilon_{fl,b}) \cdot t_{rnf} + \epsilon_{fl,b} \cdot t_{rnf}} + (h - y_{el} - t_{rnf})$$

Elastic moment resistance:

$$M_{R,el} = z_{fl,t} \cdot F_{fl,t} + z_{w,t} \cdot F_{w,t} + z_{w,b} \cdot F_{w,b} + z_{fl,b} \cdot F_{fl,b} + z_{fl,rnf} \cdot F_{fl,rnf}$$

## Plastic equations

For the plastic moment resistance, the assumption is made that the timber in compression has failed over the height of the top flange.

Maximum elastic strain is reached at the top of the web:

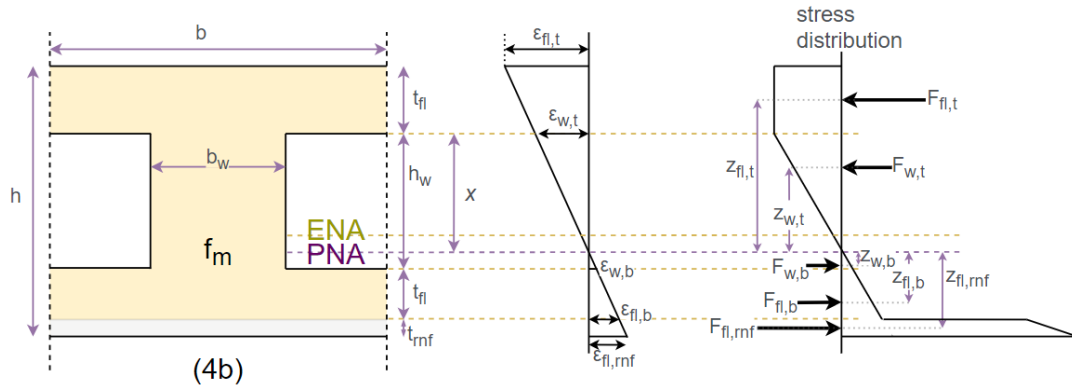
$$\epsilon_{w,t} = \frac{f_m}{E_{gl}}$$

Plastification is taken into account by non-linear behaviour. Because of plastic deformations, the neutral axis of the cross-section shifts downwards. This is taken into account by the variable  $x$  in followings equations.

Strains based on  $\epsilon_{w,t}$ :

$$\epsilon_{fl,t} = \frac{\epsilon_{w,t}}{x} \cdot (x + t_{fl})$$

$$\epsilon_{w,b} = \frac{\epsilon_{w,t}}{x} \cdot (h_w - x)$$



$$\epsilon_{fl,b} = \frac{\epsilon_{w,t}}{x} \cdot (h_w - x + t_{fl} - t_{rnf})$$

$$\epsilon_{fl,rnf} = \frac{\epsilon_{w,t}}{x} \cdot (h_w - x + t_{fl})$$

Corresponding forces:

$$F_{fl,t} = f_m \cdot t_{fl} \cdot b$$

$$F_{w,t} = E_{gl} \cdot \frac{1}{2} \epsilon_{ps_{w,t}} \cdot x \cdot b_w$$

$$F_{w,b} = E_{gl} \cdot \frac{1}{2} \epsilon_{ps_{w,b}} \cdot (h_w - x) \cdot b_w$$

$$F_{fl,b} = E_{gl} \cdot \frac{1}{2} (\epsilon_{w,b} + \epsilon_{fl,b}) \cdot (t_{fl} - t_{rnf}) \cdot b$$

$$F_{fl,rnf} = E_{rnf} \cdot \frac{1}{2} (\epsilon_{fl,b} + \epsilon_{fl,rnf}) \cdot t_{rnf} \cdot b$$

The total sum of forces should be set equal to zero to obtain equilibrium:

$$F_{fl,t} + F_{w,t} + F_{w,b} - F_{fl,b} - F_{fl,rnf} = 0$$

$x$  is the only unknown in this equation. Sum of forces can be solved for  $x$ .

Leverarms of the forces:

$$z_{fl,t} = x + \frac{1}{2} t_{fl}$$

$$z_{w,t} = \frac{2}{3} x$$

$$z_{w,b} = \frac{2}{3} (h_w - x)$$

$$z_{fl,b} = \frac{\frac{1}{2} (\epsilon_{fl,b} - \epsilon_{w,b}) (t_{fl} - t_{rnf}) \cdot \frac{2}{3} (t_{fl} - t_{rnf}) + \epsilon_{w,b} (t_{fl} - t_{rnf}) \cdot \frac{1}{2} (t_{fl} - t_{rnf})}{\frac{1}{2} (\epsilon_{fl,b} - \epsilon_{w,b}) (t_{fl} - t_{rnf}) + \epsilon_{w,b} (t_{fl} - t_{rnf})} + (h_w - x)$$

$$z_{fl,rnf} = \frac{\frac{1}{2} (\epsilon_{fl,rnf} - \epsilon_{fl,b}) t_{rnf} \cdot \frac{2}{3} t_{rnf} + \epsilon_{fl,b} t_{rnf} \cdot \frac{1}{2} t_{rnf}}{\frac{1}{2} (\epsilon_{fl,rnf} - \epsilon_{fl,b}) t_{rnf} + \epsilon_{fl,b} t_{rnf}} + (h_w - x + t_{fl} - t_{rnf})$$

Plastic moment resistance:

$$M_{R,pl} = z_{fl,t} \cdot F_{fl,t} + z_{w,t} \cdot F_{w,t} + z_{w,b} \cdot F_{w,b} + z_{fl,b} \cdot F_{fl,b} + z_{fl,rnf} \cdot F_{fl,rnf}$$

# C. Standard viaducts

Figures below display continuous two span concrete viaducts that are common in the Netherlands. Spans are displayed in meters.



## D. Timoshenko ODE system

This Appendix shows that the shear deformations of the bridge deck can be neglected. The Euler-Bernoulli deflection is calculated according to the ODE relations in Section 7.1.2. The Timoshenko deflection is calculated using the relations below which also incorporate the shear stiffness of the bridge deck.

### D.1 Timoshenko equations

Coupled Differential Equations for the Timoshenko system:

$$EI \frac{d^2 \phi}{dx^2} - GA_{eff} \left( \frac{dw}{dx} + \phi \right) = 0 \quad (D.1a)$$

$$GA_{eff} \left( \frac{d^2 w}{dx^2} + \frac{d\phi}{dx} \right) = -q \quad (D.1b)$$

Kinematic relations:

$$\gamma = \frac{dw}{dx} + \phi \quad (D.2a)$$

$$\kappa = \frac{d\phi}{dx} \quad (D.2b)$$

Constitutive relations:

$$V = GA_{eff} \gamma \quad (D.3a)$$

$$M = EI \kappa \quad (D.3b)$$

Equilibrium equations:

$$q = -\frac{dV}{dx} \quad (D.4a)$$



$$V = \frac{dM}{dx} \quad (D.4b)$$

## D.2 Results

Both the Bernoulli-Euler and Timoshenko systems are solved for the boundary conditions based on a simply supported beam with a span of 30000 mm and a cross-section of 1000 x 1000 mm. Values for the stiffnesses of timber are assumed at  $E = 13500N/mm^2$  and  $G = 850N/mm^2$  and the load is  $q = 20kN/m$ . The results are plotted in Figure D.1. The Timoshenko deflection is only 2 mm higher than the Euler-Bernoulli deflection, which comes down to approximately 1%.

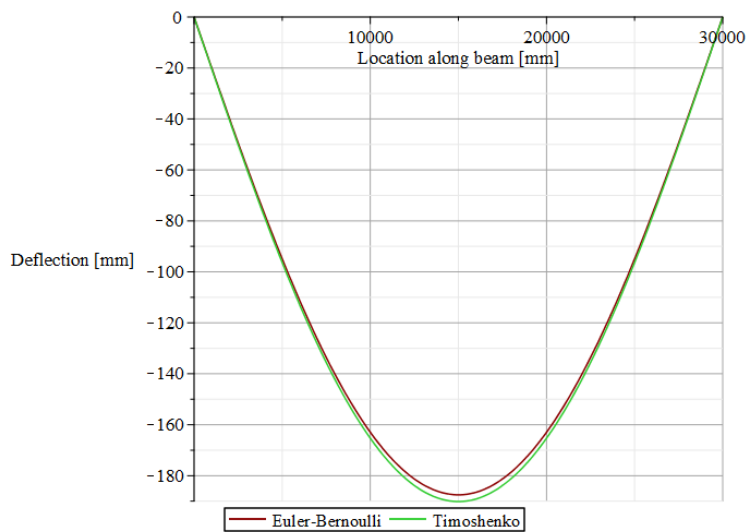


Figure D.1: Euler-Bernoulli and Timoshenko deflection